國立臺灣大學理學院地質科學系

碩士論文

Department of Geosciences

College of Science

National Taiwan University

Master Thesis

2018 年花蓮地震中嶺頂斷層北段之淺部破裂

Shallow rupture of the northernmost Lingding Fault during the 2018 Hualien earthquake

陳建銘

Jian-Ming Chen

指導教授: 王昱 博士

Advisor: Yu Wang, Ph.D.

中華民國 111 年 06 月

June, 2022

doi:10.6342/NTU202202354

國立臺灣大學碩士學位論文
口試委員會審定書
MASTER'S THESIS ACCEPTANCE CERTIFICATE
NATIONAL TAIWAN UNIVERSITY

2018 年花蓮地震中嶺頂斷層北段之淺部破裂

Shallow rupture of the northernmost Lingding Fault during the 2018 Hualien earthquake

本論文係陳建銘君(R09224201)在國立臺灣大學地質科學系暨研究所完成之碩士學位論文，於民國 111 年 6 月 28 日承下列考試委員審查通過及口試及格，特此證明。

The undersigned, appointed by the Department of Geosciences on 28th June 2022, have examined a Master's thesis entitled above presented by Jian-Ming, Chen (R09224201) candidate and hereby certify that it is worthy of acceptance.

口試委員 Oral examination committee:

王昱 (指導教授 Advisor)

盧志恒

郭昱廷

張中白

doi:10.6342/NTU202202354

誌謝

歷經了三年，這份研究終於告了一段落，從一開始什麼都不會，到慢慢地學會如何使用各種軟體做正射影像、次像素匹配等等，這一路說長不長，說短不短，碩士的生涯就在與這些軟體的奮鬥中度過。能夠完成這份論文，歸功於許多人在這些年的幫助，感謝王昱老師當時肯收留我，一路上的教導和討論，才能有這份論文的誕生；感謝郭昱廷老師帶著我買航照影像、耐心地幫助我解決軟體上遇到的困難，讓研究的路途減輕了一些負擔；感謝另外兩位口試委員:張中白老師和盧志恆博士，給予論文更完善的討論和指正，使本論文能夠完整的呈現；感謝吳逸民老師提供地震資料，使本研究的討論可以更為豐富；感謝林耕霈學長在斷層滑移反演的問題上提供協助。

在碩士生涯中，感謝研究室的大家，仙草、EU、昇翰、卉珊、Saw Myat Min、Ei Mhone、恩維學姊，在全變的日子，一起經歷了許多被電的咪聽，偶爾出的野外，有了你們，讓碩士的生活增添了許多趣味。感謝研究室助理阿賢幫忙處理行政事務，尤其是口試那一段忙亂的日子。感謝一起念到碩班的 B05 夥伴，雖然全變地處偏遠，平常很少遇到大家，但遇到了常有聊不完的話題。感謝參與大咪的 Bruce 老師、葉恩肇老師和莊昀叡老師及其研究室的同學，雖然每次報告完的建議和問題都讓頭很痛，但也使得本研究的結果和討論有更好的面貌。

待在台大的六年，歲月飛逝，許多的野外和趣事都還歷歷在目，感謝從大一到現在教過我的老師們，尤其是地質系和海研所的老師，使我對於地球科學仍保有好奇和熱忱，從科學研究的經驗談，口頭和書面報告的磨練，以及科學議題的討論，都豐富了這些年的研究路途。感謝這些年家人的支持，讓我可以任性的追求自己所想要的。最後，感謝自己熬過了這一切，雖然一直期待著畢業，但到了碩班的尾聲，還是有一點的感傷，我想那些在全變的日子，那些忙碌工作的夜晚，會成為碩士回憶中不可抹去的一塊。

doi:10.6342/NTU202202354

摘要

2018 年 2 月 6 日時，一場規模 6.4 的地震發生在花蓮外海，並伴隨兩條陸上活動斷層(米崙斷層和嶺頂斷層)的同震地表變形與破裂。在地震後對於此一地震事件的地表變形相關調查和研究主要集中在米崙斷層上，而嶺頂斷層則較少被提及和討論，歸咎其部分原因可能與嶺頂斷層主要位在較偏僻的花蓮溪中，致使相關的調查和研究不易有關。為了瞭解嶺頂斷層在本次地震事件中的破裂行為與分佈，本研究使用震前、震後的航空照片與光學衛星影像探討該斷層在本次地震中的同震地表破裂行為。本研究除了透過影像判識來描繪花蓮溪床上相關的地表破裂外，次像素匹配的方法也用來計算地表位移量和空間上的變化。這兩種方法都揭示斷層破裂主要位在花蓮溪中，並在本次地震中呈現左移的走向滑移運動型態。透過次像素匹配所測得的近斷層地表位移以南北向的位移分量為主，從北邊的花蓮溪口附近(>1.0 公尺)往南邊的木瓜溪(<0.4 公尺)遞減，其量值與 GNSS RTK 以及花蓮大橋上量測的位移量相近。本研究將所得到的地表變形進行一系列的半空間斷層滑移模型測試，結果顯示嶺頂斷層可能為一條高角度的斷層，且在本次的花蓮地震中，破裂集中在較淺部的位置(<5 公里深)。從本區域過去三十年的地震分布推論，本研究認為此地區存在兩條主要的斷層系統，斷層面分別向西和東傾，而結合 2018 花蓮地震的主震和餘震位置，我們認為這次的地震主要和向西傾的斷層活動有關，並導致位在較淺部的嶺頂斷層錯動。綜上所述，在 2018 花蓮地震中，嶺頂斷層北端有發生淺部的破裂，地表的變形以左移的走向滑移為主，並在花蓮溪中上形成一些地表破裂。

關鍵字: 航空照片、嶺頂斷層、地表變形、次像素匹配、2018 年花蓮地震

doi:10.6342/NTU202202354

Abstract

On 6th February 2018, the Mw 6.4 Hualien earthquake occurred near Hualien City, accompanied with ground deformations along the Milun and the Lingding Faults. While the post-event field survey provided a detailed description and data of deformation along the Milun Fault, there were not many reports about the ground deformations along the Lingding Fault since the main trace of the Lingding Fault passed through the Hualien River bed. In order to investigate the rupture behavior of the Lingding Fault during the 2018 earthquake, the pre- and post-earthquake aerial photos are used in this study. We not only map the plausible coseismic surface rupture on the Hualien River bed by visual inspection of the images, but also obtain the surface displacements to determine the spatial pattern and magnitude of offset across the Lingding Fault by Co-Registration of Optically Sensed Images and Correlation (COSI-Corr). Both approaches reveal clear deformations along the Hualien River bed, suggesting the 2018 coseismic rupture along the Lingding Fault is dominated by the left-lateral slip, where the displacement decreased from north to south, from >1.0m near the Hualien River mouth to <0.4 m south of the Mugua River. Such a pattern agrees well with the GNSS RTK field survey result. After that, we conduct a series of half-space fault slip models to fit the sub-pixel correlation result and GNSS RTK survey data. The result indicates the slip on the Lingding Fault concentrated in the shallow depth (<5 km depth) and the

doi:10.6342/NTU202202354

fault plane dips at a high angle. The largest fault slip happened at the northernmost tip of the Lingding Fault. The thirty-year seismicity reveals two major fault system in this area, with their fault planes dipping to the east and west, respectively. From the distribution of the mainshock and aftershocks of the 2018 Hualien earthquake, we suggest the motion of the west-dipping fault caused this event, and triggered the movement of the Lingding Fault. To sum up, the shallow portion of the northernmost Lingding Fault did rupture during the 2018 Hualien earthquake, forming a series of left-lateral surface ruptures with limited fault-normal movement.

Keywords: aerial photos, surface deformation, the Lingding Fault, sub-pixel correlation, 2018 Hualien earthquake

doi:10.6342/NTU202202354

Table of Contents

口試委員審定書 I
誌謝 II
摘要 III
Abstract IV
Table of Contents VI
Figure Contents VIII
Table Contents XII
1. Introduction 1
2. Geological Background 6
3. Review of Previous Studies 12
3.1 The geophysical studies about the Lingding Fault geometry 12
3.2 The 2018 Hualien earthquake-related studies 19
4. Materials and Methods 31
4.1 Materials 33
4.2 The orthorectification of aerial photos 36
4.3 The mapping of earthquake-related structures 42
4.4 Sub-pixel correlation 42
4.5 Numerical processing 45
4.6 Elastic half-space dislocation model 47
5. Results 49
5.1 The orthorectification of aerial photos 49
5.2 The mapping of earthquake-related structures 51
5.3 Sub-pixel correlation 57
5.4 Elastic half-space dislocation model 61
6. Discussion 67
6.1 Internal validation of the ground displacement results 67
6.1.1 The different methods for aerial photo orthorectification 67

doi:10.6342/NTU202202354

6.1.2 Comparison of the result from aerial photos with the result from satellite images 72
6.2 External validation for the displacement result 76
6.2.1 Comparison with the field survey 76
6.2.2 Comparison with GNSS data 77
6.3 The shallow fault slip 81
6.3.1 The effect of the sub-pixel correlation result 81
6.3.2 Comparison of the fault slip with published studies 84
6.3.3 The behavior of the Lingding Fault in the 2018 Hualien earthquake 86
6.4The regional geological model of the Lingding Fault 89
6.5The relation between the Lingding Fault and the Milun Fault 97
7. Conclusion 100
References 102
Supplementary 112

doi:10.6342/NTU202202354

Figure Contents

Figure 1.1 (a) Global earthquakes (1900-2013) and major volcanos around the Ring of Fire (modified from U.S. Geological Survey (USGS)). (b) The seismicity in and around Taiwan (1990-2019). 2

Figure 2.1 (a) The tectonic setting of Taiwan. (b) Active faults and the 2018 Hualien Earthquake sequence near Hualien City. The star symbol marks epicenter of the mainshock. 8

Figure 3.1 (a) The electric resistivity survey in Yueimei area (from 簡立凱，2015). Two discontinuities can be found in this survey line, which could be Lingding Fault and Yuemei Fault. (b) The seismic reflection survey along the Mugua River (from 謝一銘，2017). The color line in the lower figure is the strong reflection line, and the blue line could be the basement in this area. 13

Figure 3.2 (a) The GPS result across the fault (from 陳等人，2008). The upper profile is the fault-perpendicular component of the velocity, and the lower profile is the fault-parallel component of the velocity. The velocity changes across the fault in the parallel component, but there is no obvious change in perpendicular component. (b) The result of PS-InSAR in northern Longitudinal Valley (from 廖昱茨，2014). In the northernmost of the Lingding Fault, the velocity is different for both sides. But the velocity is similar in southern part. 15

Figure 3.3 The seismicity, seismic velocity and tomography of the northern part Lingding Fault (modified from 陳等人，2018). A high angle east-dipping fault can be revealed. 17

Figure 3.4 (a) The seismicity and focal mechanisms of the northern part Lingding Fault (from Kuochen et al., 2004). An east-dipping fault is also appeared, but the slope is gentler and locates more west. (b) The seismicity result of the northern Lingding Fault (from 鍾珮瑜，2019). A group of seismicity locates in the depth of 10 to 15 km. The distribution is nearly an east-dipping fault. 18

Figure 3.5 The related previous researches used seismic method to study this area. (a) The distribution and focal mechanism of aftershocks in 2018 Hualien Earthquake (Modified from Kuo-Chen et al., 2018). (b) The fault slips and asperities in this event (from Lee et al., 2018). (c) The levelling result after the 2018 Hualien Earthquake (modified from CGS, 2018). (d) The tomography and σ-anomaly in east Taiwan (from Toyokuni et al., 2021). 22

Figure 3.6 The InSAR results from previous studies. (a) The coseismic interferograms results (from Yen et al., 2018). The red line in profiles below is LOS deformation and gray line represents the topography. (b) The surface deformation derived from InSAR (from Tung et al., 2019). The purple dots in the profiles are

doi:10.6342/NTU202202354

deformation signals from ALOS-2, and the blue ones are from Sentinel-1..... 25
Figure 3.7 The coseismic surface deformation results. (a) The 3D surface deformation (from Yen et al., 2018). The arrow represents the horizontal displacement and the color means the vertical component. (b) The result of RTK and GPS stations (from Wu et al., 2019)..... 26
Figure 3.8 The fault slip results inversed mostly from InSAR and GPS. (a) is from Yang et al., 2018. (b) is from Zhao et al., 2020. (c) is from Huang & Huang, 2018. (d) is from Lo et al., 2019. The red rectangles are the potential fault settings related to the Lingding Fault..... 28
Figure 3.9 The different geological structures models in this area. (a) is from Lee et al., 2018. (b) is from Lo et al., 2019. (c) is from Yen et al., 2018. (d) is from Shyu et al. 2016b..... 30
Figure 4.1 The general work flow in this study. For more detailed information, please see the corresponding chapters. 32
Figure 4.2 The aerial photos used in this study. (a) Pre-event aerial photos. (b) Post-event aerial photos. 35
Figure 4.3 The location of GCPs, CPs, and ChPs in pre-event image (a) and post-event image (b). 38
Figure 4.4 The workflow of the orthorectification of the aerial photos for pre- and post-event aerial photos. 40
Figure 4.5 The workflow for examining the influence of the coseismic deformation during the orthorectification. We only selected one side of GCPs of post-event images to do the calculation..... 41
Figure 4.6 The work flow of the sub-pixel correlation, including pre-processing and post-processing in this research. 44
Figure 4.7 The location of the Lingding Fault and 13 profiles. (a) is for aerial photos, and (b) is for SPOT 7 images..... 45
Figure 4.8 The condition to remove the outliers with moving average method, used profile 11 right part of NS component profile as example. The blue line is the moving average. The yellow and green lines are the upper boundary and lower boundary, respectively. The black line is the original data, and the red line is the data after filtering..... 46
Figure 4.9 The offset across the fault (the red arrow). The green line is the linear regression line on each side. The black dots are the original data, and the red dots are the data after filtering the outliers. The purple dash line is the location of the fault. 47
Figure 5.1 The comparison of the DSMs. (a) Comparison of pre- and post-DSM. (b) Comparison of pre-DSM and 20 m DEM. (c) Comparison of post-DSM and 20

doi:10.6342/NTU202202354

m DEM..... 50
Figure 5.2 The result of orthorectification of the aerial photos. (a) is the pre-event image, and (b) is the post-event image. The red rectangle is the area used in the calculation of sub-pixel offset..... 51
Figure 5.3 The earthquake-related structures we mapped, with the closer images of ruptures and suspected ruptures..... 54
Figure 5.4 The overall mapping result of earthquake-related structures, and the field survey results by CGS and the previous study are also included..... 56
Figure 5.5 The offset maps of three window sizes. The upper column is the E/W component, and the lower column is the N/S component..... 58
Figure 5.6 The displacement across the fault of 13 profiles. The left is the W/E component of the displacement, and the right is the N/S component..... 59
Figure 5.7 The displacement across the fault of 13 profiles. The left is the parallel to the fault component of the displacement (+: left-lateral motion, -: right-lateral motion), and the right is the perpendicular to the fault component (+: extensional motion, -: compressional motion)..... 60
Figure 5.8 The down-sampling process for the surface deformation data. We use average window size of 60, and step of 60..... 61
Figure 5.9 The checkboard tests with three different sizes. The test data include the surface deformation from COSI-Corr, RTK GNSS, and GPS. The upper column is the input checkboard setting, and the lower column is the output result..... 62
Figure 5.10 (a) The input model setting with different fault lengths (the arrows are the data points of surface deformation and the green line is fault location) and output fault slip results. (b) The average residual (E/W component, N/S component, and combination of two directions) for different fault lengths..... 64
Figure 5.11 The average residual for different fault dips (degree). The positive degree means the fault plane dips to the east, and the minus one means west-dipping plane..... 64
Figure 5.12 The input model setting (arrows: input surface deformation data, green line: fault location) and the inversion result of fault slips..... 65
Figure 5.13 The surface deformations for input data (upper column) and fault slip model (middle column). The bottom column is the average residual..... 66
Figure 6.1 The result of different orthorectification methods with three window sizes (32x32, 64x64, and 128x128). The orange line is the original method we used for orthorectification. The blue and green lines are the control points only turned on in the western and eastern part, respectively..... 71
Figure 6.2 The result of COSI-Corr using different materials with three window sizes (32x32, 64x64, and 128x128). The red line is the result of aerial photos, and the

doi:10.6342/NTU202202354

blue line is the result of SPOT 7 images. 75
Figure 6.3 Left is the parallel component of displacement across the fault. Profile 7, the red rectangle, covers the Hualien Bridge. Right is the photo of the deformed Hualien Bridge (modified from CGS, 2018). The displacement for three window sizes is similar to the field measurement, ~70 cm. 77
Figure 6.4 (a) The comparison of GNSS and the result of COSI-Corr (window size 64x64), and the lower column is the distribution of the deviation between the result of COSI-Corr and GNSS. (b) The spatial distribution of the deviation between the result of COSI-Corr and GNSS, with E/W component and N/S component. 79
Figure 6.5 The vertical component of offsets comparison between the model result and GPS and leveling observations (CGS, 2018). 81
Figure 6.6 The inversion fault slip results. (a) The input data includes sub-pixel correlation result and GNSS. (b) The input data only used GNSS. Left is the model setting, and right is the fault slip results with and without vectors. 83
Figure 6.7 The fault slip results from different previous studies. (a) from Lo et al. (2019) (b) from Lee et al. (2018) (c) from Zhao et al. (2020). 85
Figure 6.8 The combination of fault-related structures mapping, the displacement along the fault and the fault slip result. 88
Figure 6.9 The relocated seismicity in research area (provided by Professor Yih-Min Wu). Two fault planes can be found, with west-dipping (red dash line) and east-dipping plane (pink dash line). The upper raw and the lower raw has slight looking angle difference. 91
Figure 6.10 (a) The location of the tomography profile. (b) The Vp, Vs, and Vp/Vs velocity model (produced by the Taiwan Velocity Model (http://tecdc.earth.sinica.edu.tw/TWtomo/VerticalProfile.php) 92
Figure 6.11 The combination of the thirty years seismicity (blue dots), the mainshock (star symbol) and the aftershocks (green dots) of the 2018 Hualien earthquake, and the fault slip and geometry of the Lingding Fault in three dimension. We display their relation in four different angles, and the direction shows in the uppermost raw. 94
Figure 6.12 The regional geological structure model of the Lingding Fault. The star is the 2018 Hualien earthquake mainshock. 96
Figure 6.13 The displacement and the fault geometry from the 2018 Hualien earthquake around the Milun Fault and the Lingding Fault area. The information is from Kuo et al. (2018), Lee et al. (2018), Lo et al. (2019), Tung et al. (2019), Yen et al. (2018). 99

doi:10.6342/NTU202202354

Table Contents

Table 4.1 Summary of the materials used in this study. 34
Table 4.2 The parameter of DMC photo used in this study. 37
Table 6.1 The fault geometry model for inversion of previous studies. 84

doi:10.6342/NTU202202354

1. Introduction

Taiwan is located in the Ring of Fire around the Pacific Ocean, where the seismic and volcanic hazards have received great attention due to their high impacts on the society in these areas (Figure 1.1a). This is particularly true in Taiwan, especially after the catastrophic 1999 Mw 7.6 Chi-Chi earthquake struck the central Taiwan. After the infamous Chi-Chi earthquake in 1999, several significant earthquake events also occurred around the island of Taiwan and caused considerable damage to the nearby cities in the past decade. These events include the 2016 Mw 6.6 Meinong earthquake in southern Taiwan (Huang et al., 2016) and the 2018 Mw 6.4 Hualien earthquake in eastern Taiwan (Lee et al., 2018) (Figure 1.1b). Many seismological, geodetic and geological studies were conducted after these events to understand the mechanism, the active tectonics, the seismogenic sources, and the surface deformation associated with these earthquake events. All of these aim to mitigate seismic hazards in the future.

doi:10.6342/NTU202202354

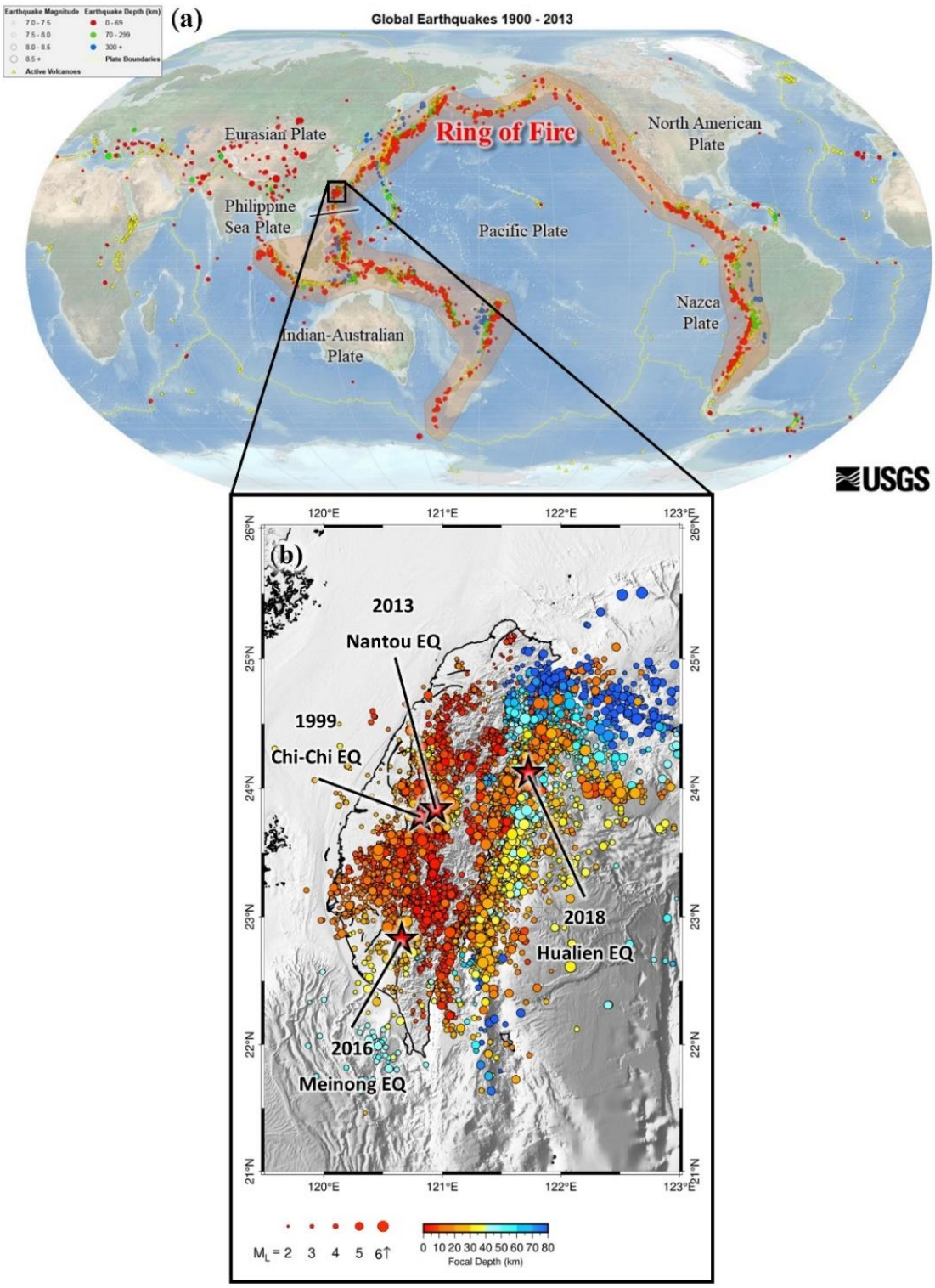

Figure 1.1 (a) Global earthquakes (1900-2013) and major volcanos around the Ring of Fire (modified from U.S. Geological Survey (USGS)). (b) The seismicity in and around Taiwan (1990-2019).

doi:10.6342/NTU202202354

The recent Hualien earthquake in 2018 is one of the vivid examples, which has been intensely studied after this damaging earthquake. The post-earthquake studies suggest this Mw 6.4 earthquake is caused by the movement of an offshore structure that propagates southward, and induced the fault surface ruptures of two on-land active faults (i.e., the Milun and the Lingding Fault) (Lee et al., 2018). Seventeen people died, and more than two hundred people were injured during the 2018 mainshock (Jian et al., 2018; Lee et al., 2018; Yen et al., 2018). The infrastructure was also severely damaged in the city of Hualien, with four buildings collapsing close to the surface rupture of the Milun Fault (Jian et al., 2018; Kuo-Chen et al., 2018; Lee et al., 2018). After the Hualien earthquake, the coseismic fault surface rupture of the Milun fault received great attention, partly because it locates in the populated Hualien City, and lots of damages occurred along its fault trace. In contrast, the discussion about the coseismic deformation along the Lingding Fault received much less attention in the post-earthquake field survey. The reasons for less surface-rupture documentation along the Lingding Fault could result from its rural location with relatively less damage, and most of its active fault traces are located in the Hualien River, making the surface-rupture field survey and documentation much more difficult after the earthquake. Note that while prior studies suggest the Lingding Fault is a left-lateral strike-slip fault with the reverse component (Barrier & Angelier, 1986; CGS, 2018; Shyu et al., 2016a), the post-

doi:10.6342/NTU202202354

earthquake leveling and geodetic measurements across the Lingding Fault suggest the fault motion during the 2018 earthquake is dominated by left-lateral slip with normal component, which contradicted the previous understandings of the Lingding Fault (more discussion can be found in chapters 2 and 3) (CGS, 2018; Wu et al., 2019). Since no coseismic surface rupture had been reported along the Lingding Fault prior to the 2018 earthquake, including the 1951 Hualien-Taitung earthquake sequence (Chen et al., 2008; Shyu et al., 2007; Yen et al., 2018), the rupture of the Lingding Fault during the 2018 earthquake thus gives us a unique opportunity to understand its active behavior, including the detailed surface displacement, shallow-depth fault-slip pattern, and regional active geological structures.

Although the surface rupture along the Lingding Fault is difficult to be documented in detail by the post-quake field survey, the sub-pixel correlation of aerial and satellite images provides an alternative way to study the near-fault deformation during the 2018 Hualien earthquake. In the past two decades, the sub-pixel correlation has become a powerful method for analyzing coseismic deformation (Avouac et al., 2006; Avouac et al., 2014; Binet & Bollinger, 2005; De Michele et al., 2010; Dominguez et al., 2003; Michel et al., 1999). The Co-registration of Optically Sensed Images and Correlation (COSI-Corr) is one of the sub-pixel correlation software packages that calculates the horizontal surface deformation from optical satellite

doi:10.6342/NTU202202354

imagery and aerial photos (Leprince et al., 2007). In general, this software package can resolve the displacements down to 1/10 of the input pixel size if the pre- and post-event images are well orthorectified with good image quality (Zinke et al., 2014). The results of horizontal surface deformation calculated by this method could not only show the near-field, but also far-field displacement, which is crucial for modeling fault slips at depth (Xu et al., 2016). Knowing the fault slip pattern at depth can help us realize the fault movement behavior and better constrain the earthquake rupture model.

This study uses COSI-Corr to analyze the surface deformation of the Lingding Fault in the 2018 Hualien earthquake with orthorectified aerial photos taken before and after the earthquake. The result of horizontal displacement will be further analyzed by the half-space elastic dislocation model to estimate the Lingding Fault's geometry and fault slip at the shallow depth. After obtaining the shallow fault geometry and slip characteristics of the Lingding Fault, we then discuss the relation between the Lingding Fault and the regional geological setting associated with the 2018 Hualien earthquake.

doi:10.6342/NTU202202354

2. Geological Background

The eastern Taiwan is one of the most seismically active regions around the world, resulting from the oblique collision of the Eurasian Plate, the Central Range Block, and the Philippine Sea Plate (Shyu et al., 2005). The Coastal Range, belonging to the northern part of the Luzon volcanic arc on the Philippine Sea Plate, moves northwestward at a rate of 85-90 mm/year relative to the Eurasian Plate (DeMets et al., 2010; Yu et al., 1997a). The collision forms the nearly N-S trending Longitudinal Valley Suture between the Coastal Range and the Central Range Block in eastern Taiwan, representing a major plate boundary between the Philippine Sea Plate and the Central Range Block/ Eurasian Plate (Barrier & Angelier, 1986; Chemenda et al., 1997; Sibuet & Hsu, 2004; Teng, 1990). Along the Longitudinal Valley Suture, several east-dipping active faults can be found at the western edge of the Coastal Range, including the Chishang Fault, the Rueisuei Fault, and the Lingding Fault from south to north, based on the geological and geodetic evidence (陳等人，2008). These active faults form the Longitudinal Valley Fault system that transects through the entire Longitudinal Valley in eastern Taiwan (Peyret et al., 2011). At the base of the Central Range's eastern mountain front, the geomorphic evidence indicates the existence of the west-dipping Central Range Fault (Shyu et al., 2006). North of the Longitudinal Valley Suture, the

doi:10.6342/NTU202202354

Philippine Sea Plate subducts northward under the Eurasian Plate, forming the E-W trending Ryukyu Trench northeast of Taiwan (Wu et al., 2009) (Figure 2.1a). The junction between the collision and the subduction system is close to the northern end of the Longitudinal Valley and Hualien City, making the active tectonic settings near the northern termination of the Longitudinal Valley Suture complicated (Hsu et al., 2001). The 2018 Hualien earthquake occurred under such complex tectonic region in this area (Jian et al., 2018; Lee et al., 2018; Lo et al., 2019; Yen et al., 2018).

doi:10.6342/NTU202202354

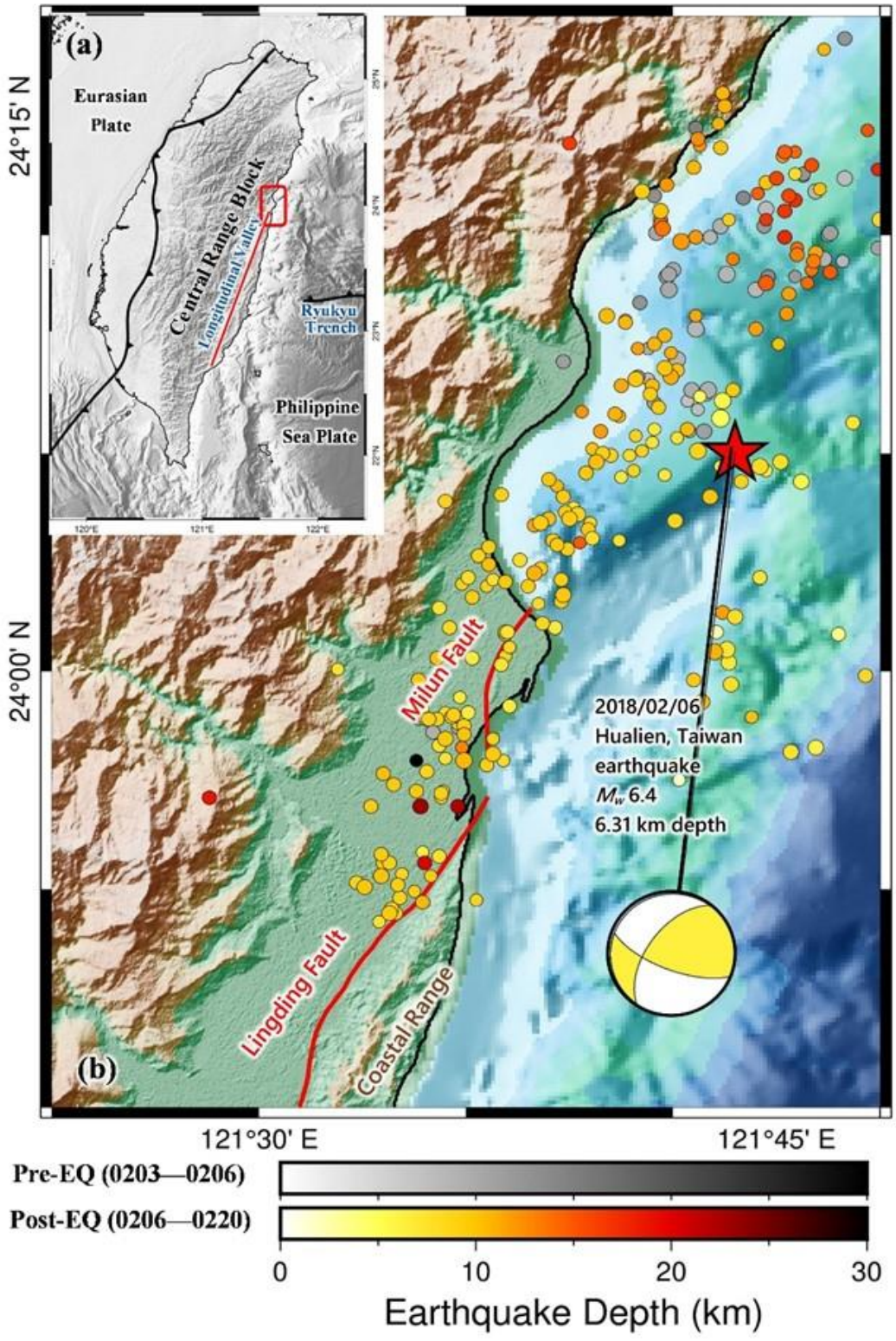

Figure 2.1 (a) The tectonic setting of Taiwan. (b) Active faults and the 2018 Hualien Earthquake sequence near Hualien City. The star symbol marks epicenter of the mainshock.

doi:10.6342/NTU202202354

The M_W 6.4 Hualien earthquake occurred offshore (about 16.5 km north) of Hualien City on February 6th, 2018 (Figure 2.1b). The focal depth is around 6.3 km deep (Jian et al., 2018; Lee et al., 2018). Based on the mainshock focal mechanism, a previously unidentified offshore structure with the N-S striking and west-dipping plane is the most possible seismogenic structure of this earthquake (Kuo-Chen et al., 2018; Lee et al., 2018; Wen et al., 2019; Wu et al., 2019; Yen et al., 2018). The slip of this offshore structure triggered the on-land Milun and Lingding Fault to rupture (Lee et al., 2018). By analyzing the seismic waves, Lee et al. (2018) suggest soon after the offshore structure started to slip, the rupture quickly propagated southwestward and made the Milun Fault begin to rupture. Eight seconds after the initial movement of the offshore structure, the Lingding Fault also started to rupture (Lee et al., 2018). More than 1000 aftershocks were detected within two weeks after the mainshock (Jian et al., 2018; Kuo-Chen et al., 2018; Lee et al., 2018). The distribution of these aftershocks is roughly in NE-SW trending (Kuo-Chen et al., 2018; Lee et al., 2018) (Figure 2.1b). The moment tensor solution of the mainshock is a significant non-double-couple, with a strong compensated linear vector dipole component (Jian et al., 2018; Lee et al., 2018; Toyokuni et al., 2021). Lee et al. (2018) explained this could be caused by the complex rupture processes on multi-segment fault planes or different fault systems. Jian et al. (2018) also had similar ideas, with varied slips and geometries on multi-segment faults.

doi:10.6342/NTU202202354

Toyokuni et al. (2021) found non-double-couple components dominant in both the 2018 and 2019 Hualien earthquakes. They elucidated these were related to structural anomalies, such as fluids from dehydration of the subducting slab.

Along the Milun Fault trace, the surface-rupture related deformations can be found right after the earthquake, including the *en echelon* tension cracks in the Meilun campus of the National Dong Hwa University (Hsu et al., 2019; Huang et al., 2019), liquefactions, and slope failures along the western edge of the Milun Tableland (Huang et al., 2019), etc. Many casualties and infrastructure damage are also related to the rupture of the Milun Fault. Results of optical correlation of satellite images suggest the shallow fault slip behavior is different between the northern and southern parts of the Milun Fault (Kuo et al., 2018). They also suggest the main rupture termination is closer to the surface in the northern part than in the southern part of the fault. It is likely because the southern half of the Milun Fault transects through the thick layers of young alluvial sediments with low cohesion near the surface. Overall, the Milun Fault shows the significant left-lateral motion with a slight reverse component during the 2018 earthquake. Based on the field measurement of fault surface offsets, Lin et al. (2019) suggest the maximum sinistral offset on the Milun Fault is more than 60 cm near the northern tip of the Milun Fault, and decreased southward to around 5 cm close to the southern end of the fault surface rupture.

doi:10.6342/NTU202202354

Compared with the Milun Fault, the Lingding Fault attracts less attention, partly because it locates in a rural area and with less damage to the community. The only measurable displacement on the Lingding Fault is at the Hualien Bridge, about 70 cm, as reported by the post-quake field survey (CGS, 2018; Lin et al., 2019). Along the Hualien River, surface cracks, sand blows (Ko et al., 2018), and slope failures can also be found along the northernmost Lingding Fault's inferred fault trace. The leveling result indicates the western side of the Lingding Fault uplifted, while the eastern side of the fault subsided during the 2018 earthquake (Figure 3.4c) (CGS, 2018). This movement pattern contradicts the previous understanding that the Lingding Fault is an east-dipping left-lateral fault with a reverse component (陳等人，2008). In Chapter 3, we will discuss more details about the results from previous geological studies related to the Lingding Fault and regional geological structure models.

doi:10.6342/NTU202202354

3. Review of Previous Studies

3.1 The geophysical studies about the Lingding Fault geometry

Although previous geological studies suggest the main trace of the Lingding Fault is mainly located in the Hualien River, and almost no outcrop of the fault can be found along its northernmost section (Wu et al., 2019; Zhao et al., 2020), several geophysical researches had been done to discuss the location, the geometry and the activity of the Lingding Fault prior to the 2018 Hualien earthquake. For example, the electric resistivity survey (簡立凱，2015) across the Lingding Fault at Yuemei area shows different strata properties across the purposed fault trace (Figure 3.1a). Two resistivity discontinuities were found along their survey line with both discontinuities not exposed to the surface. One of the discontinuities (between YM2 and YM3 in Figure 3.1a) is thought to be the fractured zone of the Yuemei Fault, which becomes wider in the deeper part of the profile. The resistivity data also suggest this fracture zone dips southeastward with a high angle. The other discontinuity (between YM6 and YM7 in Figure 3.1a) is covered by modern alluvial deposits and is thought to be the Lingding Fault. The hanging wall is composed of the high resistivity (>150 Ω-m) Tuluanshan Formation, and the footwall is interpreted as the low resistivity (<20 Ω-m) mudstone. The seismic

doi:10.6342/NTU202202354

reflection survey along the Mugua River by 謝一銘(2017) also provides constraints to the location of the northern Lingding Fault (Figure 3.1b). Their result shows continuous strong reflection beneath the Mugua River's alluvial fan without any offset found on these strong reflection signals. Hence, the location of Lingding Fault must be east of their seismic survey line.

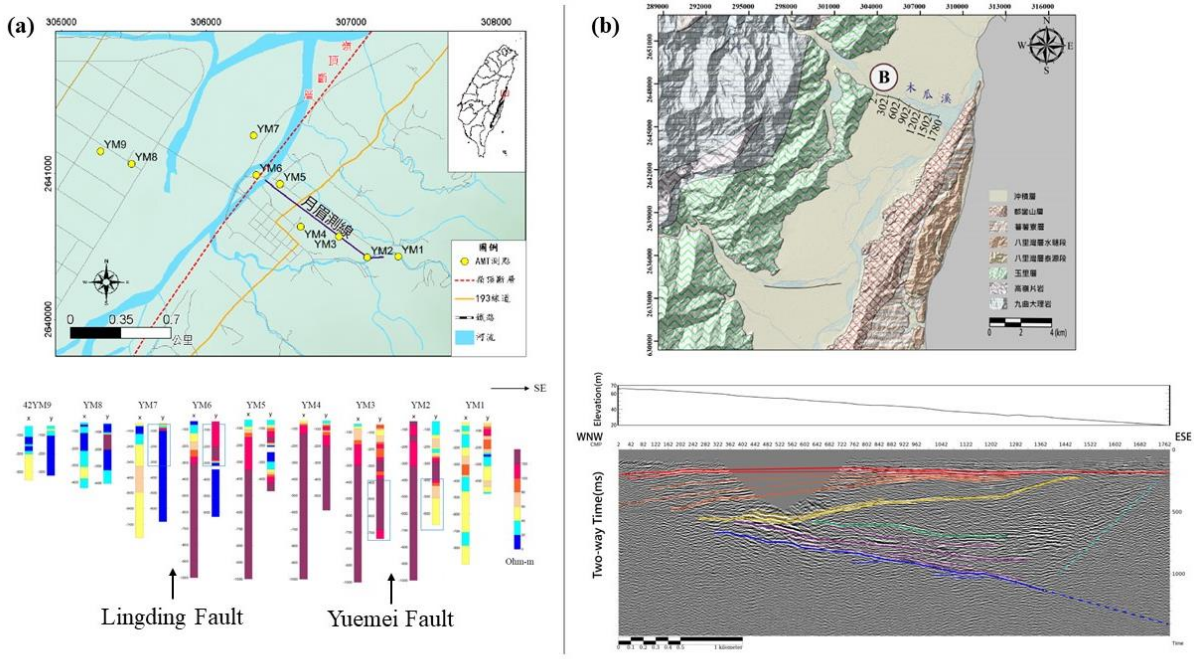

Figure 3.1 (a) The electric resistivity survey in Yueimei area (from 簡立凱，2015). Two discontinuities can be found in this survey line, which could be Lingding Fault and Yuemei Fault. (b) The seismic reflection survey along the Mugua River (from 謝一銘，2017). The color line in the lower figure is the strong reflection line, and the blue line could be the basement in this area.

For the interseismic behavior of the Lingding Fault, the Central Geological Survey used GPS to measure the ground displacement across the Lingding Fault from 2004 to 2006 (陳等人，2008) (Figure 3.2a). The geodetic analysis result shows no obvious

doi:10.6342/NTU202202354

fault-perpendicular velocity change across the Lingding Fault within the survey period. However, the Coastal Range moved 19.3 mm/year northeastward relative to the Central Range, which indicates the Lingding Fault is likely dominated by the left-lateral strike-slip motion. The PS-InSAR (Persistent Scatterers SAR interferometry) result shows that the Lingding Fault can be divided into three sub-segments (the boundary is at the latitude of 23.85° and 23.73°) based on the ALOS L-band SAR satellite data from 2007 to 2010 (廖昱茨，2014) (Figure 3.2b). The northernmost part of the Lingding Fault was relatively more active, with a slight velocity change across the Coastal Range and the Lingding Fault, than the rest of the fault. From the north to south, the observed mean Line-of-Sight (LOS) velocities of three sub-segments are 0 - 10 mm/year, 7 - -7 mm/year, and 0 - 15 mm/year, respectively.

doi:10.6342/NTU202202354

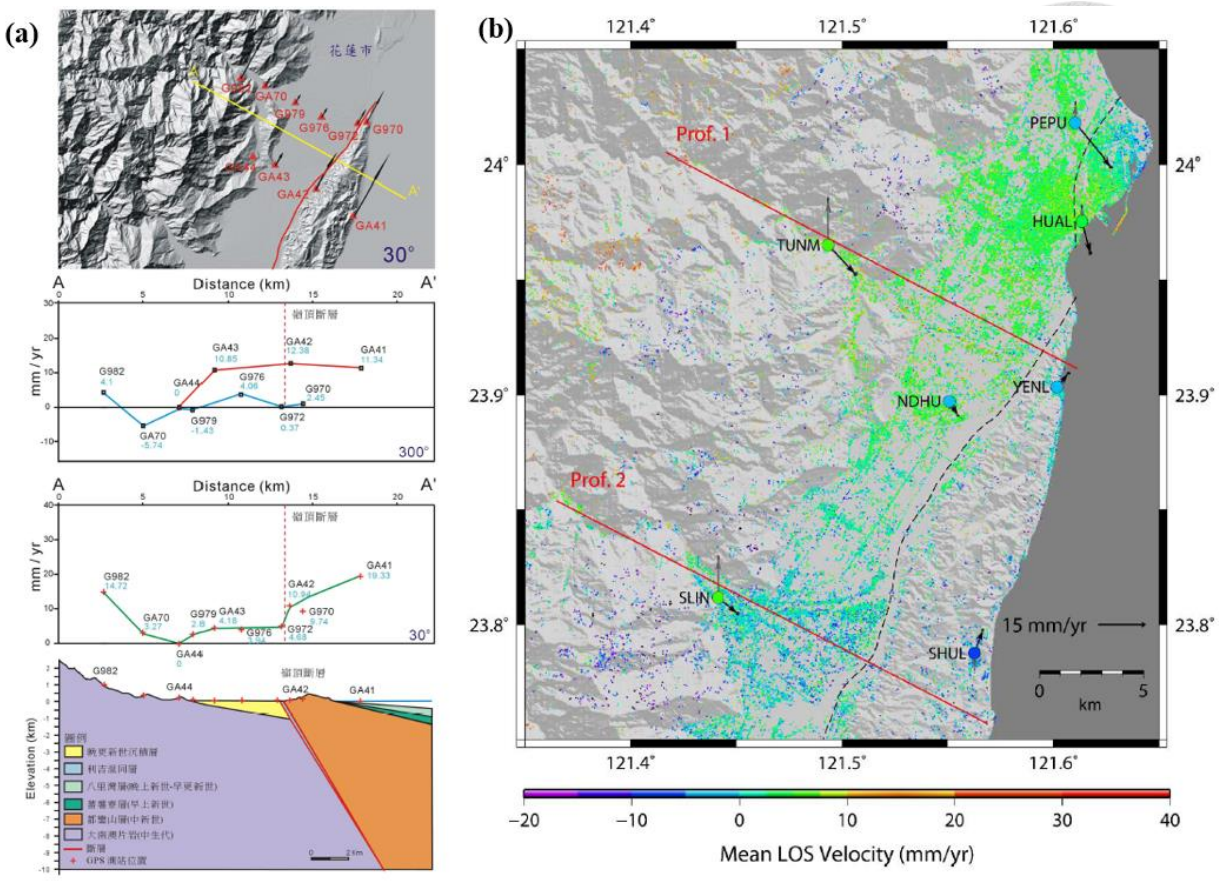

Figure 3.2 (a) The GPS result across the fault (from 陳等人，2008). The upper profile is the fault-perpendicular component of the velocity, and the lower profile is the fault-parallel component of the velocity. The velocity changes across the fault in the parallel component, but there is no obvious change in perpendicular component. (b) The result of PS-InSAR in northern Longitudinal Valley (from 廖昱茨，2014). In the northernmost of the Lingding Fault, the velocity is different for both sides. But the velocity is similar in southern part.

A few studies also used seismicity, tomography and seismic wave velocities to discuss the Lingding Fault's geometry underground. Chen et al. (陳等人，2018) used the relocated seismicity from 1900 to 2016, and the published tomography from Huang et al. (2014) to investigate the seismogenic geological structures in eastern Taiwan (Figure 3.3). Their result indicates that the northern part of the Longitudinal Valley Fault (Lingding Fault) dips 75° to the east from the surface to 30 km depth, and the

doi:10.6342/NTU202202354

fault becomes gentler below 30 km deep, to about 60° - 70°. Both the Vs and the Vp/Vs change across the northern section of the Longitudinal Valley Fault. The footwall of the Lingding Fault shows high Vs and low Vp/Vs (<1.72), and the hanging wall is featured by low Vs and high Vp/Vs (>1.72). The seismicity within 50 km depth around the Lingding Fault can at least be divided into two groups. The first group happened in the hanging wall and within 10 km deep. Along the fault plane, there was not much seismicity, which suggests the shallow part of the Lingding Fault is likely locked. The second group is located between 30 and 45 km deep and roughly along the purposed fault plane. The focal mechanisms are dominated by the reverse fault motion. Kuochen et al. (2004) used the seismicity from 1991 to 2002 relocated by hypo-DD method to evaluate the structural geometry within the Longitudinal Valley Suture (Figure 3.4a). Based on the epicentral and hypocentral distributions, their result (profile C) shows the Longitudinal Valley has an east-dipping (50°) seismic zone. Therefore, they suggest the boundary between the Philippine Sea Plate and the Eurasian Plate dips to the east, and the Philippine Sea Plate bends and dips to the west. 鍾珮瑜（2019) used the relocated seismicity from January 2017 to May 2017, and the 2018 Hualien earthquake aftershocks series and found a group of seismicity located in the depth of 10 km to 15 km (profile $\overline{BB'}$ in Figure 3.4b), which is different from Kuochen et al. (2004). The

doi:10.6342/NTU202202354

distribution of seismicity is east-dipping, and the focal mechanisms are mainly normal fault and strike-slip fault motions.

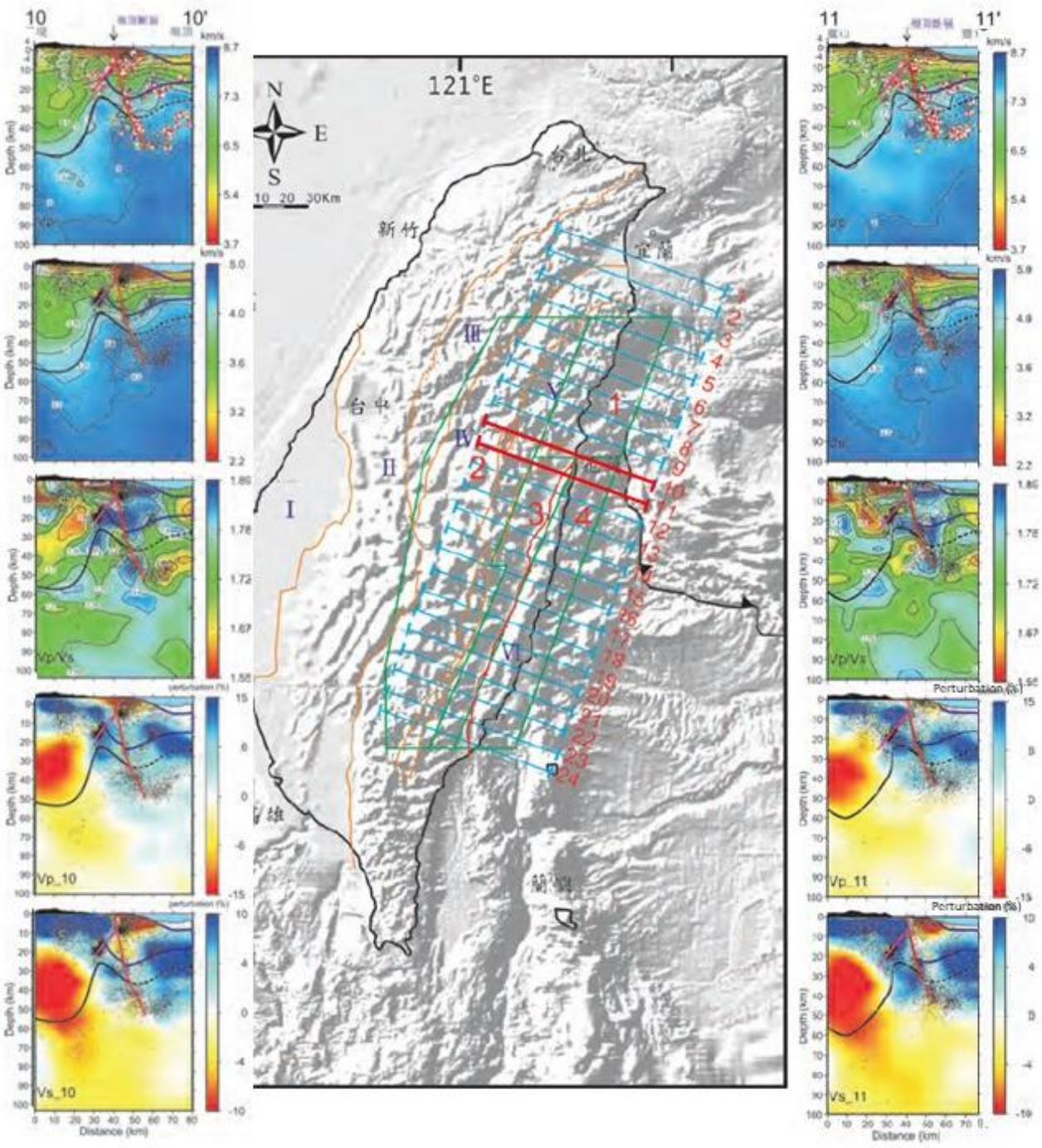

Figure 3.3 The seismicity, seismic velocity and tomography of the northern part Lingding Fault (modified from 陳等人，2018). A high angle east-dipping fault can be revealed.

doi:10.6342/NTU202202354

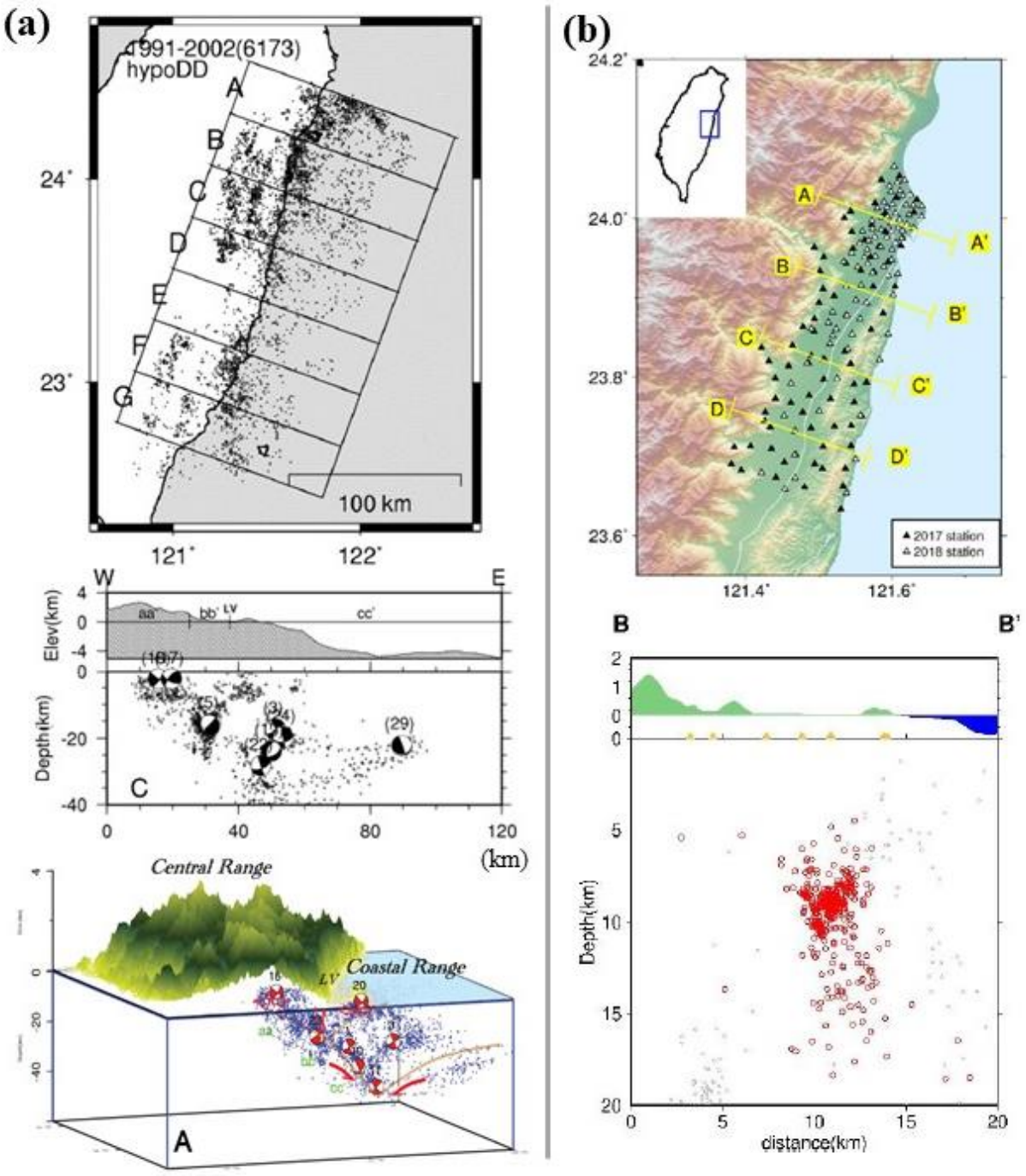

Figure 3.4 (a) The seismicity and focal mechanisms of the northern part Lingding Fault (from Kuochen et al., 2004). An east-dipping fault is also appeared, but the slope is gentler and locates more west. (b) The seismicity result of the northern Lingding Fault (from 鍾珮瑜，2019). A group of seismicity locates in the depth of 10 to 15 km. The distribution is nearly an east-dipping fault.

doi:10.6342/NTU202202354

3.2 The 2018 Hualien earthquake-related studies

While most post-earthquake researches focused on the Milun Fault and its associated surface rupture during the 2018 Hualien earthquake, several studies addressed or partially addressed the ground deformation and surface rupture of the Lingding Fault. Among these studies, only few of them focused on the deformation pattern associated with the Lingding Fault during the 2018 Hualien earthquake, and the role it played in the regional geological framework. The following is a brief summary of what previous studies have discussed.

Many different geophysical methods have been used to study the fault behaviors during the 2018 Hualien earthquake, such as seismology, remote sensing, Global Navigation Satellite System (GNSS), etc. Kuo-Chen et al. (2018) used 70 temporal vertical component seismic stations to record the aftershocks (February 8th – February 19th) near the Milun Fault and the Lingding Fault region (Figure 3.5a). The recorded seismic waves were analyzed to calculate the focal mechanisms and the locations of these aftershocks. The focal mechanisms show that this region is extension-dominated, which could be related to the post-seismic stress relaxation. The profile ($\overline{BB'}$ in Figure 3.4b) near the northern tip of the Lingding Fault illustrates a swarm of aftershocks distributed from 5 km deep to 15 km deep, and another small group of aftershocks were within 5 km deep. With the focal mechanisms, they suggest a west-dipping left-lateral

doi:10.6342/NTU202202354

fault with the normal component exists in this area. Further south to the Shoufeng area, a deep (5-15 km deep) swarm of aftershocks also presented, with a similar focal mechanism. They explain the geological structure here is a large strike-slip fault flower structure, and the Milun and Lingding Fault is part of this flower structure. They also agree that the deeper main structure triggered the slip on shallow faults (the Milun and Lingding Fault). Lee et al. (2018) did the joint source inversion with seismic waves and Global Positioning System (GPS) ground displacements to analyze the rupture process (Figure 3.5b). Three asperities were found on three given fault planes. The asperity (asperity Ⅲ) on the Lingding Fault (Fault 3) was beneath the northernmost of the Lingding Fault. The joint inversion result suggests the slip was mainly thrust at the deeper part of the Lingding Fault, and became left-lateral at the shallow depth. The maximum slip of the asperity III was 119 cm. Tian et al. (2018) used the strong motion stations in Hualien to recover the ground displacements. Unfortunately, the distribution of strong motion stations around the northern part of the Lingding Fault is sparse, so detailed movement discussion based on this method is unknown. Nonetheless, the station HUA060, located in the northern part of the Lingding Fault and on the hanging wall of the fault, shows the northward displacement reached 26.77 cm, and the westward movement was about 14.34 cm. The vertical component indicates the downward motion of 2.61 cm, which is consistent with the pattern of the GNSS and

doi:10.6342/NTU202202354

leveling survey results reported by the Central Geological Survey (Figure 3.5c) (CGS, 2018). Toyokuni et al. (2021) calculated the 3D model of Vp, Vs, and Poisson's ratio (σ) by more than twenty thousand earthquakes from 2000 to 2011, to discuss the relationship between the 2018 Mw 6.4, the 2019 Mw 6.1 Hualien earthquakes and the regional geological settings (Figure 3.5d). The epicenter of these two earthquakes was located in the boundary between drastically change in seismic velocity and Poisson's ratio in the horizontal direction, with high-Vp, high-Vs and low-σ anomalies in the west (the Central Range), and low-Vp, low-Vs, and high-σ anomaly in the east (the Coastal Range). This boundary can be correlated well with the Longitudinal Valley Fault (LVF), in which the Lingding Fault is part of the fault system. Hence, they propose the two earthquakes were related to the LVF and its branches. With the σ-anomaly, they also indicate the ascending fluid dehydration from the Philippine Sea Plate could play a role in the cause of two damaging earthquakes.

doi:10.6342/NTU202202354

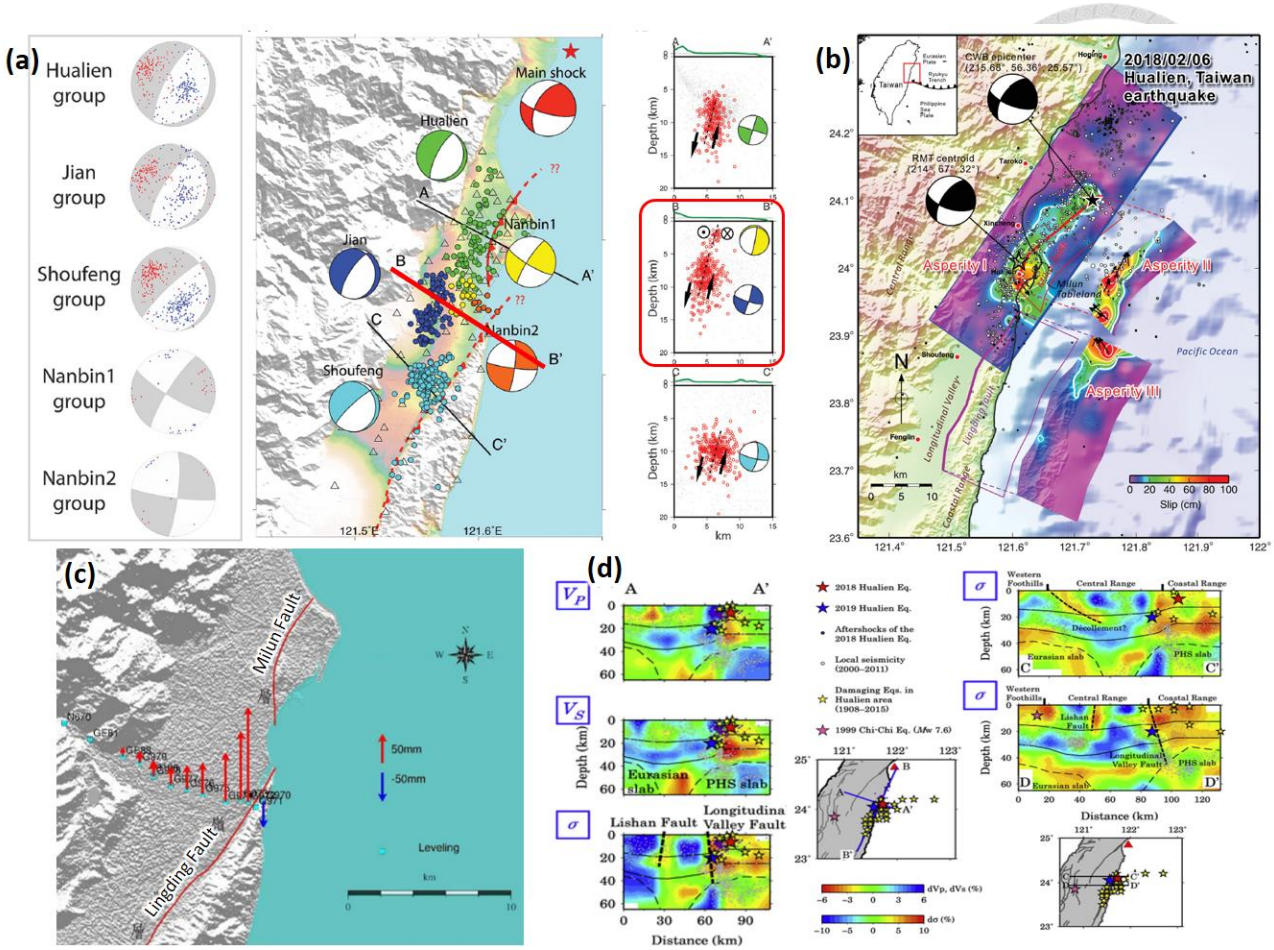

Figure 3.5 The related previous researches used seismic method to study this area. (a) The distribution and focal mechanism of aftershocks in 2018 Hualien Earthquake (Modified from Kuo-Chen et al., 2018). (b) The fault slips and asperities in this event (from Lee et al., 2018). (c) The levelling result after the 2018 Hualien Earthquake (modified from CGS, 2018). (d) The tomography and σ-anomaly in east Taiwan (from Toyokuni et al., 2021).

As for the geodetic analysis, Yen et al. (2018) used the GPS and the Differential Interferometric Synthetic Aperture Radar (DInSAR) with Sentinal-1 and ALOS-2 data to discuss the surface deformation in the 2018 Hualien earthquake (Figure 3.6a and 3.7a). Their DInSAR result shows the coseismic uplift (~1 cm) happened in the Longitudinal Valley, whereas the northernmost part of the Coastal Range was slightly

doi:10.6342/NTU202202354

subsided. This pattern qualitatively agrees with the results discussed before. For the profile near our research area (Profile D in Figure 3.6a), the Longitudinal Valley shows ~150 mm uplifting and southward motions, based on its motion toward the satellite on the ascending tracks. Their result also shows little movement for the Longitudinal Valley in descending tracks, implying limited E-W motion during the earthquake. Based on these results, Yen et al. (2018) proposed a strike-slip flower structure to explain the Milun and the Lingding Fault's geometries. They suggest the east-dipping Milun and Lingding Fault would become sub-vertical at the greater depth, and play the role of a backstop for the offshore thrust system (Figure 3.9c). Tung et al. (2019) used similar materials as Yen et al. (2018) to discuss both the instantaneous coseismic deformation and the permanent displacement (Figure 3.6b). The GPS station (YENL) at the hanging wall of the Lingding Fault recorded a ~200 mm NW horizontal displacement. For the vertical component, the result also shows 35 mm subsidence on the Coastal Range, while the station (NDHU) at the Lingding Fault's footwall recorded the coseismic uplift movement. From their InSAR results, the footwall of the Lingding Fault became shortening along the Line-of-Sight (LOS) direction, indicating this area was uplifted and/or moved westward. They suspected the west-dipping Central Range Fault meets the Lingding Fault at a deeper depth, which could explain the unknown west-dipping seismogenic structure in the 2018 Hualien earthquake. Zhao et al. (2020) used InSAR

doi:10.6342/NTU202202354

analysis from Sentinel-1 data, GPS, and teleseismic data to discuss the multi-fault complex rupture during coseismic and afterslip in this region (Figure 3.8b). They not only present the widely used three fault planes setting, including the west-dipping Milun and Lingding Faults on the surface, but also add a relatively flat north-dipping detachment fault. Although the fault slip pattern on the Lingding Fault is slight different to other studies (e.g. Huang & Huang (2018); Lo et al. (2019); Yang et al. (2018)), the largest slips are all located at the northern tip of the fault plane. Their result also shows coseismic and postseismic slip patch overlapped in the shallower depth, around 5 km deep. Lo et al. (2019) discussed the fault slip of offshore seismogenic structure, the Milun and Lingding Fault by joint inversion of teleseismic, strong motion, GPS and SAR data (Figure 3.8d). They also used InSAR, GPS and aftershocks data to search for the optimal fault geometry. Although the best fitting for the Lingding Fault is a high angle (86°) west dipping fault plane, they considered it as a sub-vertical fault. The result of fault slip on the Lingding Fault shows the largest movement happened in the northernmost end, and extended within 5 km deep. For their afterslip inversion from the SAR data, the fault slip mostly occurred on the middle part, which seemed to compensate the coseismic rupture gap. Wu et al. (2019) utilized the survey result from the Real Time Kinematic (RTK) GNSS network from April 8th to June 16th, 2018 to discuss the surface displacement pattern from the Milun Fault to the Lingding Fault

doi:10.6342/NTU202202354

(Figure 3.7b). Their result shows in the west of the Lingding Fault, around the Mugua River, the displacement is around 404 to 480 mm in S to SW direction, and the displacement became smaller southward. Near the Yuemei area, about 5 km south of the Hualien Bridge, the offset of the fault almost vanished. The measurement also indicates the east of the fault was subsidence and the west of the fault, near the Hualien Bridge, showed great uplift.

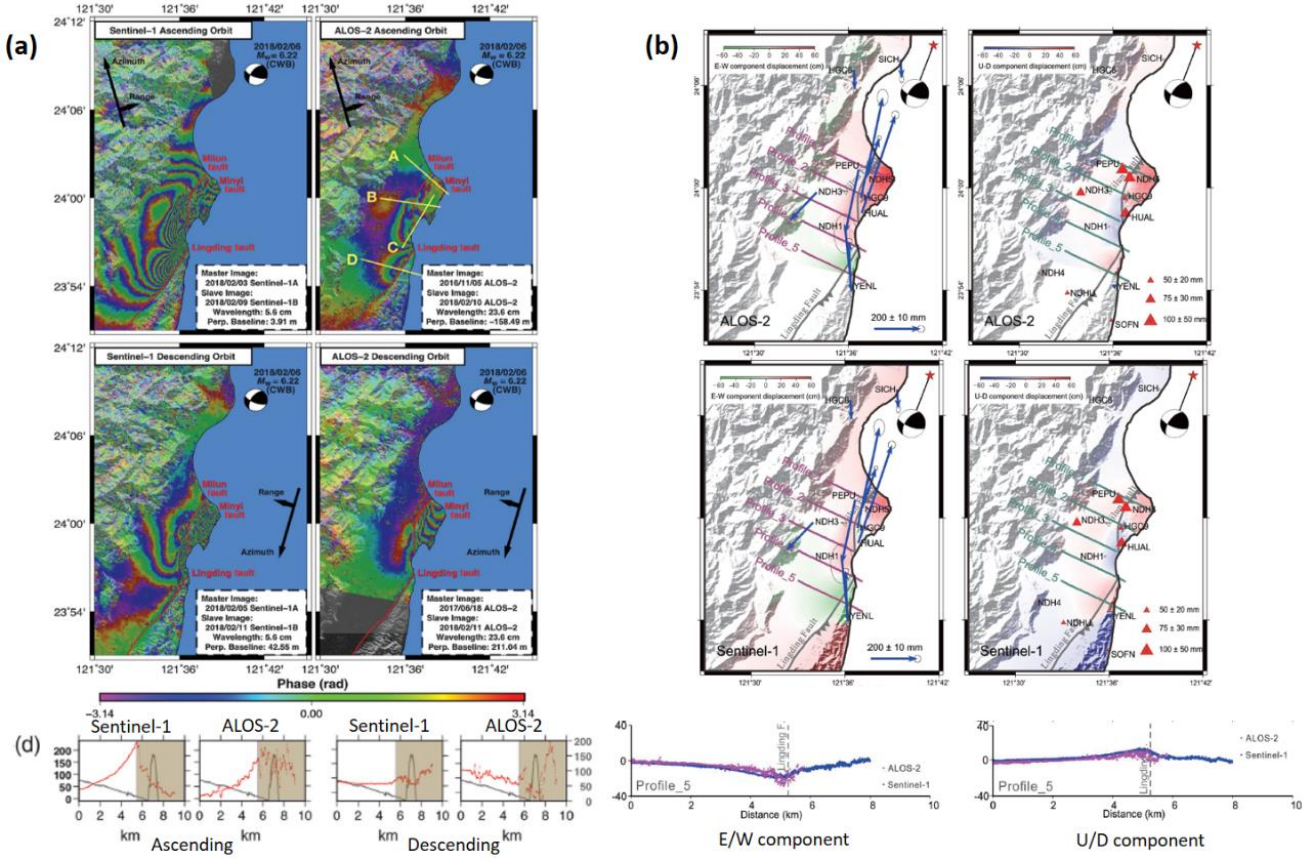

Figure 3.6 The InSAR results from previous studies. (a) The coseismic interferograms results (from Yen et al., 2018). The red line in profiles below is LOS deformation and gray line represents the topography. (b) The surface deformation derived from InSAR (from Tung et al., 2019). The purple dots in the profiles are deformation signals from ALOS-2, and the blue ones are from Sentinel-1.

doi:10.6342/NTU202202354

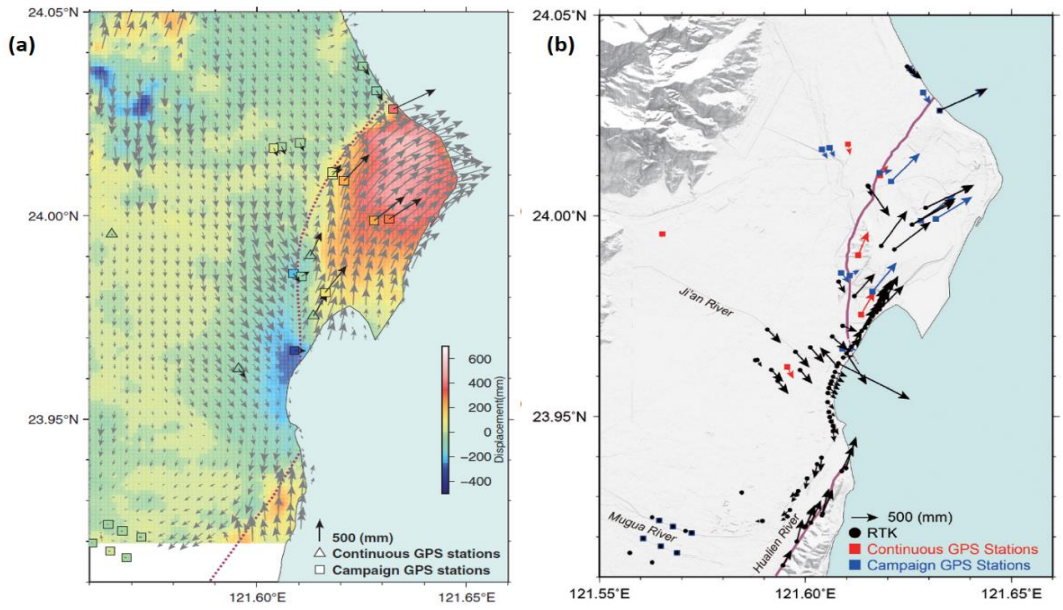

Figure 3.7 The coseismic surface deformation results. (a) The 3D surface deformation (from Yen et al., 2018). The arrow represents the horizontal displacement and the color means the vertical component. (b) The result of RTK and GPS stations (from Wu et al., 2019).

Other studies discussed the ground deformation patterns of the 2018 Hualien earthquake without considering the geological evidence of Lingding Fault, and were solely based on geophysical and geodetic observations. Yang et al. (2018) used the GPS and InSAR with Sentinal-1 and ALOS-2 images, similar to Yen et al. (2018) and Tung et al. (2019), to discuss the coseismic and postseismic model in this area (Figure 3.8a). However, the locations of faults are chosen only based on the ascending and descending InSAR data, which makes the Milun Fault the only same fault as the studies mentioned before. The high angle (85.2°) west-dipping fault mentioned in their studies is likely to

doi:10.6342/NTU202202354

be the Lingding Fault. Their multiple fault slip model indicates a slight slip occurred at shallow depth (0-8 km) in the northeastern end of this west-dipping fault. Interestingly, another relatively large slip happened in the deeper part (20-30 km deep) of this fault plane. Wen et al. (2019) investigated the rupture properties in this region by the inversion of teleseismic body wave and forward GPS displacement modeling. In their research, only two fault planes, a west-dipping offshore fault based on focal mechanism and an east-dipping fault based on geological evidence, were used in their model. The large slip patch, with left-lateral and slight down dip motion, was found on the southern and central parts of the east-dipping fault plane. If we compare this east-dipping fault with the location of the Milun and Lingding Faults, the larger slip patch is from the southern part of the Milun Fault to the northern part of the Lingding Fault. Huang and Huang (2018) used seismic and geodetic data to discuss fault slip behavior during the 2018 Hualien earthquake (Figure 3.8c). Four fault planes were used in their inversion analysis, including a large west-dipping fault exposed at the western flank of the Coastal Range. They suggest this west-dipping fault is different from the Lingding Fault system, and could be very close in space near the surface.

doi:10.6342/NTU202202354

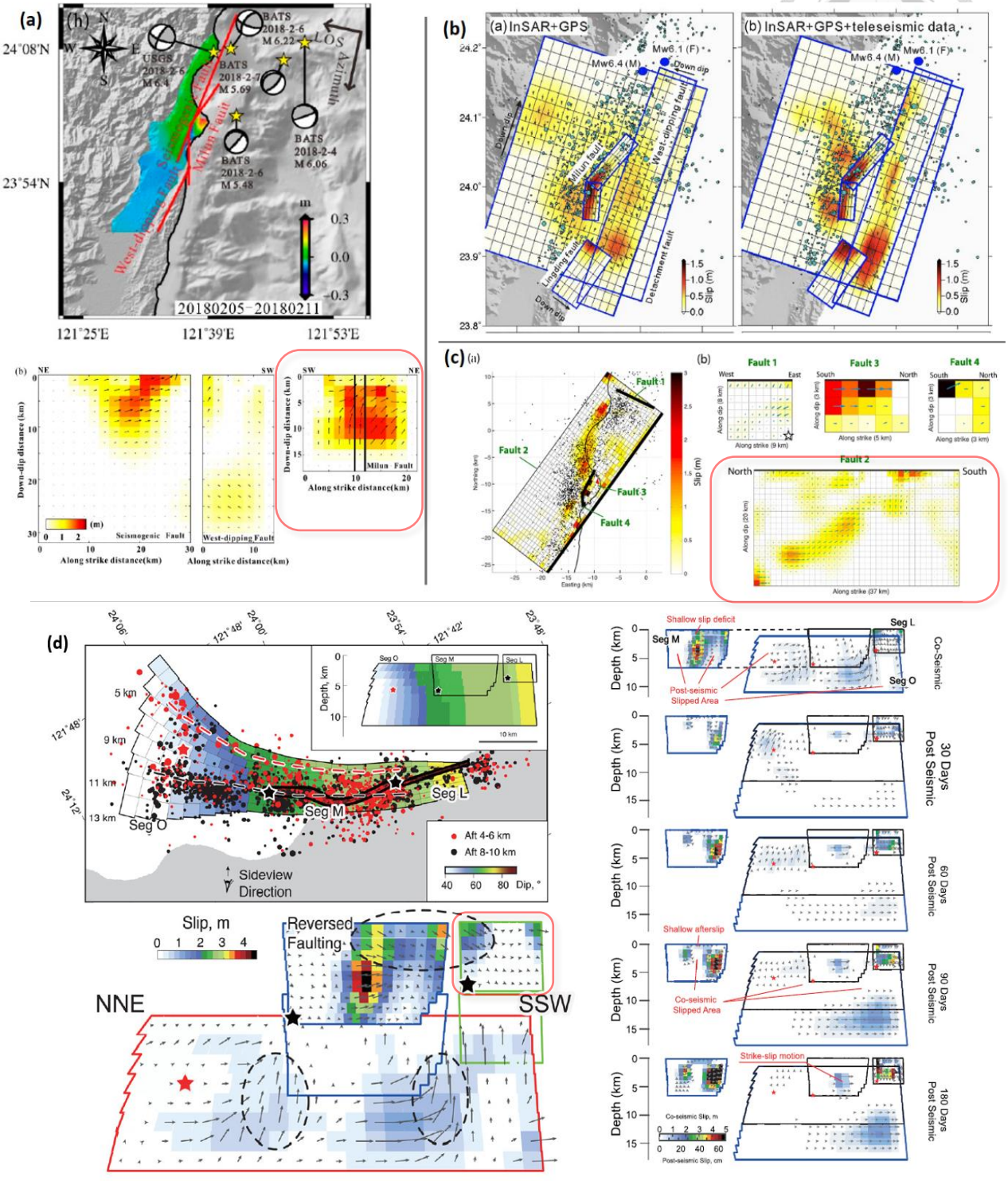

Figure 3.8 The fault slip results inversed mostly from InSAR and GPS. (a) is from Yang et al., 2018. (b) is from Zhao et al., 2020. (c) is from Huang & Huang, 2018. (d) is from Lo et al., 2019. The red rectangles are the potential fault settings related to the Lingding Fault.

doi:10.6342/NTU202202354

Although the aforementioned studies used different methods to discuss the displacement of the Lingding Fault and investigated the fault slip with different fault geometries, there are still some agreements on the motion of the Lingding Fault. For example, the hanging wall of the fault was subsidence and the footwall uplifted, and the surface deformation shows clear left-lateral motion between the Coastal Range and the Longitudinal Valley. Most of the slip inversion models also suggest that the largest slip occurred at the shallow depth near the Lingding Fault's northern tip. With the previous studies summarized here, we can notice that it still lacks a detailed discussion about the surface displacement and shallow fault slip of the Lingding Fault, especially based on the geological and geomorphological observations. Some of the geological structure models (Figure 3.9a – 3.9c) around the Milun and Lingding Fault are also proposed in the 2018 earthquake, and Shyu et al. (2016b) also built a model in this area (Figure 3.9d) based on the relocated seismicity, focal mechanisms of earthquake sequences, and tectonic geomorphology indication. All of these models have some differences and points of view. In this study, we will also try to suggest a geological model based on our results in this area.

doi:10.6342/NTU202202354

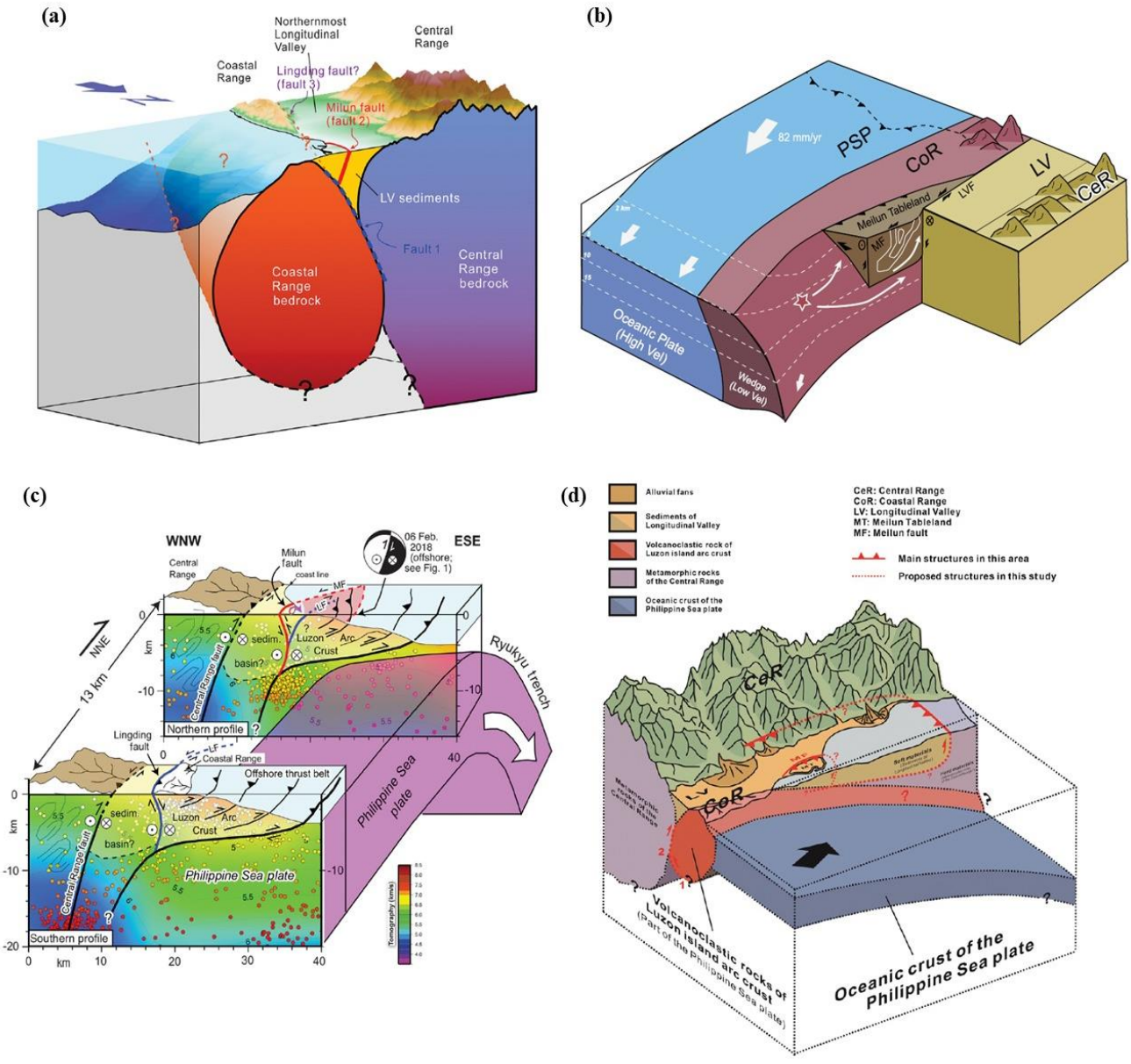

Figure 3.9 The different geological structures models in this area. (a) is from Lee et al., 2018. (b) is from Lo et al., 2019. (c) is from Yen et al., 2018. (d) is from Shyu et al. 2016b.

doi:10.6342/NTU202202354

4. Materials and Methods

Overview

In this study, we use aerial photos taken before and after the 2018 Hualien earthquake (chapter 4.1) to analyze the surface deformation and shallow fault slip of the Lingding Fault. Our study includes four main processes as described below: First, we use Agisoft Metashape Pro software to orthorectify and merge aerial photos into the pre- and post-event image, respectively (chapter 4.2). Second, we map the earthquake-related structures by visual inspections from these aerial photos (chapter 4.3). After locating the surface rupture through visual inspections, we use the software package COSI-Corr to perform the sub-pixel correlation and obtain the surface deformation map and estimate fault offsets along the Lingding Fault (chapter 4.4). We then use the half-space elastic dislocation model (chapter 4.6) to calculate the shallow fault geometry of the Lingding Fault, and the fault slip pattern at the shallow depth.

doi:10.6342/NTU202202354

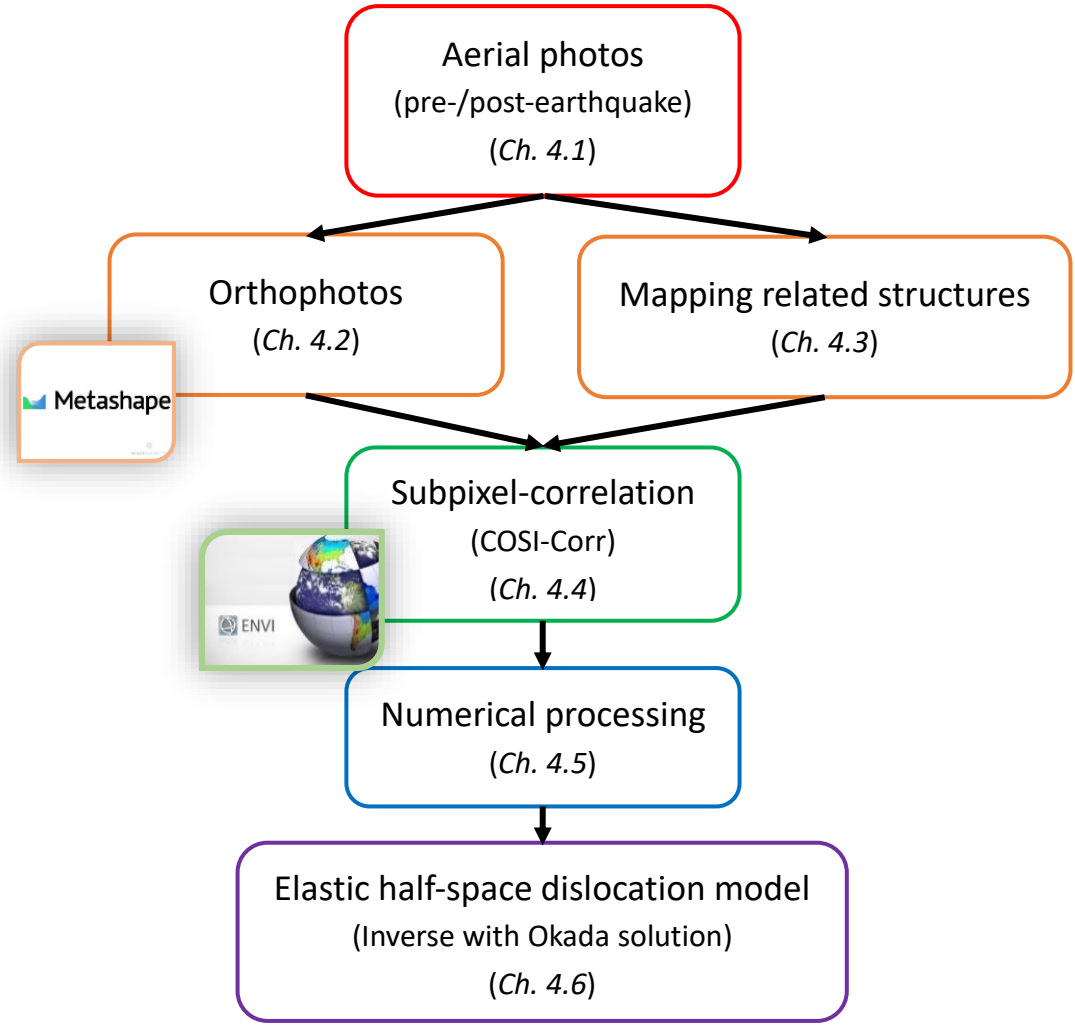

Figure 4.1 The general work flow in this study. For more detailed information, please see the corresponding chapters.

doi:10.6342/NTU202202354

4.1 Materials

The main material we use to analyze the near-fault ground displacement is the aerial photos taken before and after the 2018 Hualien earthquake. All these aerial photos were taken with the Digital Mapping Cameras (DMC) by the Aerial Survey Office, Forestry Bureau, Taiwan. We use ten pre-earthquake photos taken on October 27th, 2016 (around 1.5 years before the event) (Figure 4.2a), and eleven post-earthquake photos taken on March 4th, 2018 (1 month after the event) (Figure 4.2b) for our analyses. The resolution of these RGB aerial photos is about 0.25 m/pix, depending on their flight height. The overlap between these aerial photos is around 30% cross-track and 60% along-track to have better orthorectification results (Supplementary 1).

In addition to the DMC aerial photo, we also use the SPOT 7 optical satellite images (Supplementary 2) to validate our inspection results from aerial photo analyses. These orthorectified SPOT 7 images are obtained from the Center for Space and Remote Sensing Research, National Central University, with ground resolution of 1.5 m/pixel (Table 4.1). We use these satellite images to validate our aerial photo inspection result, since part of the post-event aerial images are covered by clouds at the eastern part of the Coastal Range (Figure 4.2b), and the shooting times of the satellite images are closer to the 2018 Hualien earthquake. The pre-event image was taken on October 18th, 2017, with an incident angle of 22.86°, and the post-event image was taken on

doi:10.6342/NTU202202354

February 18th, 2018, with an incident angle of 18.26° (Table 4.1). The small difference in their incident angle could reduce the topographic effect in the sub-pixel correlation analysis (Kuo et al., 2018).

Table 4.1 Summary of the materials used in this study.

Aerial photos		
	Shooting Date	**Photos Amount**
Pre-event	2016.10.27	10
Post-event	2018.03.04	11
Source	Aerial Survey Office, Forestry Bureau, Taiwan	
Satellite images (SPOT 7)		
	Shooting Date	**Incident Angle**
Pre-event	2017.10.18	22.86°
Post-event	2018.02.18	18.26°
Source	Center for Space and Remote Sensing Research, National Central University	

doi:10.6342/NTU202202354

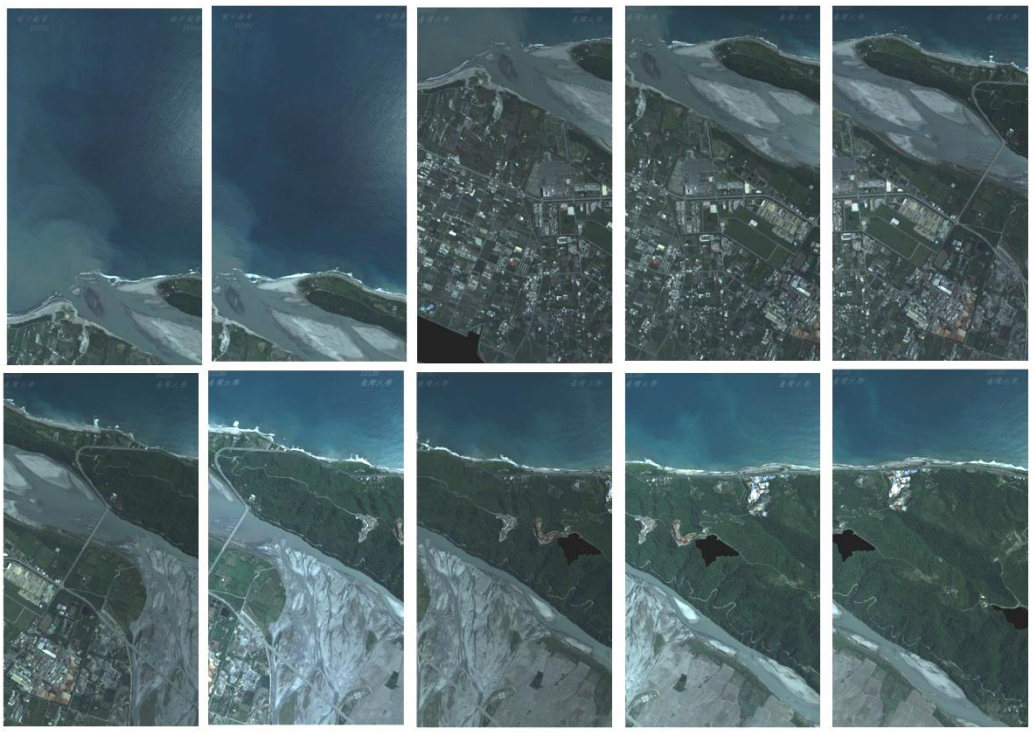

(a) Pre-event aerial photos (2016.10.27).

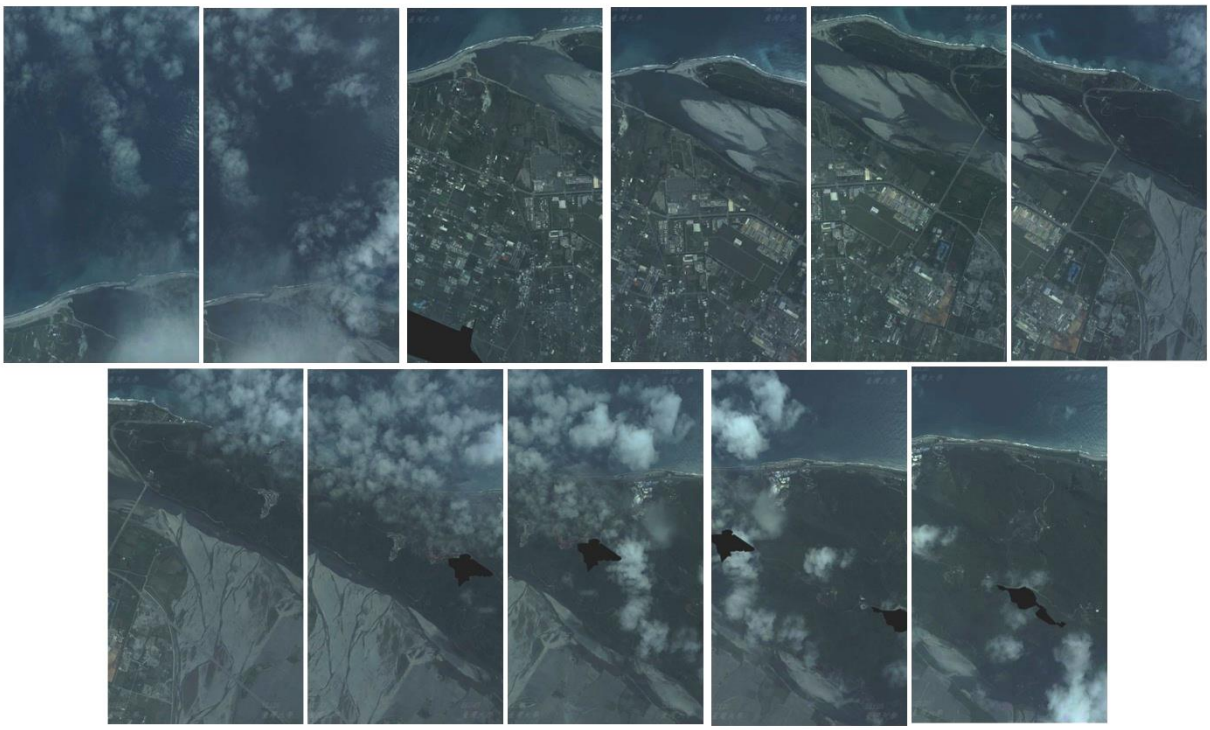

(b) Post-event aerial photos (2018.03.04).

Figure 4.2 The aerial photos used in this study. (a) Pre-event aerial photos. (b) Post-event aerial photos.

doi:10.6342/NTU202202354

4.2 The orthorectification of aerial photos

The Agisoft Metashape® Pro software is used to orthorectify and merge selected aerial photos into pre- and post-event images. The main algorithms used in this software are Structure from Motion (SfM) and Multi-View Stereo (MVS) (Bemis et al., 2014). Among them, SfM is the technique for computer to detect the same key features in a sequence of photos, i.e., the same building in different images. Because of the different looking angles to the key features in the photo sequence, the parallax can help to build a three-dimension model. By aligning these key features detected by the program with aerial photos taken in sequence and the constraints of focal length and pixel size (see table 4.2), an automated three-dimension sparse point cloud can be generated without geographic coordination constrained. The MVS is complementary to SfM, and can increase the number of matching points from different images with parameters estimated by SfM. The usage of MVS would refine the sparse points obtained by the SfM and generate a dense point cloud by pixel grid-based matching (Bemis et al., 2014).

In the past several years, the SfM-MVS technique has been widely used in the geosciences research field, with more and more scientists using this method to generate high-resolution 3D models from unmanned aerial system (UAS) imagery and classic aerial photos (Gomez et al., 2015; James & Robson, 2012; Piermattei et al., 2016; Saito et al., 2018). The software we use in this study is Agisoft Metashape® Pro (version

doi:10.6342/NTU202202354

1.6.3), which is reported to be more effective in the 3D model generation from classic aerial photos than other similar software (林亞嫻，2020). Our workflow for this step can be found in figure 4.4.

Table 4.2 The parameter of DMC photo used in this study.

Camera Type	Frame
Pixel size (mm)	0.012 × 0.012
Focal length (mm)	120

* Information from Forestry Bureau Aerial Survey Office (https://www.afasi.gov.tw/0000041)

To have proper geographic coordination and better alignment of aerial photos, the control points (CP), ground control points (GCP), and checkpoints (ChP) are given after the generation of the first dense point cloud (see Figure 4.4). The CPs are the key points that can be clearly identified in the photos, such as the corner of road signs and the art decoration on the ground. Our test result suggests that the inclusion of CPs can improve the alignment of both pre- and post-quake aerial photos. The GCPs are the CPs with geographic coordinates, including latitude, longitude, and altitude. We reference our GCPs to the point and the coordinate read from the web map of the National Land Surveying and Mapping Center, Ministry of the Interior. We also collect a few

doi:10.6342/NTU202202354

geographic feature points in the field using apps on the GPS-enabled mobile phone. However, because the precision of these points is low and thus we only use them as the checkpoints and do not use them in the image processing.

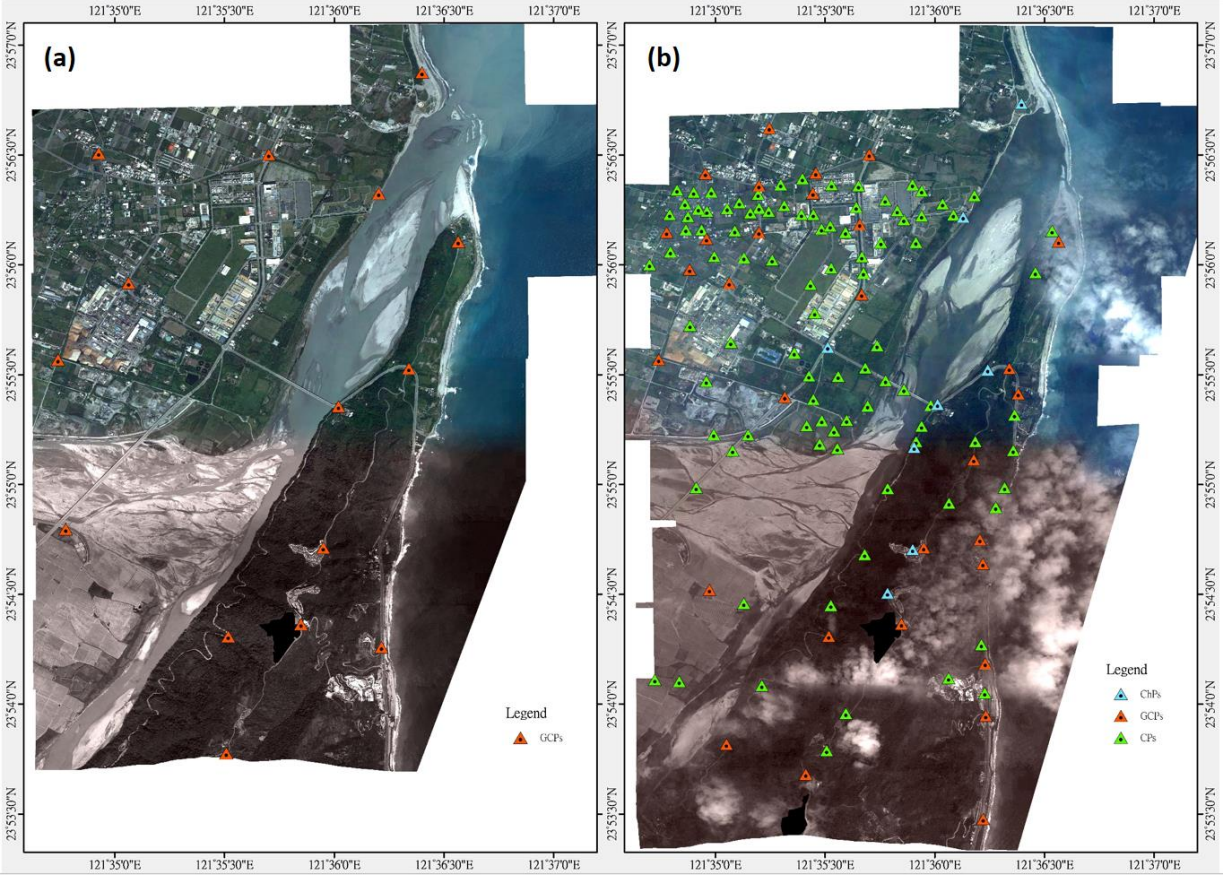

Figure 4.3 The location of GCPs, CPs, and ChPs in pre-event image (a) and post-event image (b).

After generating the dense point cloud for both pre- and post-quake aerial photos in different processing chunks, we align these two chunks to reduce the image shifting between the pre- and post-quake aerial photos. Because the post-quake point cloud suffers from some cloud coverage at the Coastal Range side, and the generation of 3D

doi:10.6342/NTU202202354

model at the Coastal Range side is significantly affected by these clouds, we, therefore, decide to merge the whole post-event dense point cloud with the extracted pre-event dense point cloud at the Coastal Range side to fill the data gap in the post-event's 3D model. Such procedure is done under the assumption of no significant internal deformation within the Coastal Range (i.e., >1 meter), so the pre- and post-quake 3D topography at the Coastal Range can be simplified as the block motion along the fault. To ensure such assumption won't significantly affect our result, we also use another way to examine our result by selecting only one side of GCPs to do the calculation (see Figure 4.5). Then, the Digital Surface Model (DSM) and orthomosaic photos are produced for pre- and post-event, respectively.

doi:10.6342/NTU202202354

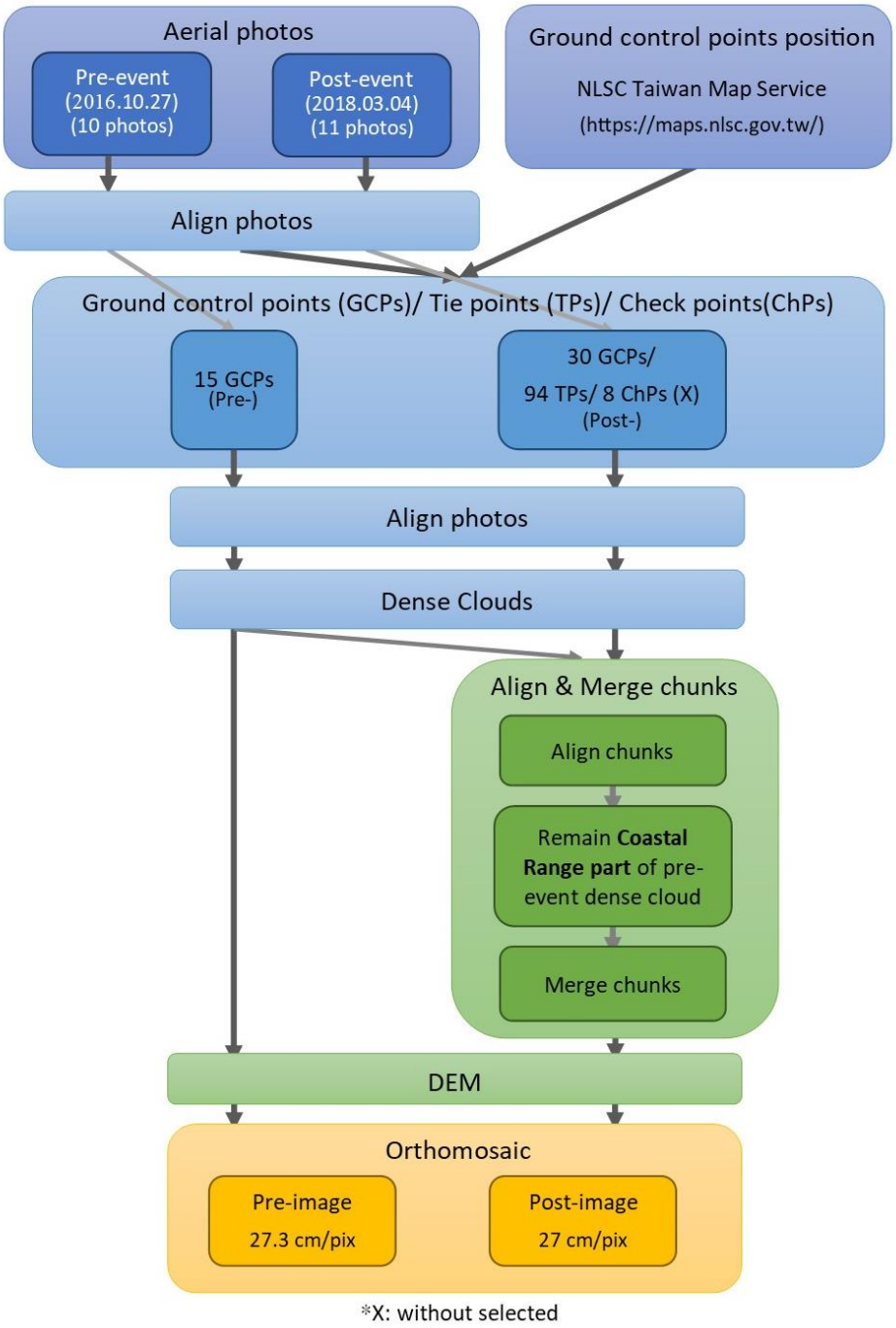

Figure 4.4 The workflow of the orthorectification of the aerial photos for pre- and post-event aerial photos.

doi:10.6342/NTU202202354

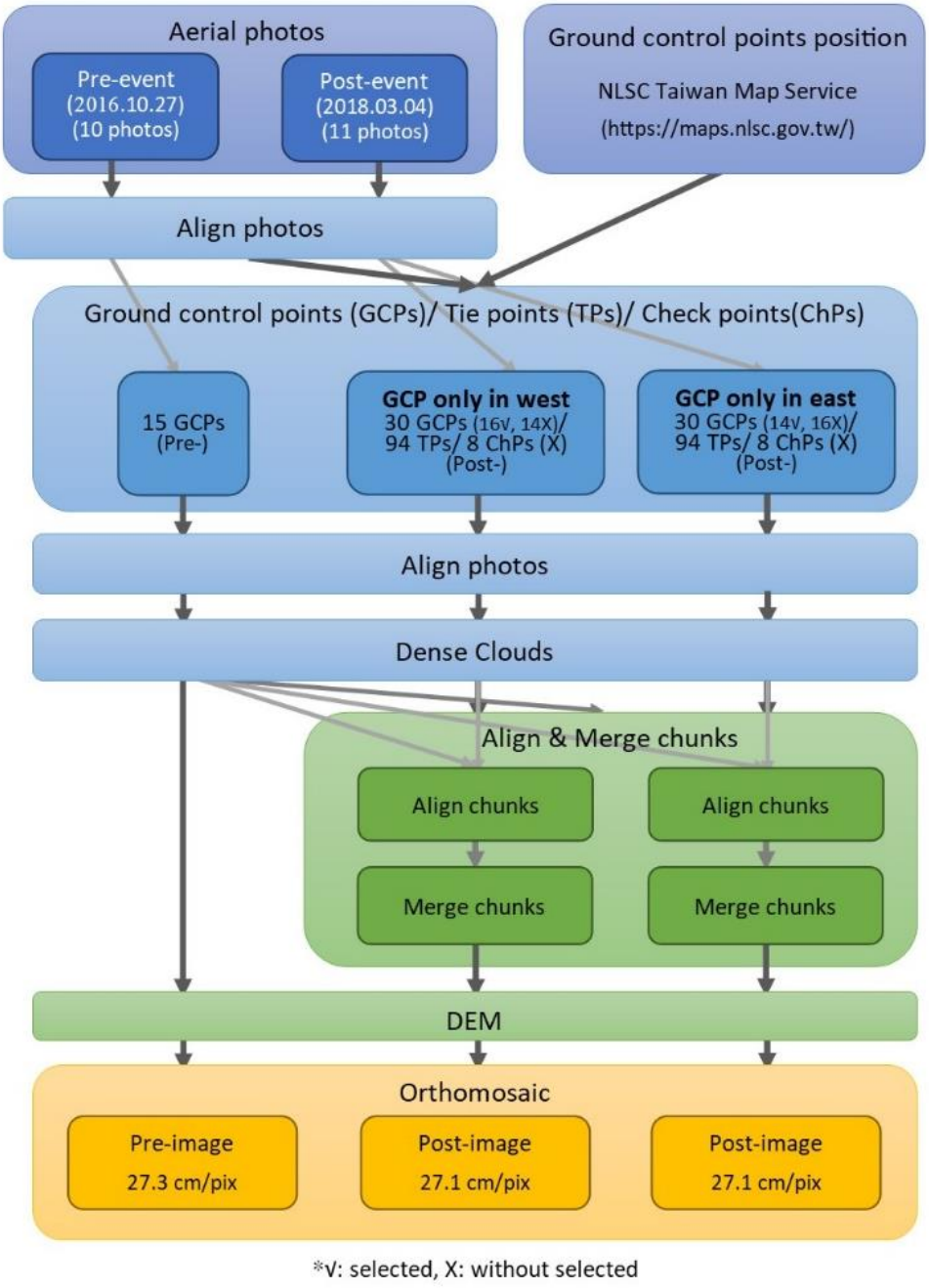

Figure 4.5 The workflow for examining the influence of the coseismic deformation during the orthorectification. We only selected one side of GCPs of post-event images to do the calculation.

doi:10.6342/NTU202202354

4.3 The mapping of earthquake-related structures

After generating the georeferenced orthomosaic aerial photos, we map the earthquake-related surface features by visual inspections of pre- and post-event aerial photos with ENVI and ArcGIS software. Since the shooting time of these aerial photos is not right before and after the 2018 Hualien earthquake, the difference found from our visual inspections can be not only caused by the coseismic surface ruptures, but also cause by other external processes, such as the fluvial erosion and deposition, or artificial modification. To reduce the temporal gap of our inspection, we also use the satellite imagery from Google Earth Pro to check the time series of satellite images, the time interval of the images is from one month to three months, to confirm the relationship between the surface features and the Hualien earthquake. In addition to the earthquake-related geomorphic features found from the aerial photo inspection, we also include results from the post-quake field surveys taken right after the 2018 Hualien earthquake by Central Geological Survey (CGS, 2018) and a previous study (Lin et al., 2019) in our mapping.

4.4 Sub-pixel correlation

The sub-pixel correlation is calculated using the Co-registration of Optically Sensed Images and Correlation (COSI-Corr) software package, working under the ENVI platform. The COSI-Corr has been widely used to study the ground deformation

doi:10.6342/NTU202202354

caused by earthquakes (Hollingsworth et al., 2017; Kuo et al., 2014; Kuo et al., 2018; Milliner et al., 2016; Milliner et al., 2015; Zinke et al., 2014), the migration of sand dunes (Baird et al., 2019; Hermas et al., 2012; Michel et al., 2018), and the change of the glaciers (Herman et al., 2011; Miles et al., 2021). Although this method can only get the horizontal displacement (E/W and N/S component), some studies (Kuo et al., 2014) used this method to discuss the three-dimension deformation with high precision ground control points information. The calculation of the relative displacement from the pair images relies on the phase difference of the Fourier transform (Leprince et al., 2007).

Suppose a point in image 1 (i_1) moves Δx and Δy in x and y direction, respectively, and becomes image 2 (i_2).

$$i_2(x, y) = i_1(x - \Delta x, y - \Delta y) \tag{1}$$

$$\xrightarrow{\text{Fourier transform}} \quad I_2(\omega_x, \omega_y) = I_1(\omega_x, \omega_y) e^{-j(\omega_x \Delta x + \omega_y \Delta y)} \tag{2}$$

$$\xrightarrow{\text{Normalized cross-spectrum of the images}} \quad C_{i_1 i_2}(\omega_x, \omega_y) = \frac{I_1(\omega_x,\omega_y) {I_2}^*(\omega_x,\omega_y)}{|I_1(\omega_x,\omega_y) {I_2}^*(\omega_x,\omega_y)|} = e^{j(\omega_x \Delta x + \omega_y \Delta y)} \tag{3}$$

$$\xrightarrow{\text{Inversed Fourier transform}} \quad F^{-1}\{e^{j(\omega_x \Delta x + \omega_y \Delta y)}\} = \delta(x + \Delta x, y + \Delta y) \tag{4}$$

I_1, I_2 are the Fourier form of the images, and the ω_x, ω_y are the frequency variables. * represents the complex conjugate.

doi:10.6342/NTU202202354

Before calculating the sub-pixel correlation, some pre-processing and post-processing are done to ensure better performance in calculation and displaying (Figure 4.6). The pre-processing includes transforming the unit of geo-coordination from the degree (latitude, longitude) to meter (UTM), merging the RGB bands into greyscale, and down-sampling the resolution to 1 m/pix in order to reduce the high-frequency signal interference of the images (Personal communication with Kuo, 2021). We also test three different window sizes for the correlation. These three window sizes range from 32×32 to 128×128 with the same step and other parameters in this research. After generating the correlation results from these parameters, we further truncate our result to ±1.5, ±2 or ±3 meters in both N/S and E/W directions to eliminate the noise from the water surface (e.g., ocean and rivers).

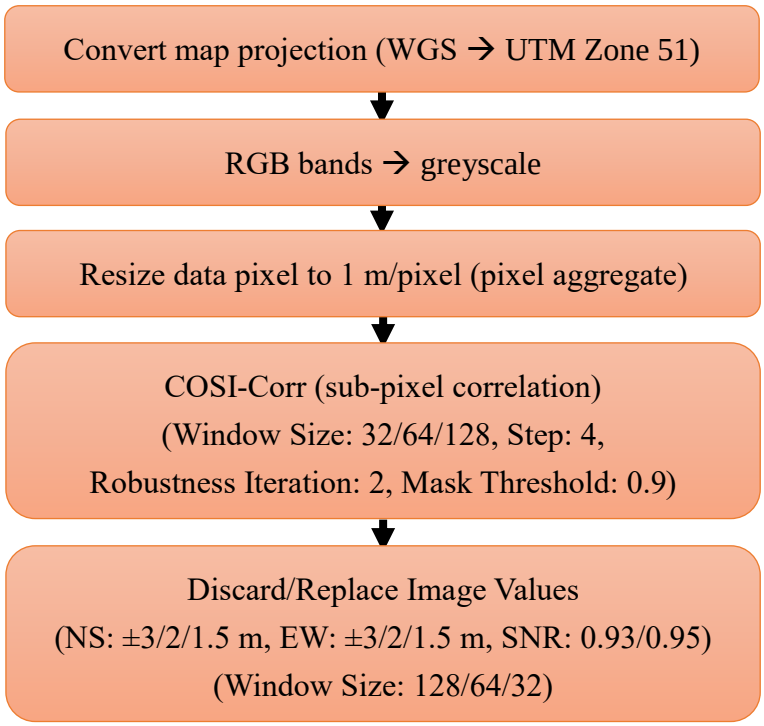

Figure 4.6 The work flow of the sub-pixel correlation, including pre-processing and post-processing in this research.

doi:10.6342/NTU202202354

To better understand the surface deformation along the Lingding Fault, we extract the ground deformation field along 13 profiles across the Lingding Fault from north to south (Figure 4.7). The dimension of each profile is 3450 m in length and 285 m in width for aerial photos, and around 3600 m in length and ~300 m in width for SPOT 7 satellite image.

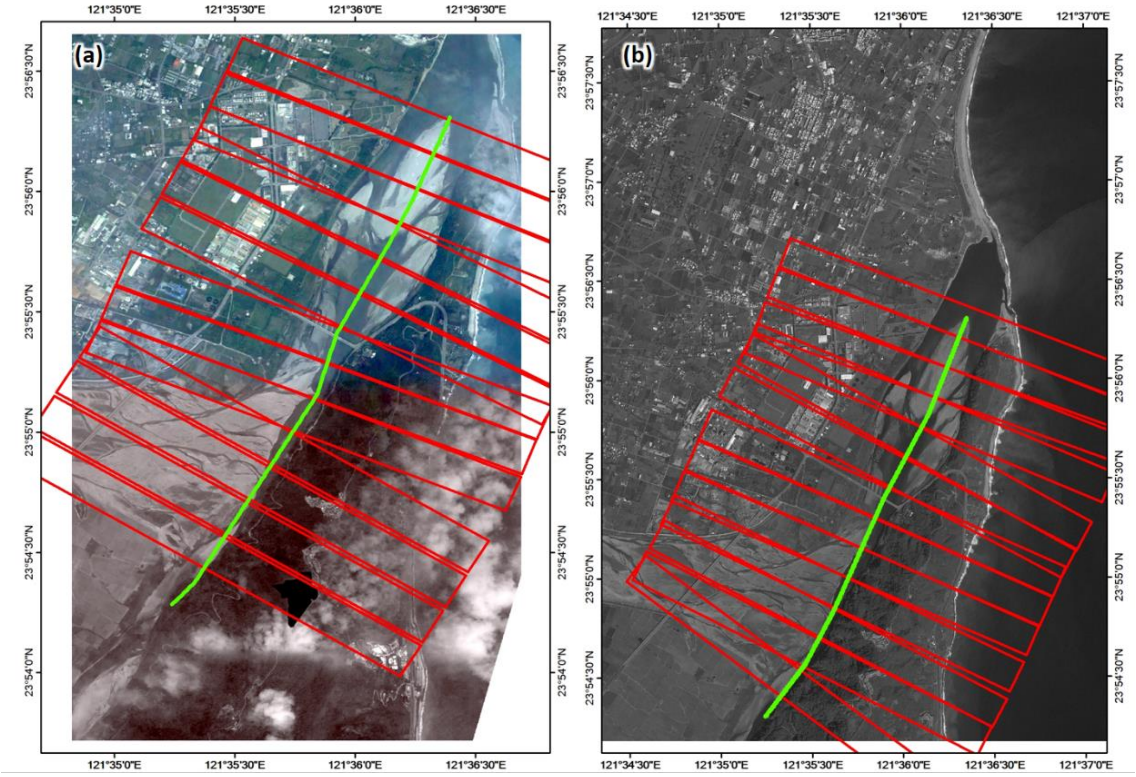

Figure 4.7 The location of the Lingding Fault and 13 profiles. (a) is for aerial photos, and (b) is for SPOT 7 images.

4.5 Numerical processing

The data within each profile is further filtered with two-stage numerical processing. These include outlier removal and linear regression. Although stacking profiles can

doi:10.6342/NTU202202354

make the result smooth, the quality of our profile result is still noisy, with the existence of extreme values along the profile. We use the moving average method to remove these outliers. In order to not affect the coseismic deformation estimation from these profiles, the moving average is applied from both end of the profile away from the Lingding Fault. The window size applied in these profile is 30 data points, and because our data is not always continuous, the average value and the standard deviation within the moving window would only be calculated when the number of data within the window is at least three. Then, the outliers would be removed when the value is not within one standard deviation (Figure 4.8). After the outlier removal, the linear regression would be calculated on each side of the fault. The difference in the values when two regression lines intersect on the fault is the displacement across the fault (Figure 4.9).

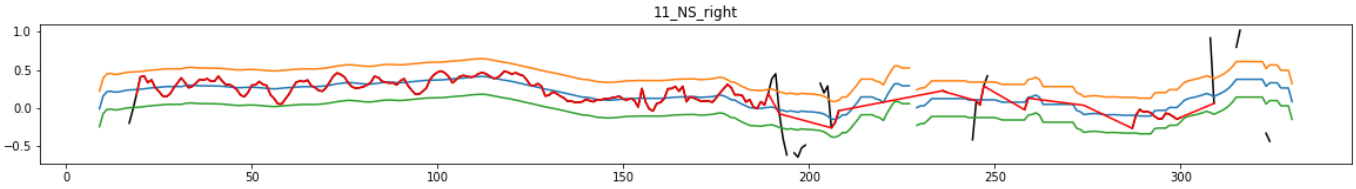

Figure 4.8 The condition to remove the outliers with moving average method, used profile 11 right part of NS component profile as example. The blue line is the moving average. The yellow and green lines are the upper boundary and lower boundary, respectively. The black line is the original data, and the red line is the data after filtering.

doi:10.6342/NTU202202354

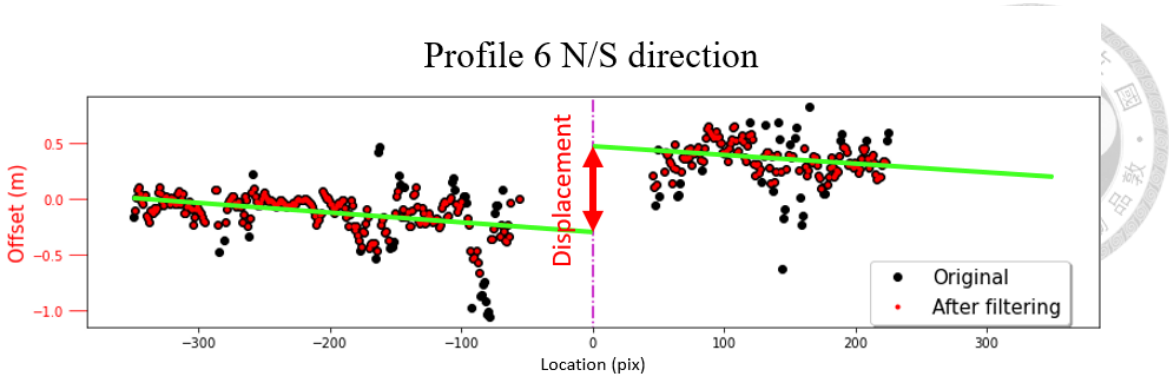

Figure 4.9 The offset across the fault (the red arrow). The green line is the linear regression line on each side. The black dots are the original data, and the red dots are the data after filtering the outliers. The purple dash line is the location of the fault.

4.6 Elastic half-space dislocation model

The elastic half-space dislocation model is used for the fault-slip inversion, in order to understand the pattern of shallow fault slip on the fault plane. The inversion model we use is based on the Okada half-space elastic dislocation model (Okada, 1985). We only use the horizontal displacement to inverse the strike-slip and dip-slip components. The fault strike is based on our mapping results (chapter 5.2), while the dip and length of the fault are tested with a range to find the optimal fault geometry in this earthquake. The fault bottom depth is decided by the checkboard test, and the fault top depth is set to 0 km. The fault strike is N29°E, which is based on the mapping result.

doi:10.6342/NTU202202354

$$\boldsymbol{d} = \boldsymbol{G} * \boldsymbol{m}$$

$$\begin{bmatrix} d_e^1 \\ d_n^1 \\ d_e^2 \\ d_n^2 \\ \vdots \\ \vdots \\ d_e^t \\ d_n^t \end{bmatrix} = \begin{bmatrix} ss_e^1 & ds_e^1 \\ ss_n^1 & ds_n^1 \\ ss_e^2 & ds_e^2 \\ ss_n^2 & ds_n^2 \\ \vdots & \vdots \\ \vdots & \vdots \\ ss_e^t & ds_e^t \\ ss_n^t & ds_n^t \end{bmatrix} \begin{bmatrix} ss \\ ds \end{bmatrix} \dots\dots\dots\dots (5)$$

$\boldsymbol{d}$: the displacement of surface movement (E/W and N/S direction) with t observation

$\boldsymbol{G}$: the matrix of the Okada model depending on the fault geometry setting

$\boldsymbol{m}$: the strike-slip (ss) and dip-slip (ds) of the fault

The Laplacian smoothing is applied to make the result close to real. The smoothing weighting factor is decided based on the trade-off curve (misfit-model roughness) (Supplementary 13).

$$\begin{bmatrix} d \\ 0 \end{bmatrix} = \begin{bmatrix} G \\ \alpha\nabla^2 \end{bmatrix} \mathrm{m} \dots\dots\dots (6)$$

∇^2: the Laplacian smoothing, α: the smoothing weighting factor (decided by the misfit-model roughness trade-off curve)

doi:10.6342/NTU202202354

5. Results

5.1 The orthorectification of aerial photos

Before orthorectifing the pre- and post-earthquake aerial photos, this study first examines the quality of DSM generated from these aerial photos to ensure the orthorectification result won't contain significant errors from their DSMs. The examination includes two different tests to check the quality of DSM: First, we compare the pre- and the post-DSM to verify if there are any large elevation discrepancies between these two datasets (Figure 5.1a), since we are not able to apply the same set of GCPs to the pre- and post-quake images. Second, we compare both the pre- and post-DSM with the published 20-m Digital Elevation Model (DEM) from the Ministry of the Interior (published in 2019) to check if our DSMs contain any systematical elevation errors (Figure 5.1b and c). For the first comparison, the difference between pre- and post-quake DSM is mostly within ±3 m. The differences larger than 3 m or smaller than -3 m are almost in the river or ocean, which is not the area we are concerned about. A small degree of elevation tilting is also found between these two DSMs along the NW-SE direction. Although some degrees of tilting happened between these two DSMs, the elevation at the center part of both DSMs shows good agreement to each other in both the Coastal Range and the Longitudinal Valley sides. For the second comparison,

doi:10.6342/NTU202202354

because the resolution of 20-m DEM is far lower than our DSMs (~0.5 m/pix), only ~40 - 50% area, mostly at the flat terrains, in our DSMs are within ±3 m compared to the 20-m DEM. In the city area (the western part), the larger difference can clearly display the outline of buildings and bridges. In the Coastal Range area, the differences between 20-m DEM and our DSMs are also larger than 6 m, which could be resulted from the height of vegetation. Since most of the elevation differences are in the Coastal Range side and the city area close to Hualien city, we suggest these differences are mostly resulted from the difference between the surface topography (DSM) and the bare-earth topography (DEM). Hence, we suggest the quality of the DSMs used for the later orthorectification of the aerial photos is acceptable.

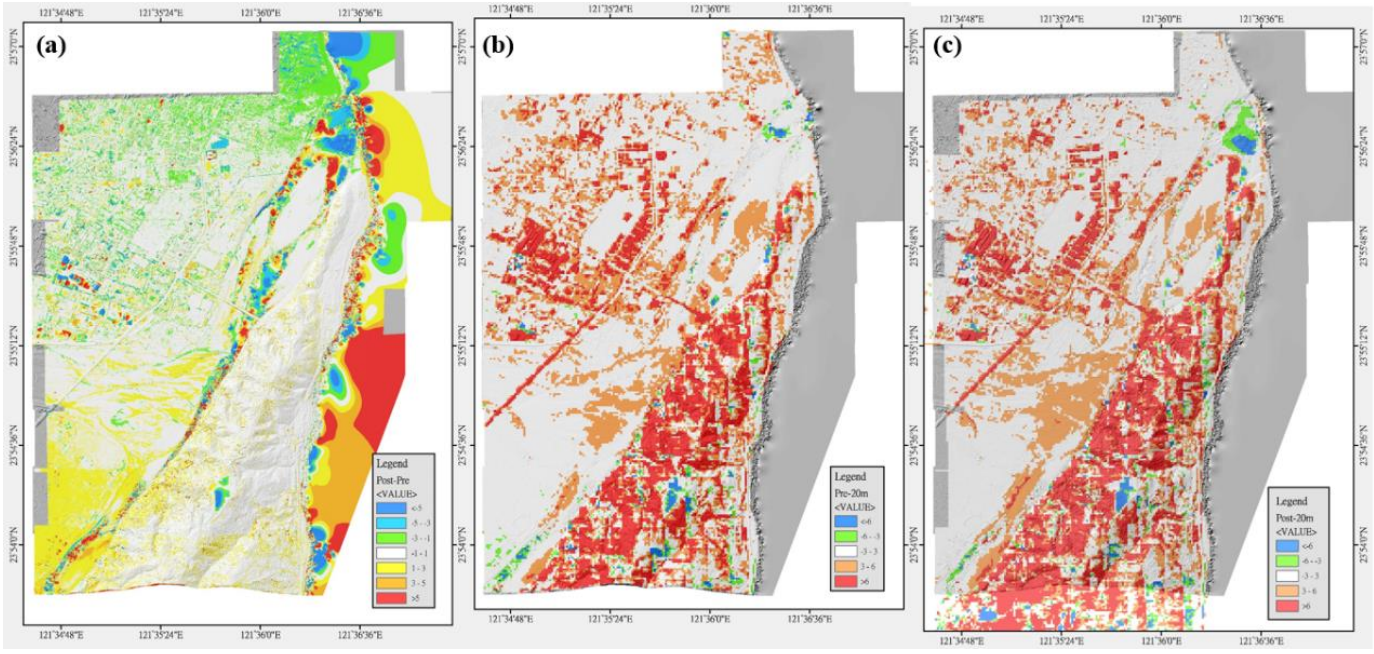

Figure 5.1 The comparison of the DSMs. (a) Comparison of pre- and post-DSM. (b) Comparison of pre-DSM and 20 m DEM. (c) Comparison of post-DSM and 20 m DEM.

doi:10.6342/NTU202202354

After orthorectifing with the DSM generated by the aerial photos, the resolutions of both pre- and post-earthquake orthorectified images are around 27 cm/pix. Figure 5.2 shows the orthorectification result of both pre- and post-quake aerial photos. Note that the eastern side of the Coastal Range is partly covered by the cloud, which is likely to affect our sub-pixel correlation result away from the Lingding Fault rupture.

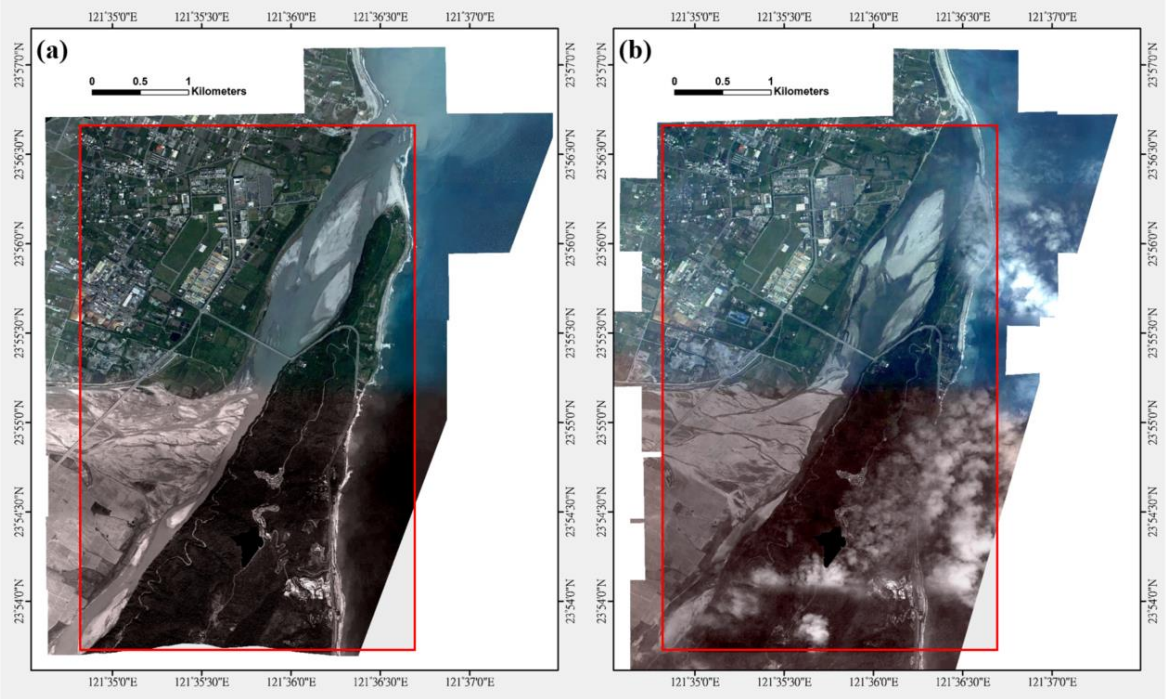

Figure 5.2 The result of orthorectification of the aerial photos. (a) is the pre-event image, and (b) is the post-event image. The red rectangle is the area used in the calculation of sub-pixel offset.

5.2 The mapping of earthquake-related structures

The earthquake-related features we map from aerial photos are mainly fault surface ruptures within the Hualien River. Based on the morphology of these ruptures, we divide them into three confidential levels. The first category is the rupture (red line in

doi:10.6342/NTU202202354

Figure 5.3), which we have the highest confidence in, owing to its clearly linear outline and only appearing after the earthquake (Supplementary 5a). This kind of rupture only shows in the northern Hualien River sandbar, between the Hualien Bridge and the Hualien River mouth. One of the linear structures cut through a grey belt on the southern end of the sandbar, showing clear left-lateral strike-slip motion (Figure 5.3 upper left and Supplementary 4). More interestingly, this structure can be traced southward into the water body, and can be distinctly identified after adjusting the color bands. These linear structures were not reported before, probably because these areas were not accessible after the 2018 earthquake. We also check the discharge record of the Hualien Bridge (from the Hydrological Year Book of Taiwan Republic of China https://gweb.wra.gov.tw/wrhygis/) to rule out the possibility of the effect of river erosion and transportation. The discharge record close to the pre-event aerial photo is 211.78 m^3/s on October 27th 2016 (97.88 m^3/s on September 23rd 2017 for the pre-event Google Earth Pro image), while the record close to the post-event is 87.50 m^3/s on March 4th 2018. The linear structure didn't appear in the higher discharge period; therefore the structure has a lower possibility related to river erosion. The second type of rupture is the suspected rupture, marked in yellow in Figure 5.3. This type of rupture has lower confidence than the first category, because its morphologies are not as clear as the first one, and it is possible that these suspected rupture features are related to the

doi:10.6342/NTU202202354

erosion of the river. However, our inspection shows that some of these suspected linear structures only appeared after the earthquake and are roughly aligned to each other, especially in the area south of the Hualien Bridge. Such spatial distribution makes us believe these features are associated with the Lingding Fault rupture during the 2018 earthquake. The third type is the uncertain rupture (Supplementary 6), in which we have the lowest confidence that these structures were related to the earthquake. Although they also have roughly linear appearances and are aligned to other features mapped from the aerial photos, some of these structures are hard to be identified even with the intense adjustment of the color bands to amplify their outlines. In addition, almost all of these uncertain features have blurred appearances, and they are hard to be validated by imagery in Google Earth Pro. The only clear one is in the southernmost part of the river (Supplementary 5c). However, we still cannot exclude the possibility that the water flow caused this structure.

doi:10.6342/NTU202202354

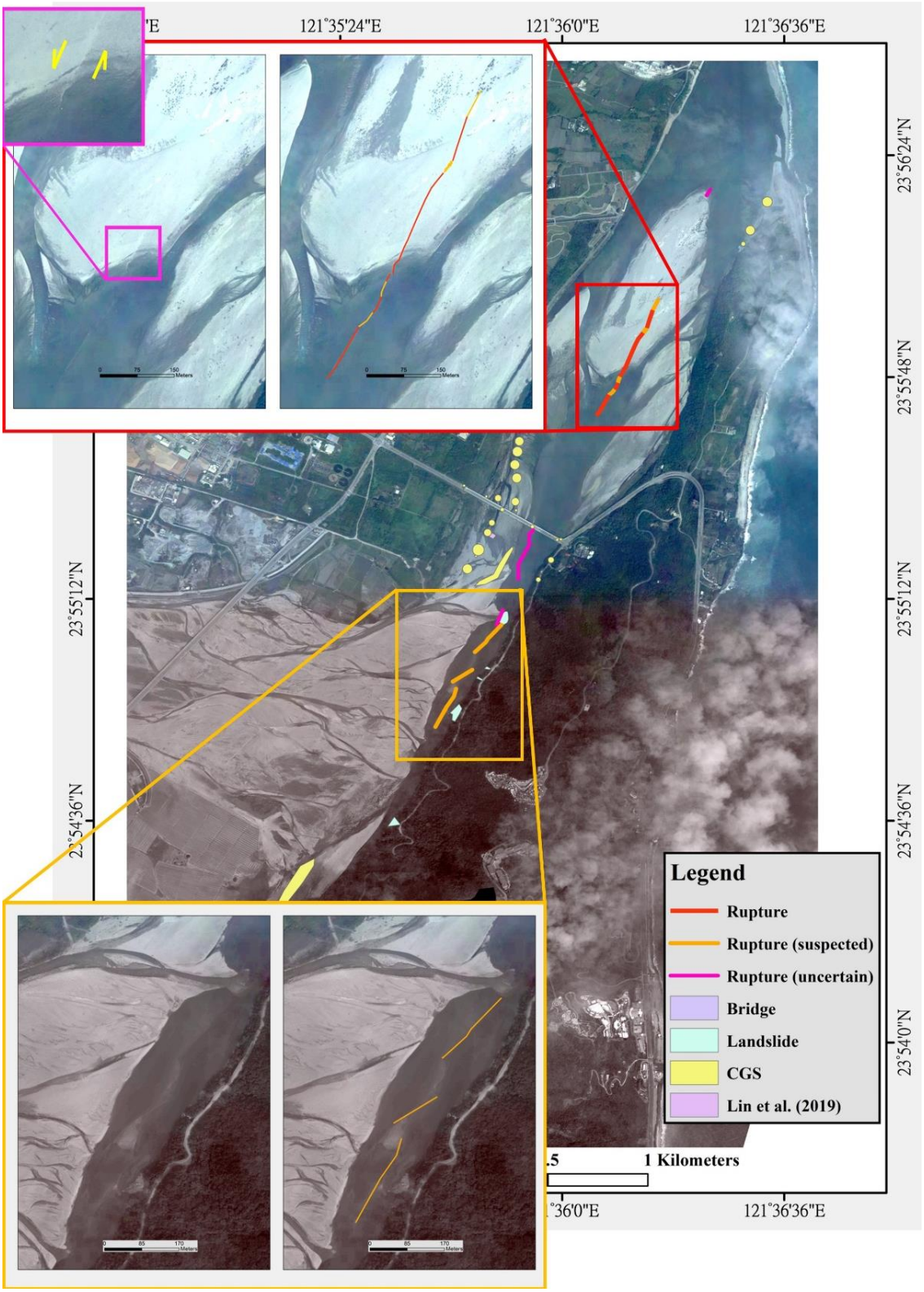

Figure 5.3 The earthquake-related structures we mapped, with the closer images of ruptures and suspected ruptures.

doi:10.6342/NTU202202354

Overall, the distribution of the structures we map and from the field survey is nearly linear distribution (Figure 5.4). Almost all of them are within the Hualien River, which indicates the fault trace of the Lingding Fault is along the river. The confidence of our mapping results is systemically decreased from north to south, where the linear feature we map in the northern sandbar has the highest confidence. As all of these mapped features are roughly aligned and match the location of the deformed Hualien Bridge, we later use these locations as the surface trace of the Lingding Fault to estimate the displacement across the fault (Figure 4.7).

doi:10.6342/NTU202202354

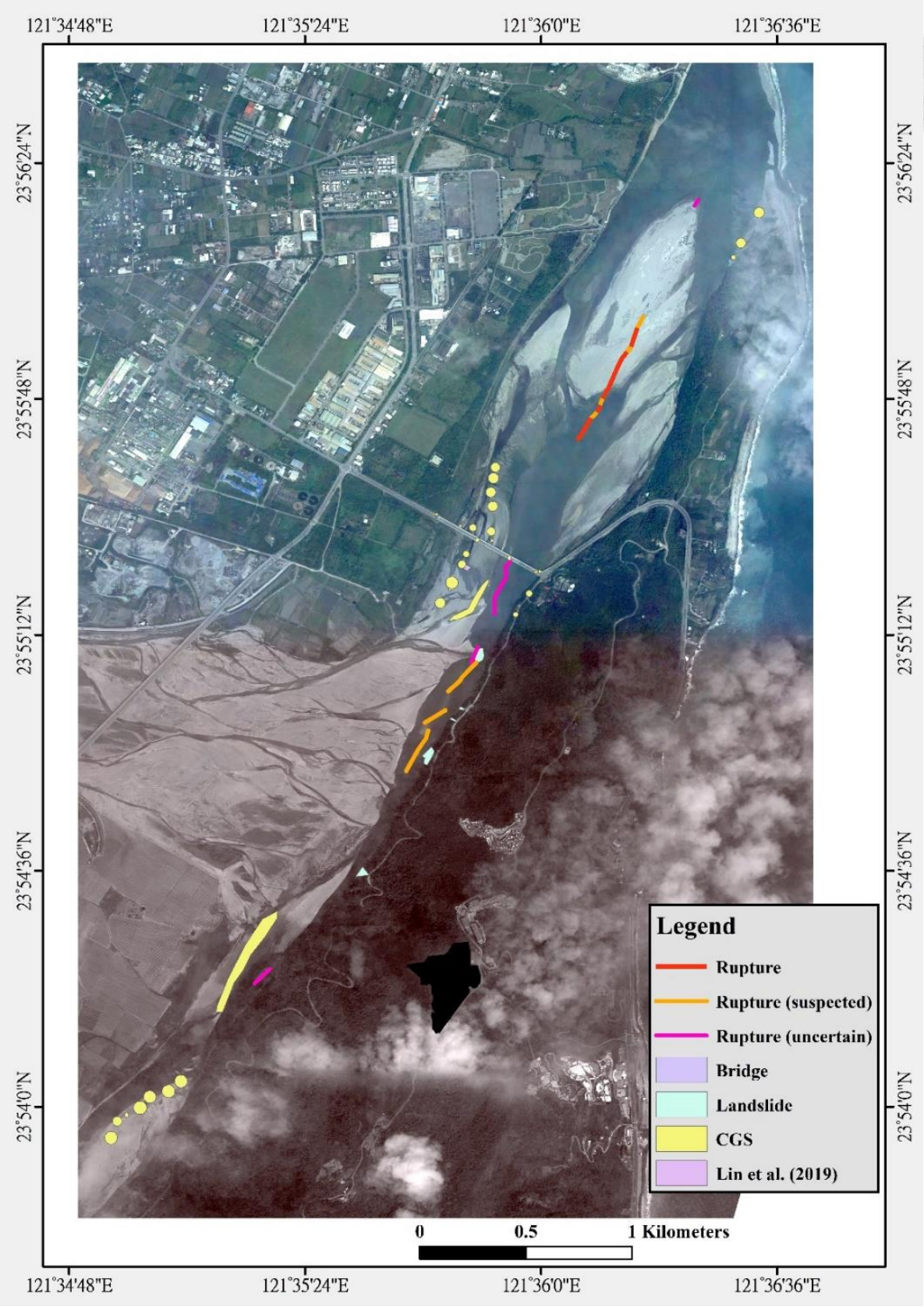

Figure 5.4 The overall mapping result of earthquake-related structures, and the field survey results by CGS and the previous study are also included.

doi:10.6342/NTU202202354

5.3 Sub-pixel correlation

After locating the Lingding Fault ruptures from aerial photo inspection, we perform the sub-pixel correlation using the down-sampled orthorectified aerial photos. We test three different window sizes for sub-pixel correlation, including 32x32, 64x64, and 128x128 (Figure 5.5). Although our sub-pixel correlation results do contain some degrees of topographic effects in the urban area and the Coastal Range, the deformation pattern of these three window sizes can still be noticed, with the western part (the Longitudinal Valley) moving southwestward and the eastern part (the Coastal Range) moves northeastward. This pattern agrees with previous study results that the Lingding Fault is likely to be a left-lateral strike-slip fault (陳等人，2008). From the surface offset map, the offset is N/S component dominant, owing to the fault's strike being nearly N-S direction. The northern part of the Lingding Fault also has larger deformation than the southern part of the fault. Interestingly, the rupture on the sandbar near the Hualien River mouth can be clearly identified in the offset maps, especially in larger window sizes. Comparing the results of these three window sizes, the smaller window size produces much higher frequency signals, both in the offset maps (Figure 5.5) and the profiles (Supplementary 7 and 8). However, the first-order pattern and the values of these three are quite similar.

doi:10.6342/NTU202202354

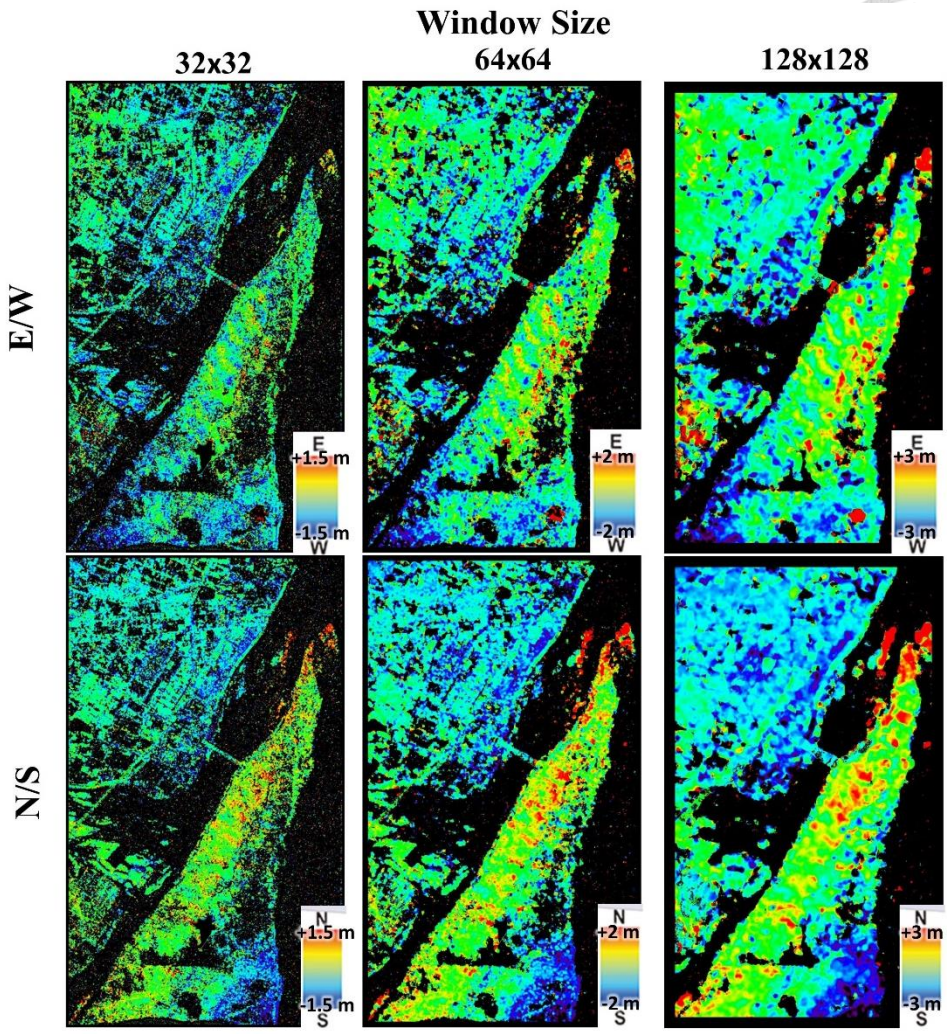

Figure 5.5 The offset maps of three window sizes. The upper column is the E/W component, and the lower column is the N/S component.

The topographic effect could result from the edge of high buildings and mountain ridges, where obtaining good orthorectification results is difficult from the standard aerial photos. Because higher objects will have larger differences in images from different looking angles, the sub-pixel correlation results show some outlines of the buildings. In addition, the southern part of the Coastal Range also shows some weird movement directions, especially for the southeastern part of the image. This error could

doi:10.6342/NTU202202354

be related to its marginal location and the cloud coverage in the post-quake images, where the orthorectification results are also poor at this corner, owing to the fewer images covered in this area.

The displacements across the Lingding Fault from three different window sizes are calculated through 13 profiles across its surface fault trace (Figure 5.6). The N/S component shows that the surface displacement decreases southward, from >1.1 m in the north to ~0.5 m in the south. The pattern for the E/W component is not very clear, but its general trend suggests the displacement increases slightly from the northern part and retains in ~0.2 - 0.4 m to the south.

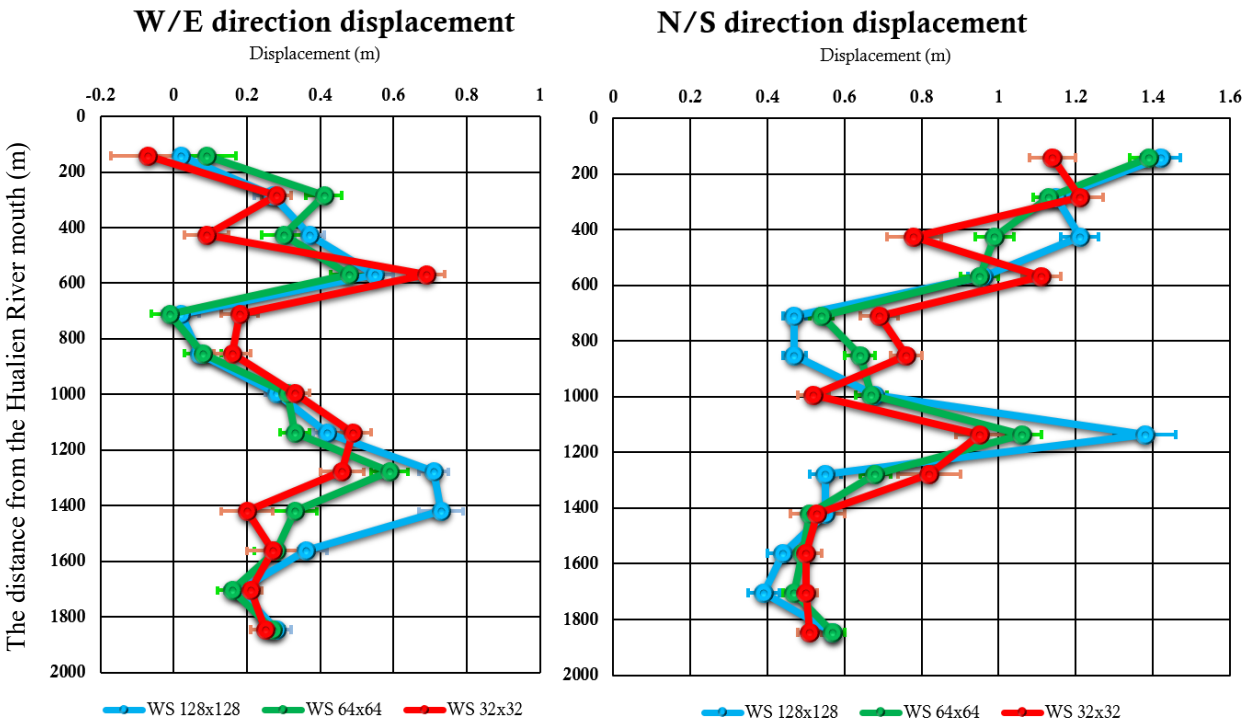

Figure 5.6 The displacement across the fault of 13 profiles. The left is the W/E component of the displacement, and the right is the N/S component.

doi:10.6342/NTU202202354

We also calculate the fault-parallel and the fault-perpendicular components of the displacement with the fault strike N29°E, which can more intuitively understand the spatial change of the motion for a strike-slip fault (Figure 5.7). The result shows that the displacement of the Lingding Fault in the 2018 Hualien earthquake is fault-parallel component dominant, with the values constantly larger than 0.5 m through the entire section of Lingding Fault we study. The fault-perpendicular component is also slightly larger at the northernmost part of the fault, around 0.5 m with compressional motion. The rest of our profiles show the value of 0.2 m, with motion shifting from the compression to the extension from north to south. The change of fault-perpendicular motion suggests only limited dip-slip motions occurred along the Lingding Fault during the 2018 Hualien earthquake.

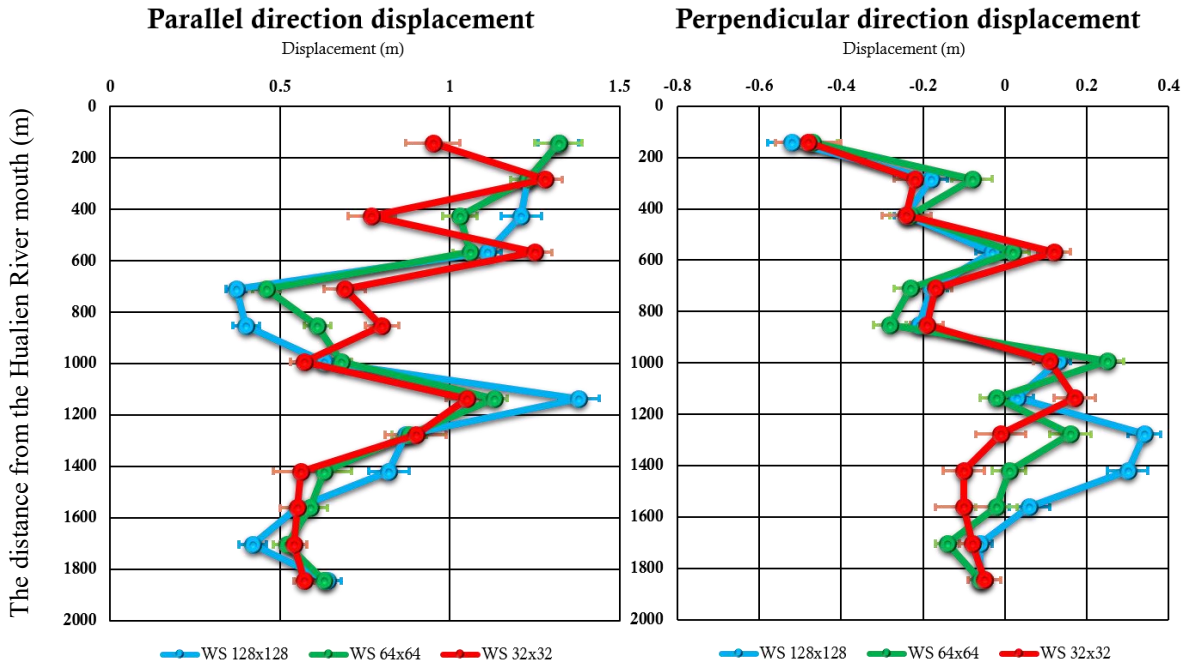

Figure 5.7 The displacement across the fault of 13 profiles. The left is the parallel to the fault component of the displacement (+: left-lateral motion, -: right-lateral motion), and the right is the perpendicular to the fault component (+: extensional motion, -: compressional motion).

doi:10.6342/NTU202202354

5.4 Elastic half-space dislocation model

The Okada half-space elastic dislocation model is used to inverse the surface deformation to understand the fault slip at depth. The input data includes the surface deformation calculated from the COSI-Corr, along with 20 RTK GNSS data (Wu et al., 2019) and 2 GPS data (CGS, 2018). The surface deformation data from COSI-Corr using correlation window size 64x64 (the reason will mention in chapter 6.2) are down-sampled with window size 60 and step 60 (Figure 5.8) to reduce the number of points in the inversion model. We first use the checkboard test to find the optimal depth, which our data can resolve. Three different checkboard sizes are tested (Figure 5.9) and show our data can only resolve the fault slip shallower than 8 km deep.

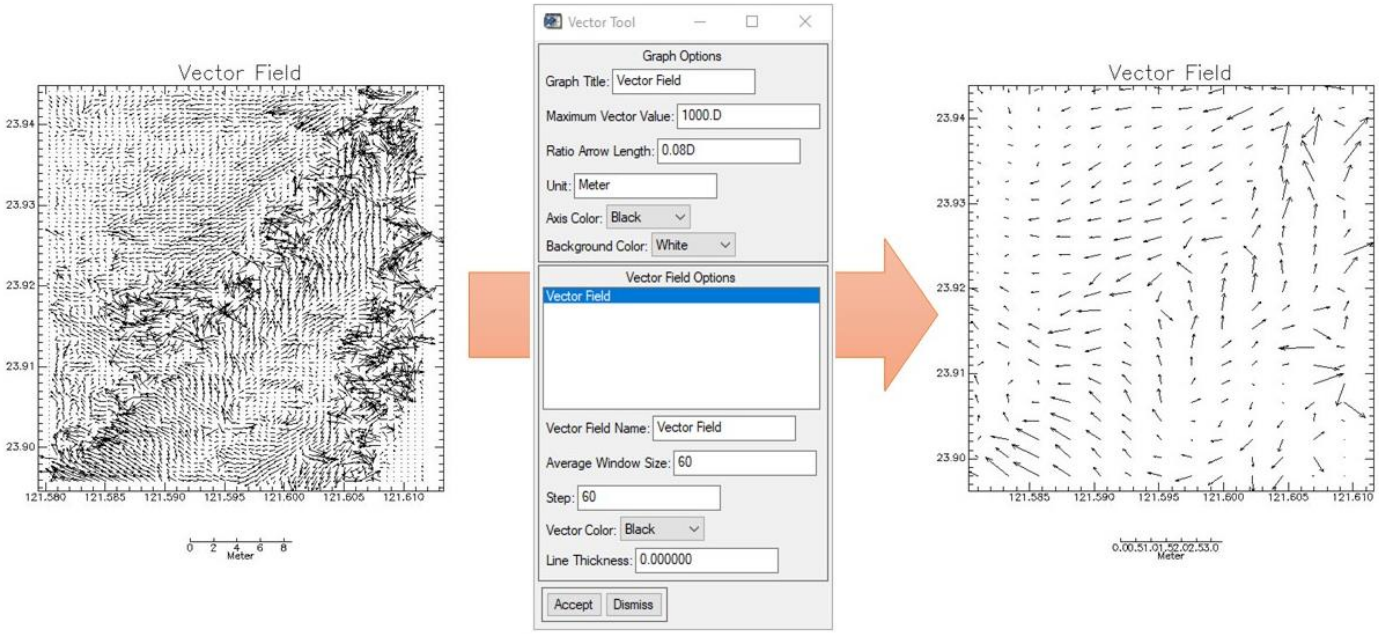

Figure 5.8 The down-sampling process for the surface deformation data. We use average window size of 60, and step of 60.

doi:10.6342/NTU202202354

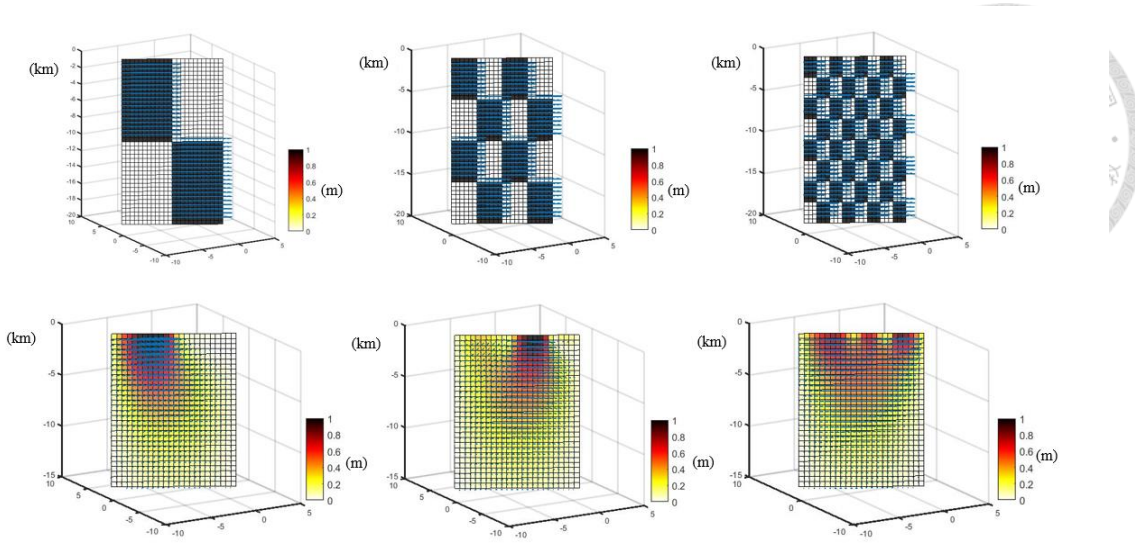

Figure 5.9 The checkboard tests with three different sizes. The test data include the surface deformation from COSI-Corr, RTK GNSS, and GPS. The upper column is the input checkboard setting, and the lower column is the output result.

Following the checkboard test, we test the optimal fault length and fault dip from the inversion model. Because the modeled length of the fault can affect the value and position of fault slips, and the fault should not be limited by the boundary of land and ocean, we test 5 different fault lengths (6 km, 8 km, 10 km, 12 km and 14 km) (Figure 5.10a) to discuss in what situation the fault length will not significantly influence the fault slip result. Among our 5 test results, the smallest modeled fault length, 6 km, fits the input data spatial range, showing smaller largest-slip than other results. From the average residual (absolute value) and the fault length relationship (Figure 5.10b), the longer fault length has a smaller residual, owing to the fault slips on the small patches can have more combinations. The residuals of 12 km and 14 km don't have a large change. Therefore, we choose the fault length of 12 km for the following calculation.

doi:10.6342/NTU202202354

Because we don't have better constrain for the fault length extension in the ocean. Then, the different fault dips are tested to find the optimal fault geometry (Figure 5.11). We test the fault dips ranging from 55° (east-dipping) to 75° (west-dipping), with a 5° interval, as previous seismicity studies suggest the fault plane likely to be a 50° east-dipping plane (Kuochen et al., 2004) or a high-angle (75°) within the top 30 km deep (陳等人，2018). The result shows that the high-angle fault plane better fits our ground deformation data. The reason for the different fault dip angle results is mostly related to the research method applied to these studies. The result from seismicity distribution can reveal the major tectonic structures, but it is hard to discuss the detailed minor structures, such as the very shallow part of the Lingding fault. Hence, for the fault geometry, we will use 5 km for the fault bottom depth, 12 km for the fault length, and 90° for the fault dip angle.

doi:10.6342/NTU202202354

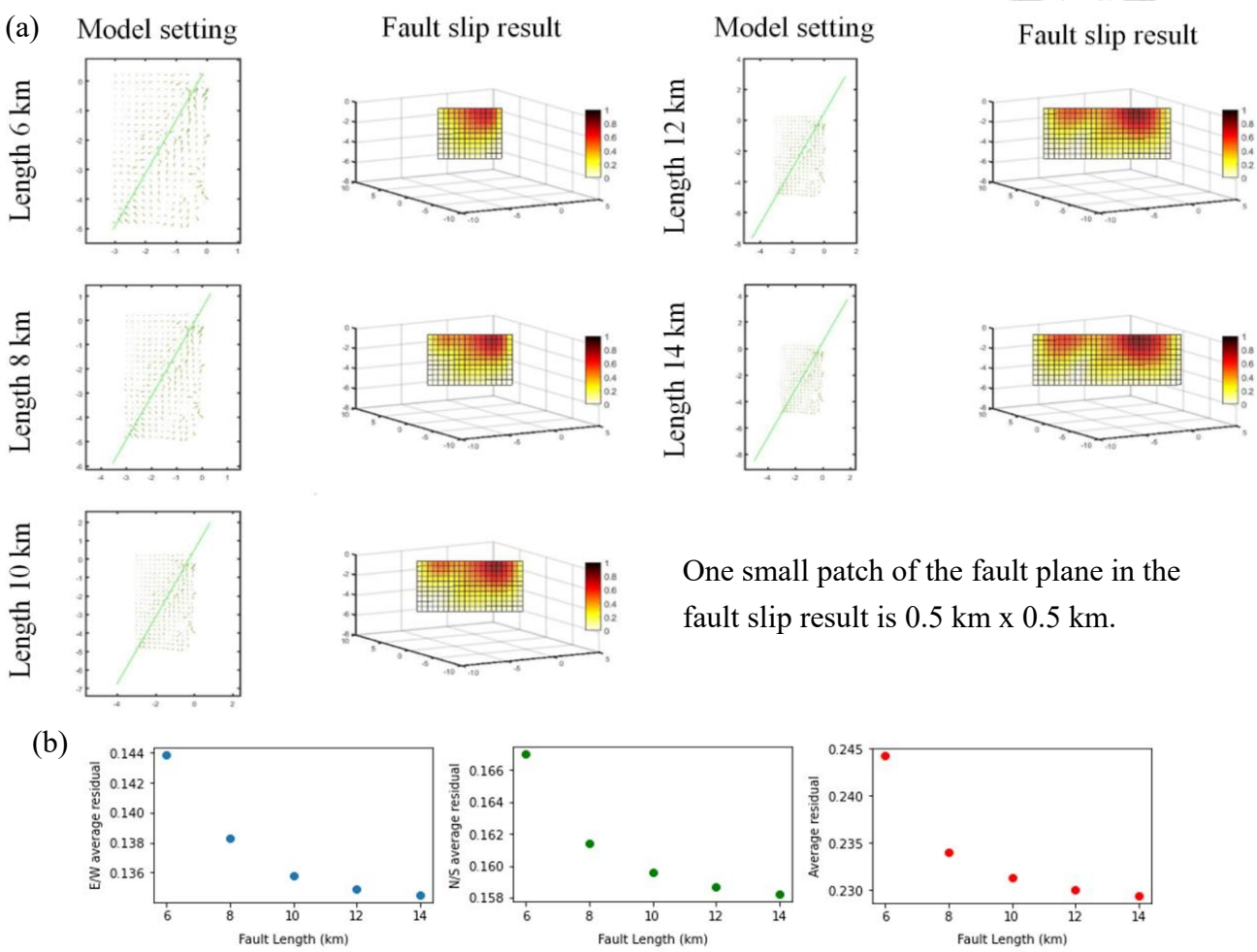

Figure 5.10 (a) The input model setting with different fault lengths (the arrows are the data points of surface deformation and the green line is fault location) and output fault slip results. (b) The average residual (E/W component, N/S component, and combination of two directions) for different fault lengths.

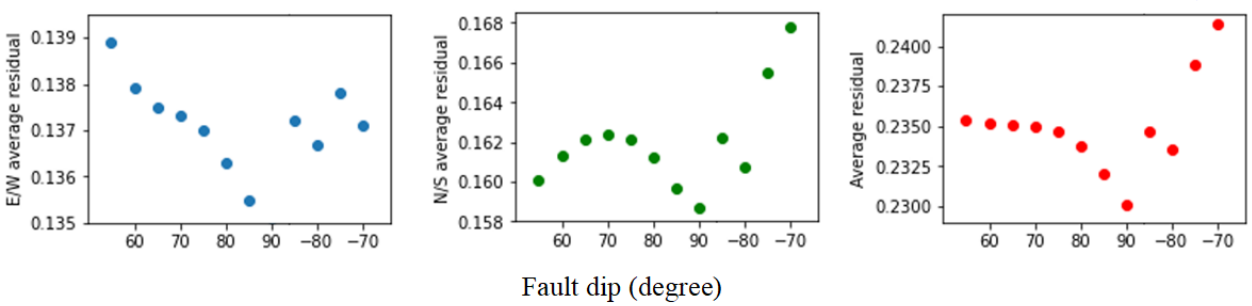

Figure 5.11 The average residual for different fault dips (degree). The positive degree means the fault plane dips to the east, and the minus one means west-dipping plane.

doi:10.6342/NTU202202354

The inversion result of our elastic half-space dislocation model shows the fault slip concentrates at very shallow depth (Figure 5.12), from near the surface to around 4 km deep. The slips on the fault plane are all within 1 m. The larger fault slip locates in the northernmost of the fault. From the result with vectors, the northern part of the movement is with a downward motion, which qualitatively agrees with leveling and GPS results (CGS, 2018). The overall vectors show the Lingding Fault has a left-lateral strike-slip motion during the 2018 earthquake. However, the southwestern end has right-lateral strike slips. We think this dextral slip is an artifact since our input data do not cover this part of the fault. We also compare the surface deformation we input for calculation (Figure 5.13 upper column) and the surface deformation calculated from inversed fault slip model (Figure 5.13 middle column). The average residual (Figure 5.13 lower column) for the E/W component is 0.13 m, and ~0.16 m for the N/S direction.

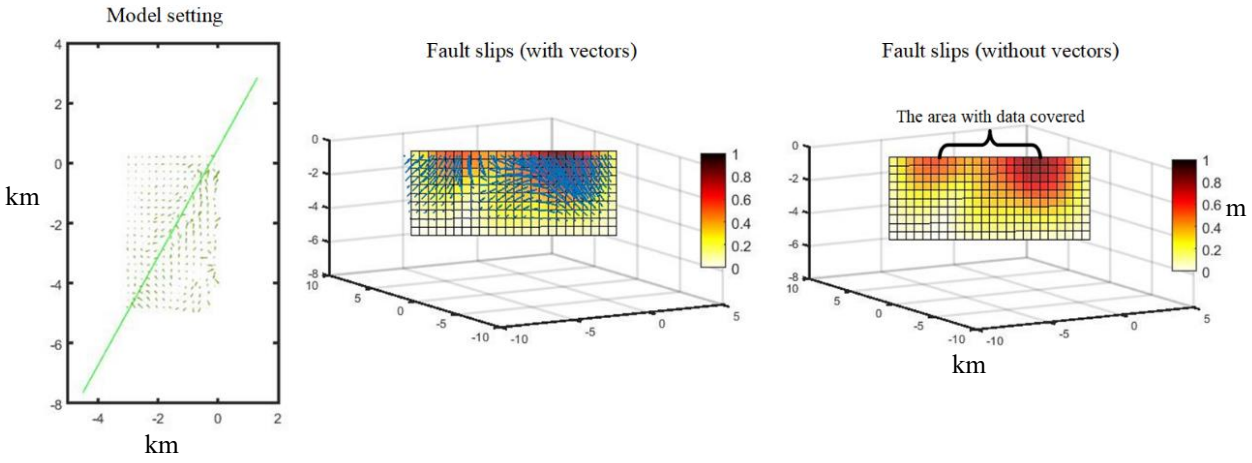

Figure 5.12 The input model setting (arrows: input surface deformation data, green line: fault location) and the inversion result of fault slips.

doi:10.6342/NTU202202354

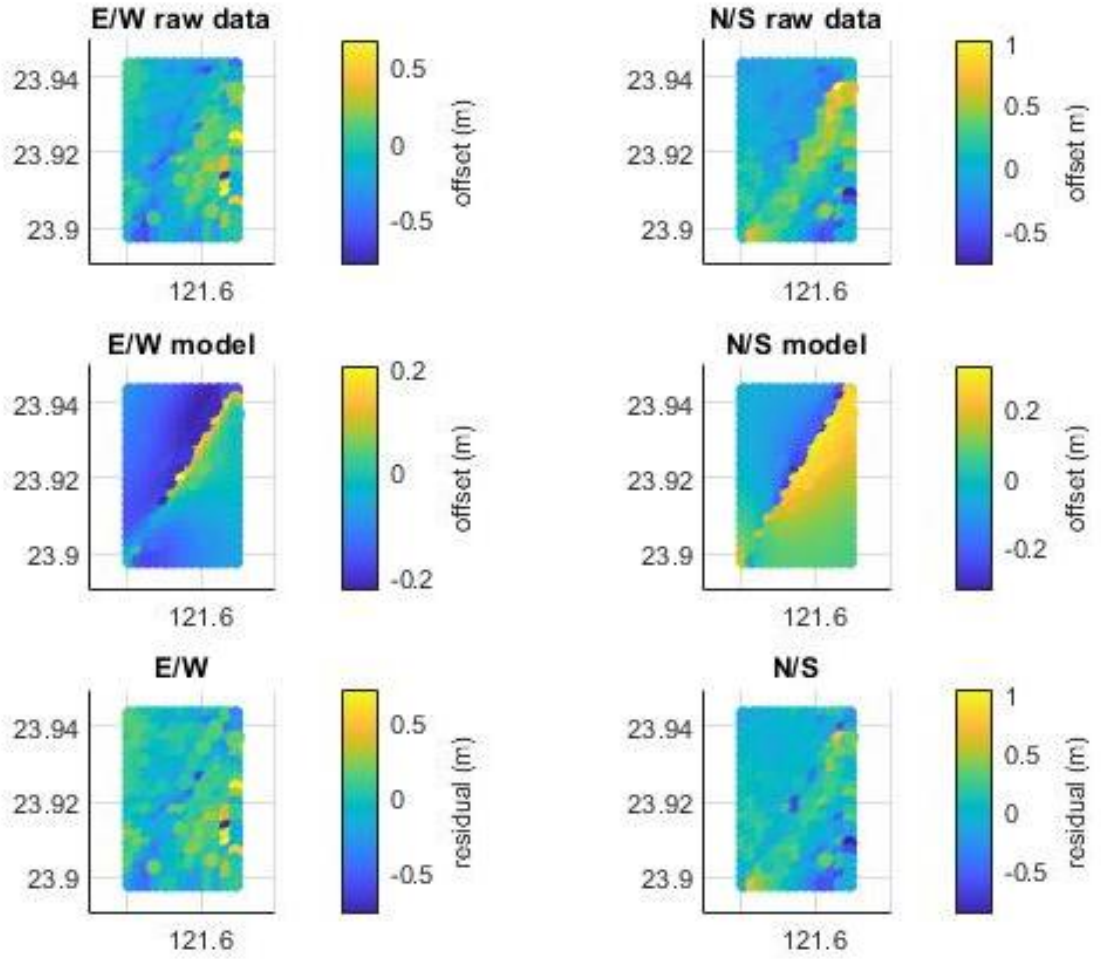

Figure 5.13 The surface deformations for input data (upper column) and fault slip model (middle column). The bottom column is the average residual.

doi:10.6342/NTU202202354

6. Discussion

6.1 Internal validation of the ground displacement results

We conduct a series of tests to validate our result of ground displacement, and to check if different methods or materials quality (i.e., the orthorectification methods and procedures; the material for sub-pixel correlation) could cause a large discrepancy in our results. On the following page, we discuss each of our testing results in detail.

6.1.1 The different methods for aerial photo orthorectification

In order to validate whether the method for orthorectified aerial photos or the distribution of GCPs can significantly change the surface deformation result, we use different sets of GCPs from only one side of the fault, and generate the offset maps from these single-side GCPs orthorectified aerial photos (see chapter 4.2 for more details). The result of offset maps is generally similar to different sets of GCPs (Supplementary 9). For a more detailed comparison, 13 profiles across the Lingding Fault are plotted, showing that these results are almost the same across the fault (Figure 6.1), no matter which window sizes are applied to the sub-pixel correlations. The N/S component displacement, in particular, is not affected by the selection of GCPs. The E/W component displacement at the eastern part of the fault from both sets of GCP selection is slightly larger than the original method. This could be caused by the topographic

doi:10.6342/NTU202202354

effect, the clouds coverage or the loose orientation controls of the photo across the track. Although there are some differences in the E/W component, the displacement of the Lingding Fault in this earthquake is N/S component dominant. Therefore we think this would not affect the result greatly. Further comparisons with RTK GNSS and GPS data are also made to check the quality of different methods (Supplementary 10). The original method still shows a better result, because the result is more similar to the other observation (see chapter 6.2). Besides, the aerial photos include two flight tracks; therefore, having ground control points on both sides of the fault is still important to obtain good quality sub-pixel correlation results.

doi:10.6342/NTU202202354

Window Size 32x32

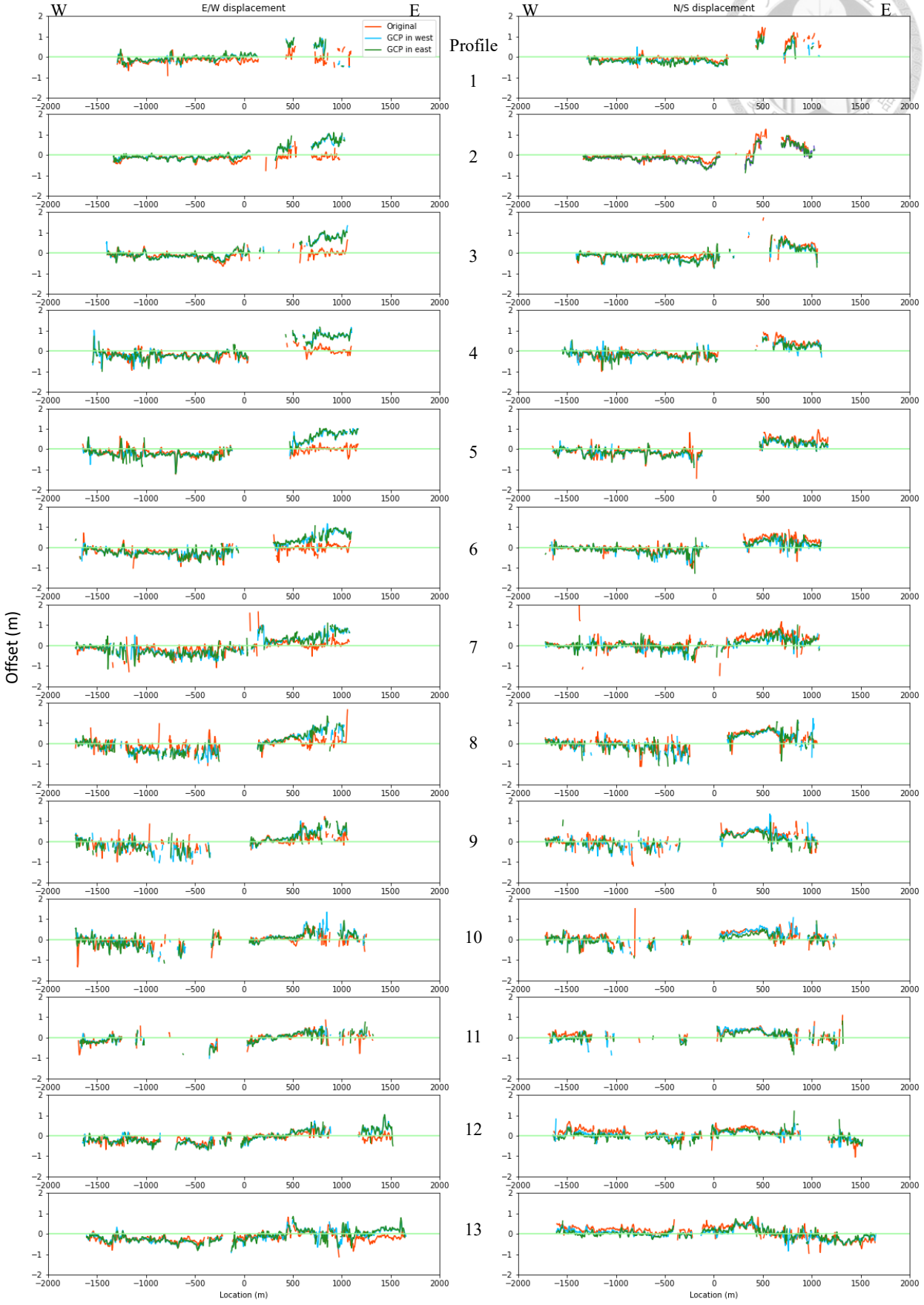

doi:10.6342/NTU202202354

Window Size 64x64

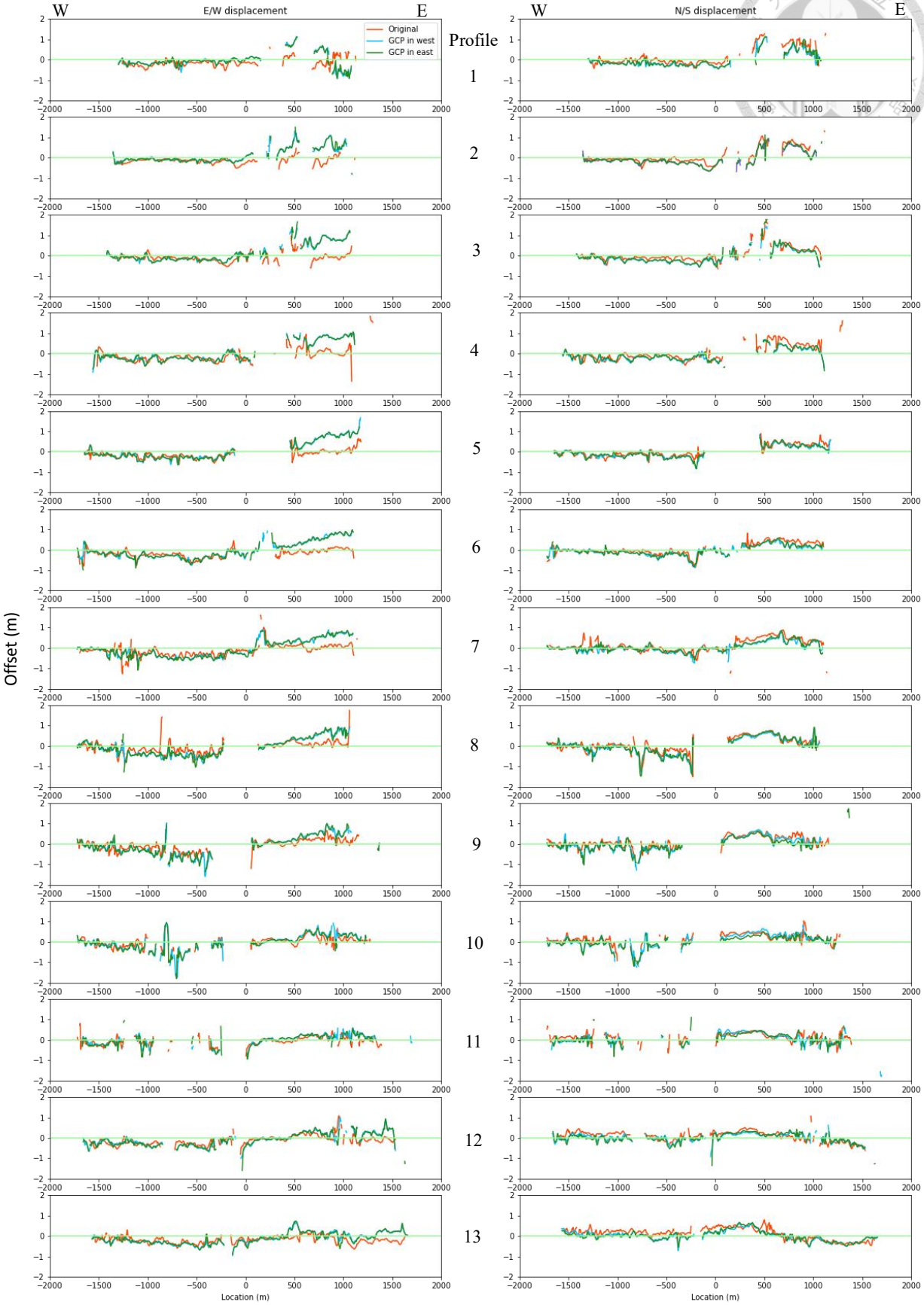

doi:10.6342/NTU202202354

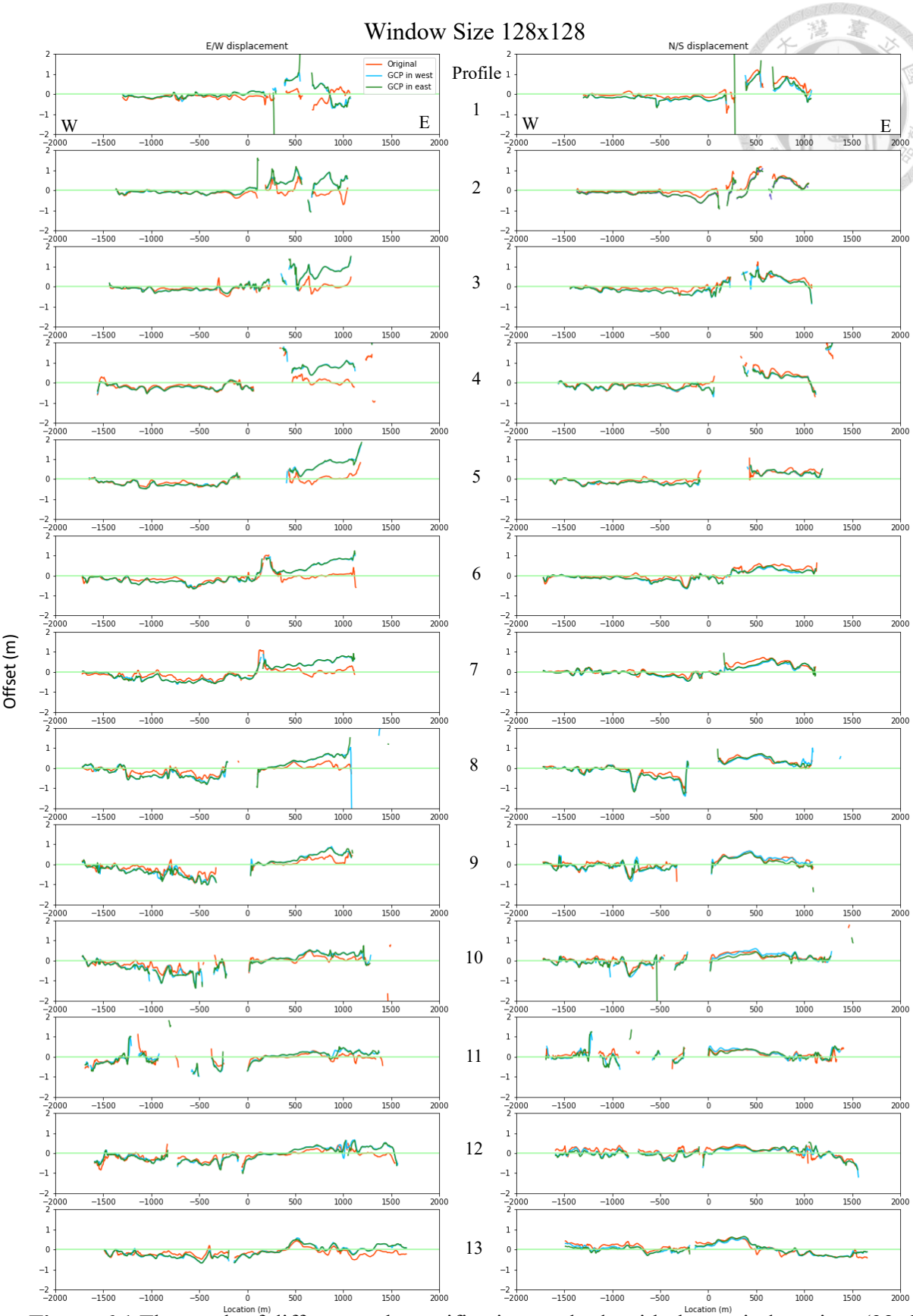

Figure 6.1 The result of different orthorectification methods with three window sizes (32x32, 64x64, and 128x128). The orange line is the original method we used for orthorectification. The blue and green lines are the control points only turned on in the western and eastern part, respectively.

doi:10.6342/NTU202202354

6.1.2 Comparison of the result from aerial photos with the result from satellite images

Because our post-quake aerial photos are suffered by the clouds covering the Coastal Range side, the result of the sub-pixel correlation could be affected. Therefore, we use the SPOT 7 satellite images to validate the result from the aerial photos. Unfortunately, the orthorectification process of the SPOT 7 images was already done by the National Central University, thus we are not able to use the same set of GCPs to process these satellite images. Compared to the aerial photos used in this study, the resolution of the SPOT 7 satellite images is lower, but they are not covered by any cloud and the image taken dates are closer to the 2018 earthquake. Although the signal from these satellite images is quite noisy, the general pattern is similar to that obtained from the aerial photos (Figure 6.2). The displacement in the eastern part of the E/W component is also similar, which has some differences in comparing different methods of orthorectification (chapter 6.1.1). The noisy surface displacement signal obtained from the satellite images can be attributed to the purpose of the orthorectification for satellite images, since the automatic orthorectification method may not be suitable for high precision usage, such as moderate earthquake surface deformation.

doi:10.6342/NTU202202354

Window Size 32x32

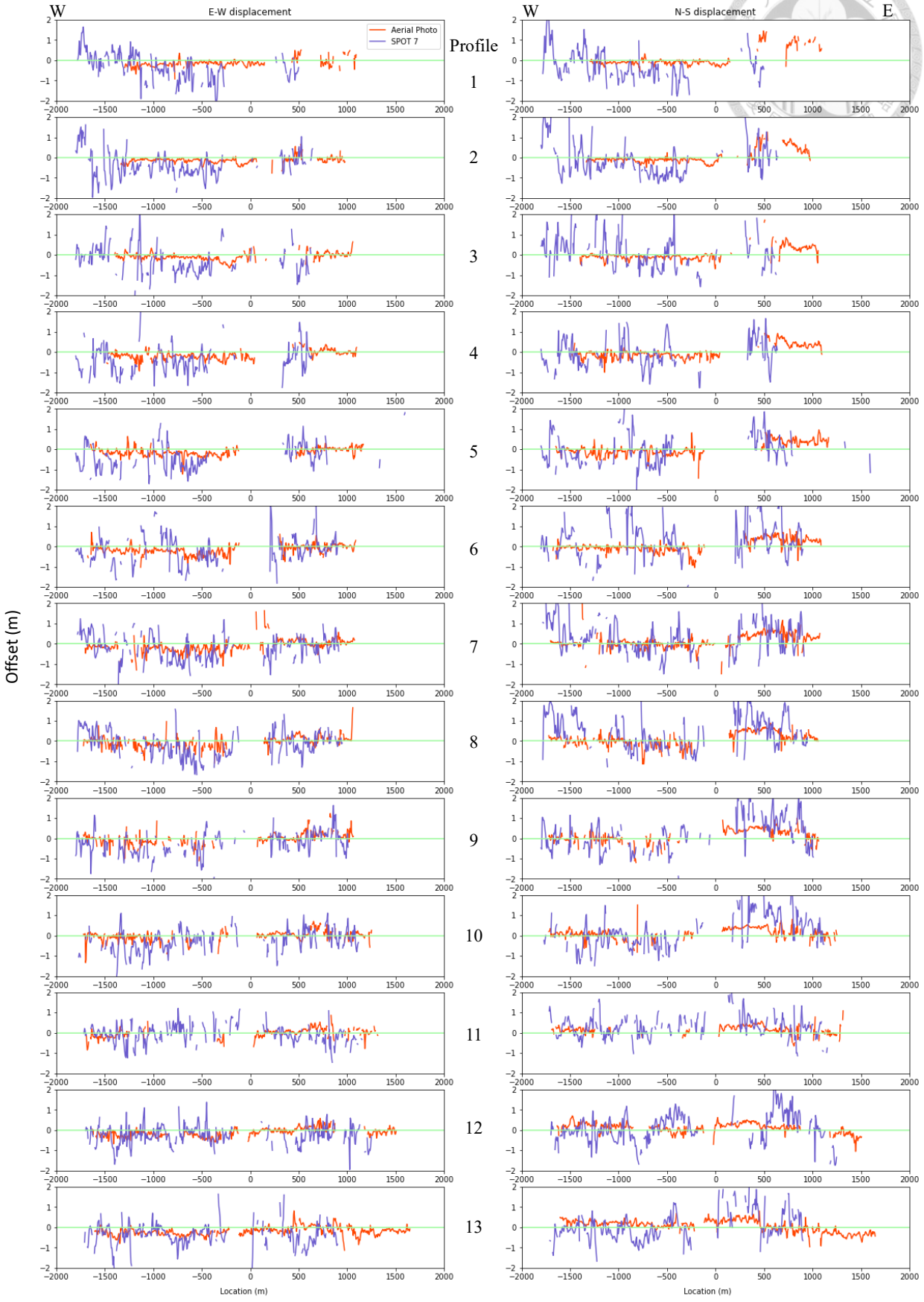

doi:10.6342/NTU202202354

Window Size 64x64

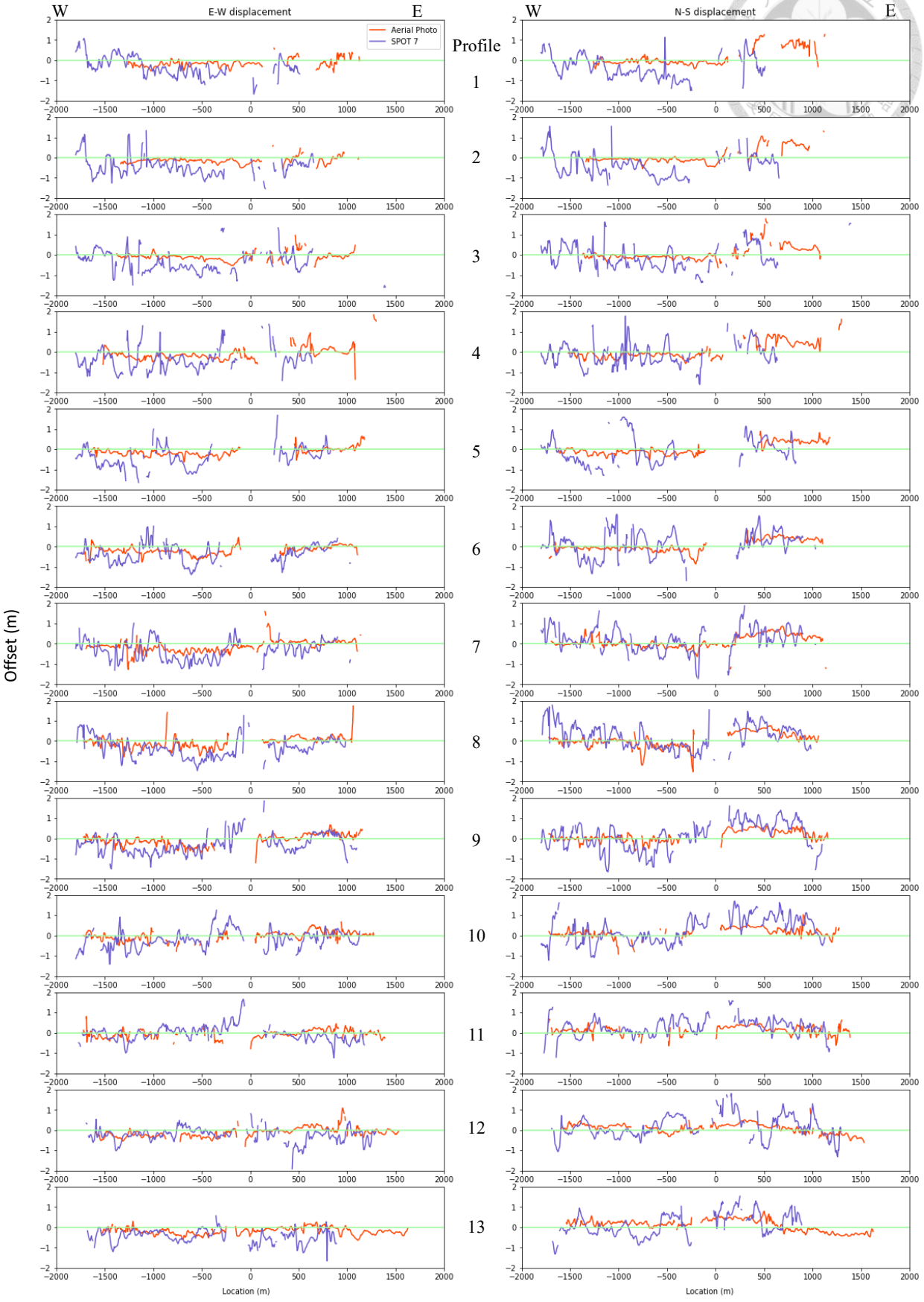

doi:10.6342/NTU202202354

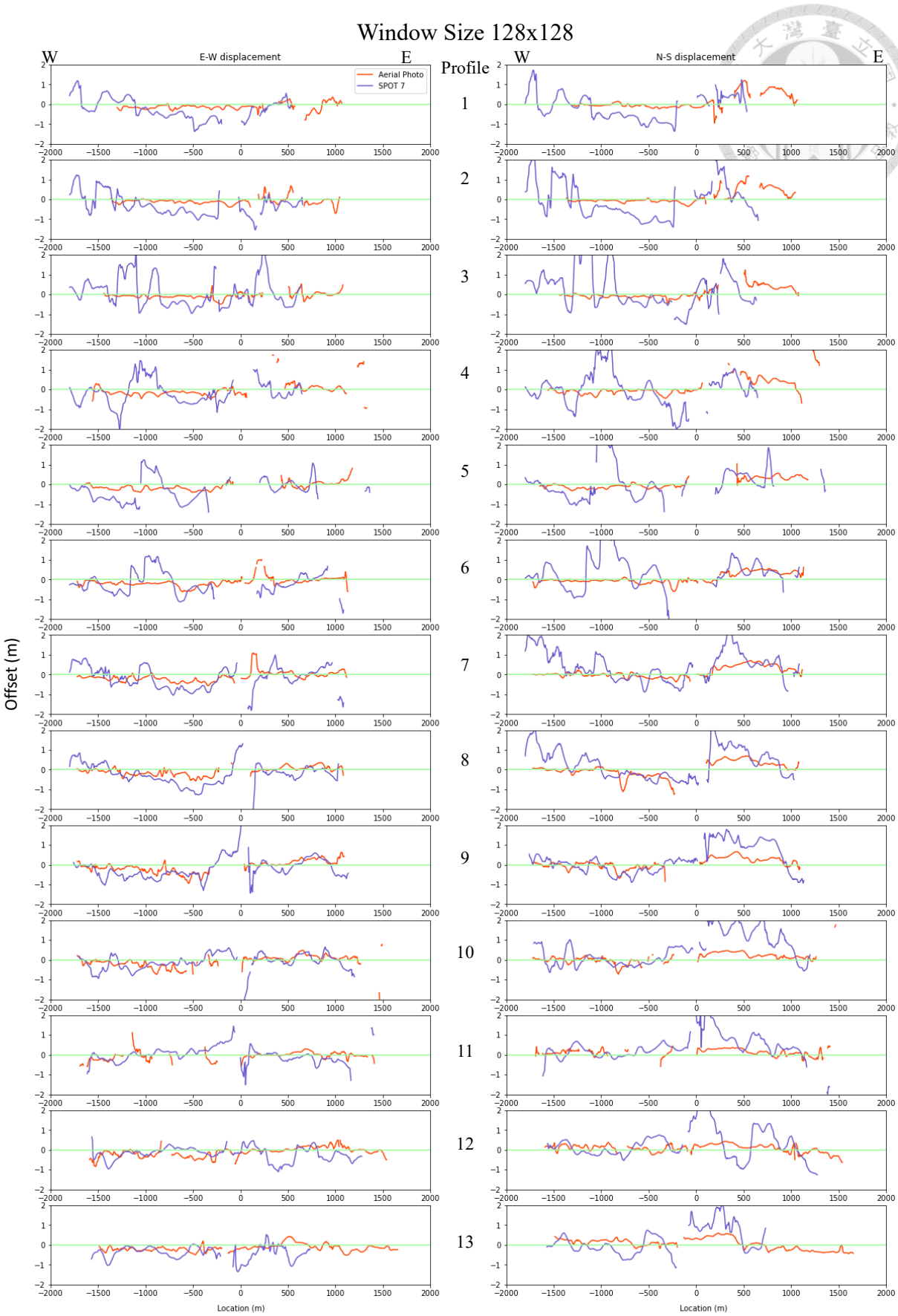

Figure 6.2 The result of COSI-Corr using different materials with three window sizes (32x32, 64x64, and 128x128). The red line is the result of aerial photos, and the blue line is the result of SPOT 7 images.

doi:10.6342/NTU202202354

After comparing the different materials and methods we use, we believe our result is overall reliable. The different methods for orthorectification show almost the same results, with only slightly different in the eastern part of the E/W component. However, this difference does not appear when comparing satellite image results. Although the signals of satellite images are noisy, the first-order comparison is still similar. Hence, the internal validation of our result is acceptable.

6.2 External validation for the displacement result

To have higher reliability of our results, we not only do the internal validation, which is mainly related to the materials and processes we use, but also the external validation, in which we compare our result with the published data, including the measurement from the field survey and GNSS result.

6.2.1 Comparison with the field survey

As we mentioned before, the only displacement along the Lingding Fault reported after the 2018 Hualien Earthquake is on the Hualien Bridge. The displacement is around 70 cm (CGS, 2018; Lin et al., 2019). One of our profiles, Profile 7, covers the area of the Hualien Bridge. Therefore, we compare the parallel component of the displacement across the fault with the field survey result. Our result shows the parallel component of displacement for Profile 7 is 0.57, 0.68, and 0.63 meters, from window size 32x32 to

doi:10.6342/NTU202202354

128x128 (Figure 6.3). The results for the three window sizes are all within 20% relative error, which indicates our result has high reliability.

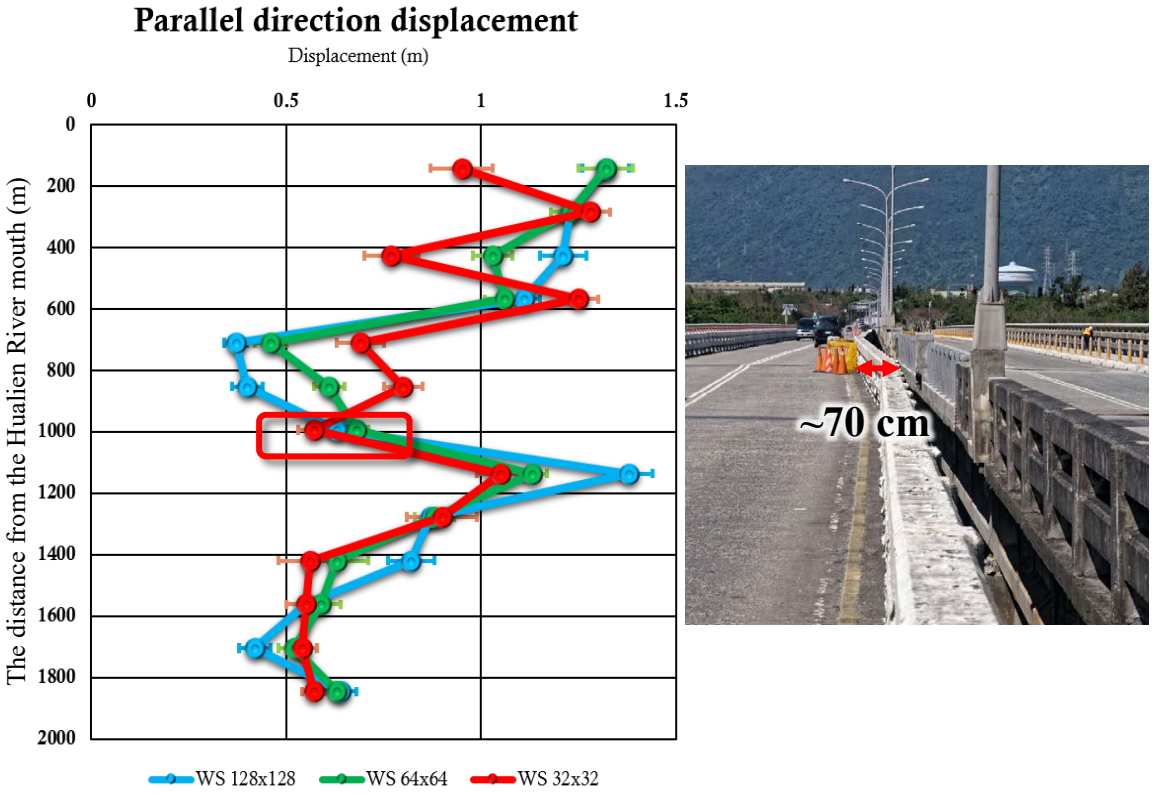

Figure 6.3 Left is the parallel component of displacement across the fault. Profile 7, the red rectangle, covers the Hualien Bridge. Right is the photo of the deformed Hualien Bridge (modified from CGS, 2018). The displacement for three window sizes is similar to the field measurement, ~70 cm.

6.2.2 Comparison with GNSS data

Because there is only one displacement of the Lingding Fault measured after the earthquake, the quality of the rest of the surface deformation result is still unclear. Hence, we compare the surface deformation with published GNSS data (CGS, 2018;

doi:10.6342/NTU202202354

Wu et al., 2019). The GNSS data include 20 RTK GNSS displacement data, and 2 GPS geodetic station data. To lower the topographic effect and noise influence, we average our sub-pixel correlation results with window size 40 and step 40 by software (Figure 5.6). The result (Figure 6.4) shows the N/S component is nearly 1:1 scale (slope: 0.86), especially excluding some outliers. The result for the E/W component is not as good as the N/S component, with a systemic shift of about 0.15 m. However, the slope is still nearly 1:1 scale (slope: 1.04). The deviations (COSI-Corr - GNSS) of both components are close to the normal distribution, with slightly shifting to negative. Even though the validation of the E/W component is not as good as we expected, our result still shows overall high reliability, because the surface deformation is N/S component dominated. The spatial distribution of the deviation for both components (Figure 6.4b) doesn't have an obvious systematic error. The larger deviation can be found in the near fringe area, the northern tip and the southern part of the Coastal Range for examples, where the orthorectification could not have a better result. We compare not only the window size 64x64, but also the window sizes 32x32 and 128x128 (Supplementary 11, 12). The result of window size 64x64 is better than the other two. Based on the comparison with GNSS data from the aspects of the linear regression, the general statistics on deviation values, and the spatial distribution of deviation, we think our surface deformation result is trustworthy.

doi:10.6342/NTU202202354

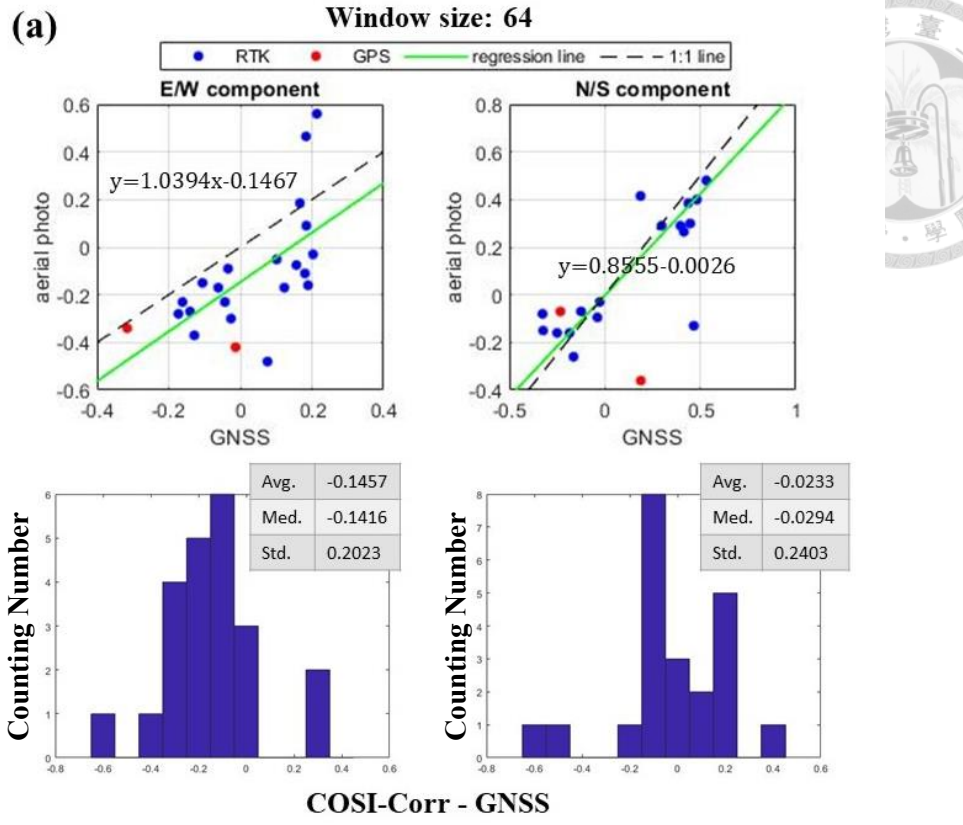

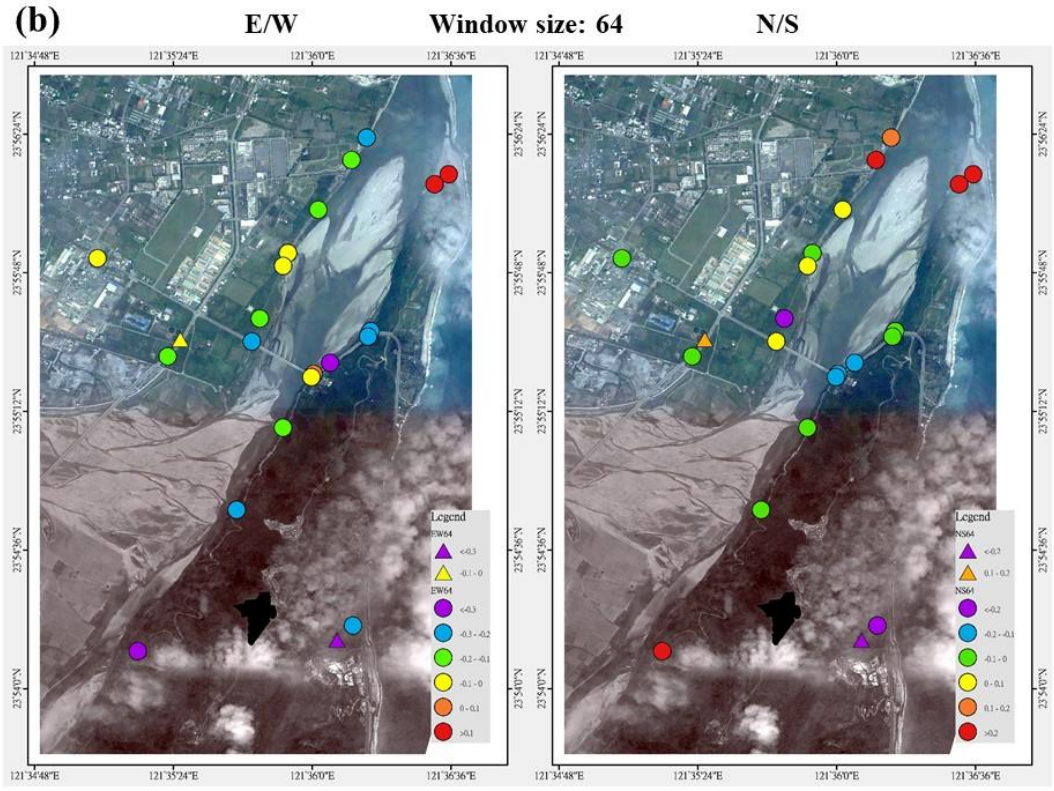

Figure 6.4 (a) The comparison of GNSS and the result of COSI-Corr (window size 64x64), and the lower column is the distribution of the deviation between the result of COSI-Corr and GNSS. (b) The spatial distribution of the deviation between the result of COSI-Corr and GNSS, with E/W component and N/S component.

doi:10.6342/NTU202202354

The external comparisons also indicate our result is reliable, especially for comparing the field survey. Although the comparison with GNSS has some shift for the E/W component, the slopes of the two components are almost 1:1 scale. The spatial and statistic distributions of the deviation (COSI-Corr - GNSS) indicate our result contains an uncertainty of around 20 cm, which is larger than the calculation uncertainty for the fault offset estimations. From these two external validations, the window size 64x64 also shows better results. Therefore, we use the result of window size 64x64 to calculate the fault slip (chapter 5.4).

The vertical component of the fault offsets are calculated from our fault slip model, and are compared with the geodetic survey results, including the leveling data and GPS station records from Central Geological Survey (CGS, 2018). The model result and the GNSS observation are similar in the first order, with the same movement direction. However, the quantitative comparison has some differences, as our modeling result does not maintain a good linear trend and some even have larger discrepancies compared to the field survey result (Figure 6.5). The reasons for the differences include that we only input the horizontal components of offsets. Hence, the vertical component has no constraint. Because there are only five locations for comparison, the overall difference between the model and the real world is still unclear.

doi:10.6342/NTU202202354

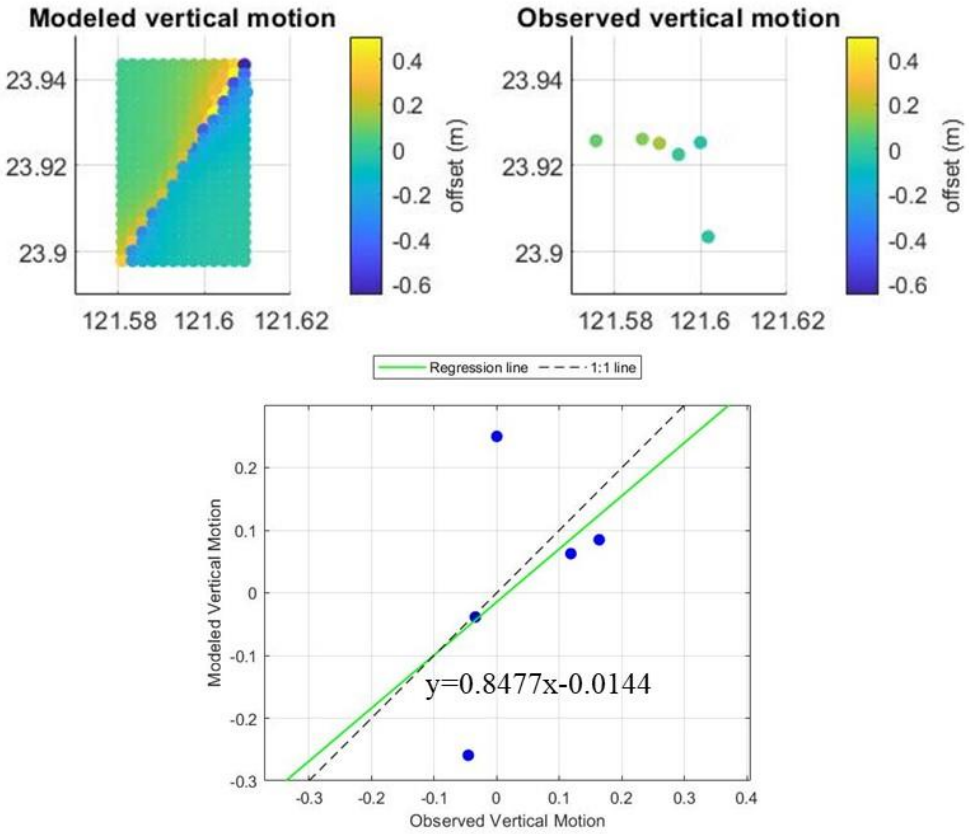

Figure 6.5 The vertical component of offsets comparison between the model result and GPS and leveling observations (CGS, 2018).

6.3 The shallow fault slip

6.3.1 The effect of the sub-pixel correlation result

To examine the importance of the sub-pixel correlation result, we not only calculate the fault slip from the sub-pixel correlation and GNSS (RTK and GPS) (Figure 6.6a), but also solely use the GNSS data to do the inversion (Figure 6.6b). Both results yield a similar shallow fault slip pattern, with larger slips in the northern part of the

doi:10.6342/NTU202202354

fault and focusing on the shallow depth. Nevertheless, the detailed pattern and values have some differences. The vectors show the movement with some downward motions in the northern part with the calculation of the sub-pixel correlation result, but the result from GNSS-only inversion reveals an almost purely left-lateral strike-slip movement. The value of fault slips with the input of sub-pixel correlation is also larger than the slip from the GNSS-only data. These differences could be related to the spatial distribution and number of input data. As the model set is shown in figure 6.6, the GNSS data is mostly concentrated in the riversides of the Hualien River, which are very close to the fault. Therefore, the resolution of the fault slips should be at a very shallow depth. The small number of input data, 22 data points, also has less control for the inversion. Although there are some differences between the two input data sets, the general patterns are similar. Considering the sub-pixel correlation result, the fault slips will have more detailed results, owing to the spatial distribution and numbers of data.

doi:10.6342/NTU202202354

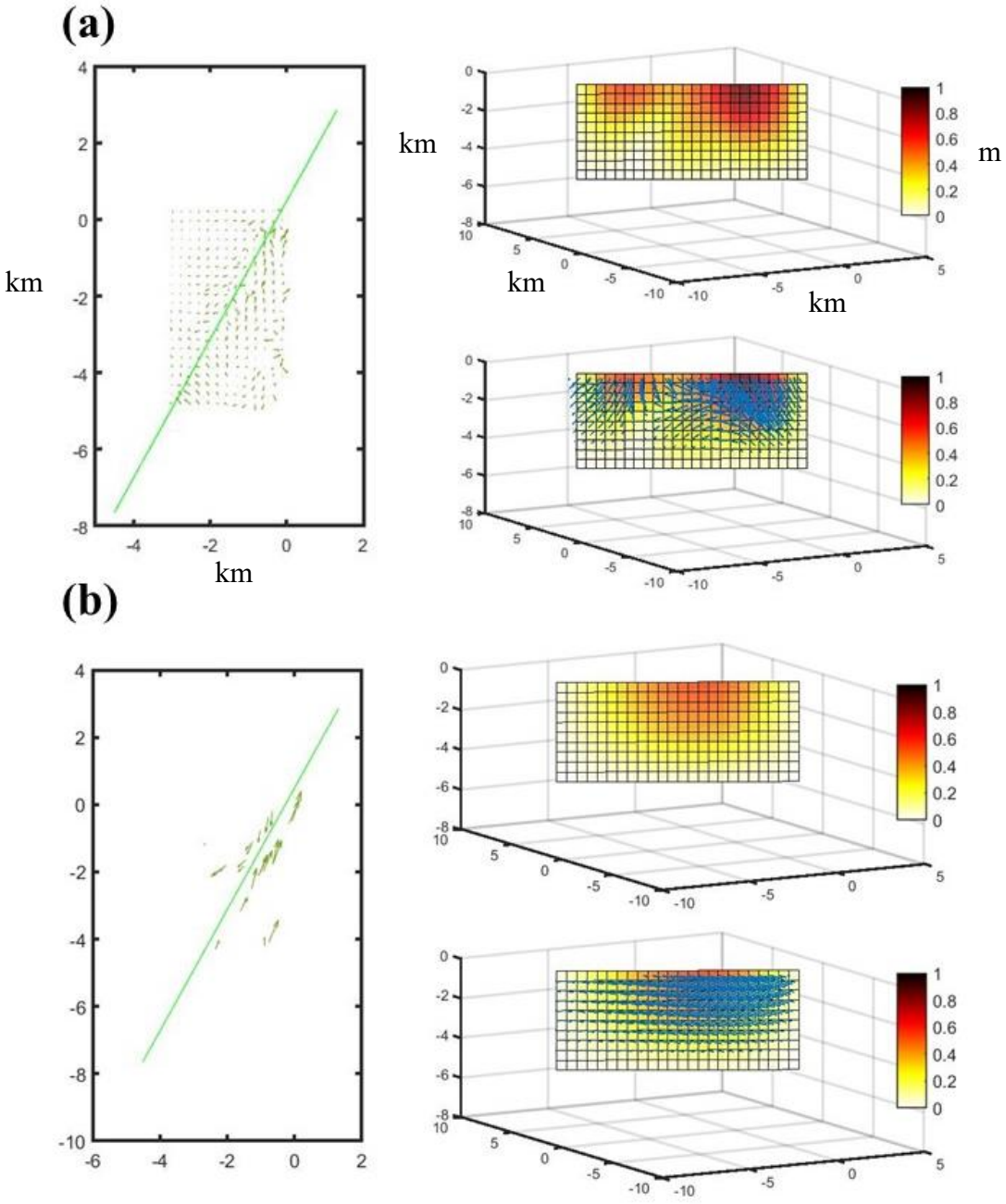

Figure 6.6 The inversion fault slip results. (a) The input data includes sub-pixel correlation result and GNSS. (b) The input data only used GNSS. Left is the model setting, and right is the fault slip results with and without vectors.

doi:10.6342/NTU202202354

6.3.2 Comparison of the fault slip with published studies

As we mentioned in Chapter 3, there are some studies used the InSAR, GPS, and/or seismic data to calculate the slip on the Lingding Fault plane (M. H. Huang & Huang, 2018; Lee et al., 2018; Lo et al., 2019; Yang et al., 2018; Zhao et al., 2020). However, most results are too smooth to discuss the detailed slip pattern. The only three studies that have better results are Lee et al. (2018), Zhao et al. (2020), and Lo et al. (2019) (Figure 6.7). Therefore, we only compare our fault slip result with theirs. The detailed fault geometry settings for these three are summarized in Table 6.1.

Table 6.1 The fault geometry model for inversion of previous studies.

Previous studies	**Data**	**Fault length (km)**	**Fault width (km)**	**Fault dip (°)**	**Maximum slip (m)**	**Fault number in inversion**	**Size of subfaults**
Lee et al., 2018	Teleseismic body waves, local ground motion, GPS	?	17	75 (east-dipping)	1.19	3	~ 10 km^2
Lo et al., 2019	Teleseismic body waves, regional strong motion, SAR, GPS	5-6*	~5*	~90	>2	3	~0.2 km^{2*}
Zhao et al., 2020	InSAR, GPS, broad-band teleseismic data	10	12	60 (east-dipping)	1.2	4	4 km^2

*Because Lo et al., 2019 only mentioned the number of subfaults, the length and width of the fault are measured based on the scale in their figure.

doi:10.6342/NTU202202354

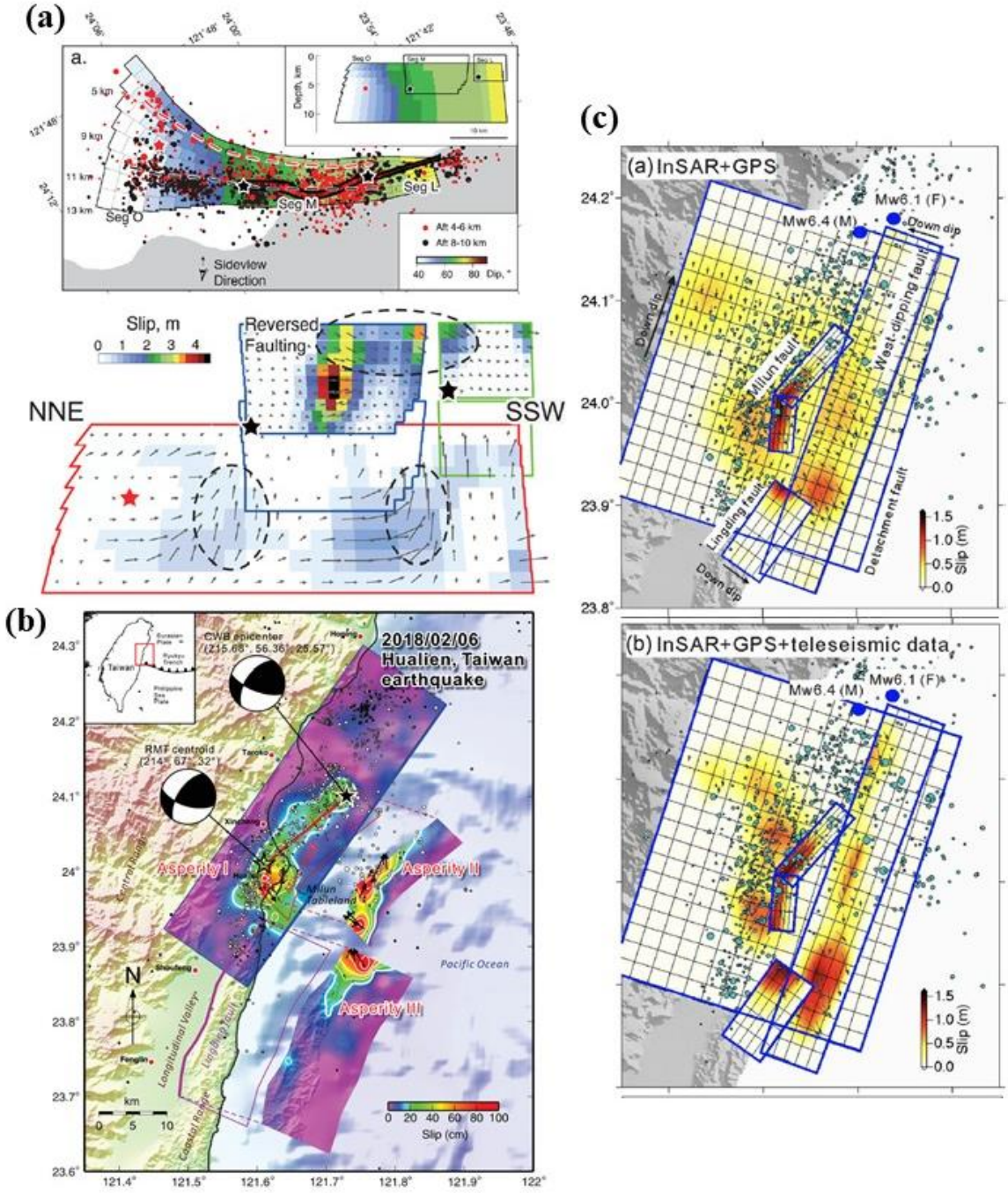

Figure 6.7 The fault slip results from different previous studies. (a) from Lo et al. (2019) (b) from Lee et al. (2018) (c) from Zhao et al. (2020).

doi:10.6342/NTU202202354

Although the setting of the dip angle has some variation, the overall pattern shows the largest fault slip happens on the northernmost of the fault plane, and is very close to the surface. This pattern agrees well with our result. However, the quantitative comparison has some differences. Our result shows the fault slips are all within 1 m, which is similar to the result from Lee et al. (2018) and Zhao et al. (2020) (around 1.2 m). The largest fault slip in Lo et al.'s model even shows more than 2 m. These variations could be related to the types of input data, the quality of data, and the spatial resolution of the data. The largest difference between our input data and theirs is our input data has a higher spatial resolution in a relatively small area. Therefore, we expect our result to be better near the subsurface in the northernmost Lingding Fault. The InSAR images usually have poor coherence in the mountain area, such as the Coastal Range. Nevertheless, our results and previous studies all show that the fault slips in the shallow part of the northern tip.

6.3.3 The behavior of the Lingding Fault in the 2018 Hualien earthquake

Combining the results of earthquake-related structures mapping, the surface displacement across the fault (parallel to the fault component), and the fault slip at depth (Figure 6.8), we can discuss about the behavior of the Lingding Fault during the 2018

doi:10.6342/NTU202202354

Hualien earthquake more comprehensively. First of all, the mapping result shows a clear and almost continuous linear rupture occurred north of the Hualien Bridge (the red line in our mapping result), and to the south, another suspected ruptures (marked in yellow) with a few segments and not as linear as the northern one happened. This result agrees well with the surface displacement and fault slip, because larger fault slip can make the surface deformation more server, and therefore causes clear and continuous linear structures on the surface. This could be the reason that to the south of the Hualien Bridge, there are almost no clear and continuous structures that can be found in the aerial photos.

doi:10.6342/NTU202202354

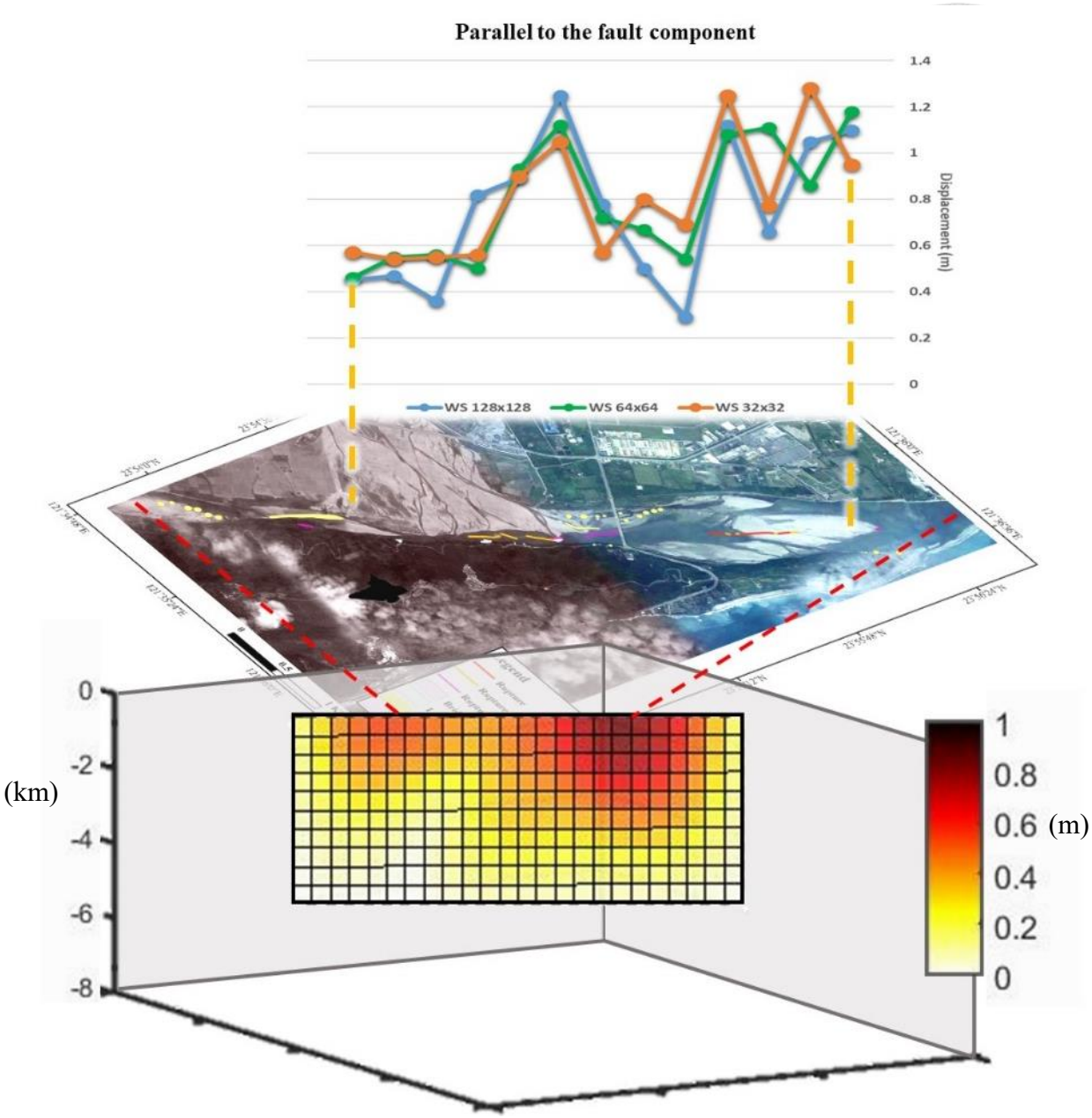

Figure 6.8 The combination of fault-related structures mapping, the displacement along the fault and the fault slip result.

Second, many studies (Jian et al., 2018; Lee et al., 2018) suggest this earthquake includes the movement of at least three structures, starting from an offshore structure, and propagating to the two on-land faults. The Lingding Fault could be the southern

doi:10.6342/NTU202202354

end of this multi-fault rupture. From the displacement pattern of the fault-parallel component, the displacement decreases southward, and becomes little change in the southern profiles. This slip pattern is similar to the “dogtail” slip distribution (Ward, 1997; Zielke et al., 2015), meaning the fault only partially ruptures and can terminate anywhere on the fault plane. Owing to the displacement along the fault gradually decreasing, the profile appearance looks like a dog's tail. Many historical earthquakes have such a rupture pattern, like the 1992 Landers earthquake, 2002 Denali earthquake, and 2010 Darfield earthquake (Zielke et al., 2015). Besides, the fault-to-fault jumping pattern in this earthquake and became the dogtail rupture pattern on the Lingding Fault can be called slip leakage (Sieh, 1996), which means the rupture can propagate across the faults/segments boundary, and forms a dogtail rupture pattern at the rupture termination. Such a rupture pattern can also be found in the 1992 Landers earthquake (Sieh, 1996).

6.4 The regional geological model of the Lingding Fault

The distribution of the seismicity can reveal potential fault planes, because the fault planes are relatively weaker surfaces where earthquakes happen more easily. Therefore, we discuss the distribution of the relocated seismicity from 1990 to 2019, and compare the aftershock (within four weeks) distribution of the 2018 Hualien

doi:10.6342/NTU202202354

earthquake. From the distribution of the thirty-year seismicity, two fault planes can be found (Figure 6.9). The clearer one is a west-dipping plane with a gentle slope, and becomes steeper at depth. Many earthquakes happened on this plane, including most of the aftershocks of the 2018 Hualien earthquake, and concentrated in a narrow zone, which makes the plane obvious. The plane starts beneath the Coastal Range and extends under the Central Range to about 20 km deep. The other fault plane is relatively blurred, with the plane dipping to the east. The seismicity on this plane is beneath the Coastal Range at about 10 to 15 km depth, and extends to the offshore to 40 km deep. It seems that the fault plane is steeper in the shallow part and becomes gentler at depth. Although the seismicity related to this plane is not clear at the shallow depth, we think this plane is the lower part of the Longitudinal Valley Fault, or the Lingding Fault. The velocity model also shows a similar result (Figure 6.10). The tomography is produced by Taiwan Velocity Model, with the velocity model using Huang et al., 2014 and seismicity and focal mechanism from Wu et al., 2008(a, b). The two fault planes can also be found in the Vp/Vs. The Vp/Vs contrast reveals a clear west-dipping plane, with the higher value in the east and the lower value in the west. This plane seems to cut across the Coastal Range, which shows in higher Vp/Vs value, at about 10 km deep. The other plane has higher contrast in the shallow depth (< 10 km deep), which is the boundary between the Coastal Range and the Central Range. But as it extends to the deeper depth, it seems to

doi:10.6342/NTU202202354

pass through the two high Vp/Vs value areas, which might be related to the Coastal Range and the material of forearc basement. The geometry of the two faults is also similar to the seismicity result. In brief, two fault planes can be revealed by the distribution of the seismicity and the tomography. The west-dipping plane locates in the shallow depth, and the east-dipping plane extends to deeper depth.

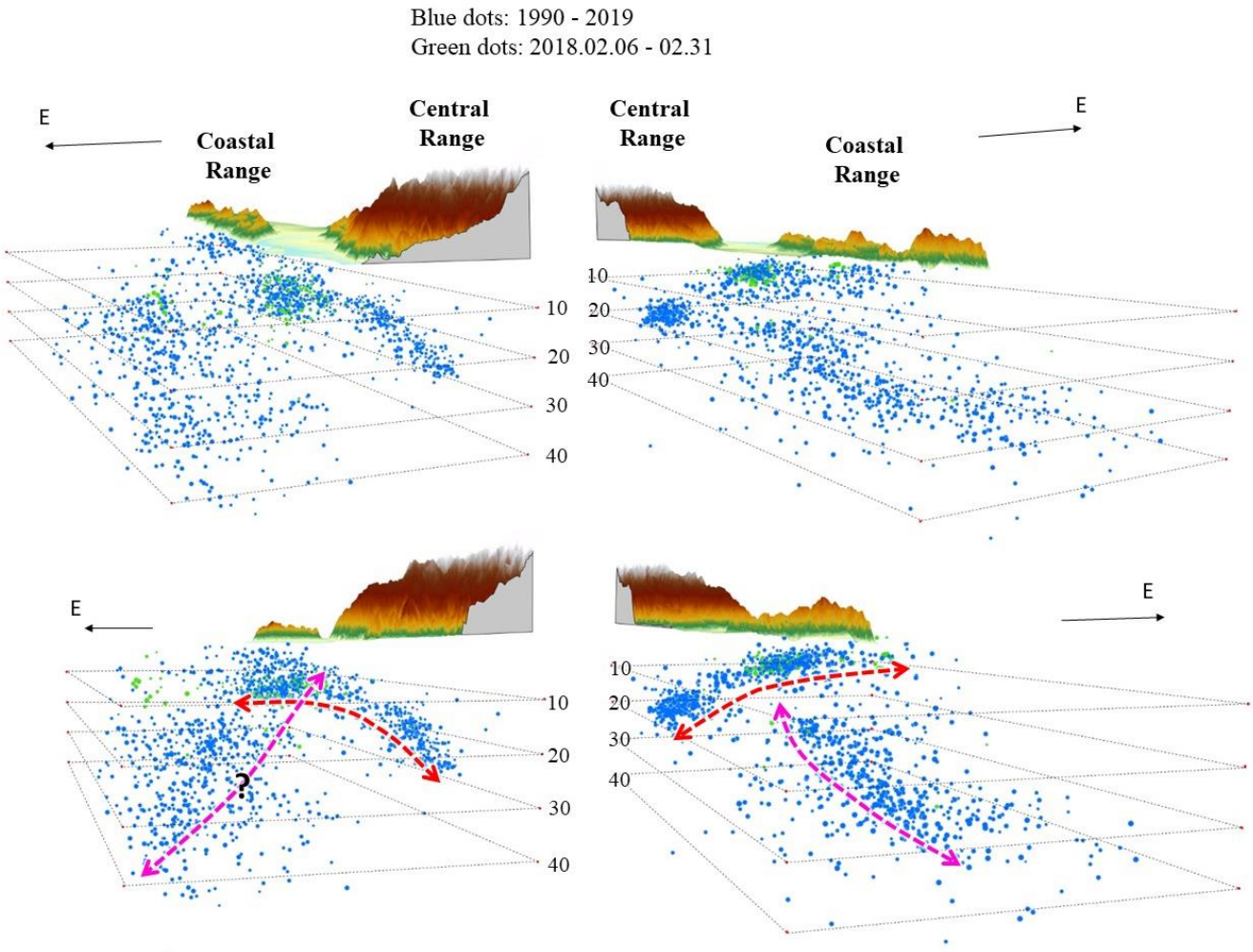

Figure 6.9 The relocated seismicity in research area (provided by Professor Yih-Min Wu). Two fault planes can be found, with west-dipping (red dash line) and east-dipping plane (pink dash line). The upper raw and the lower raw has slight looking angle difference.

doi:10.6342/NTU202202354

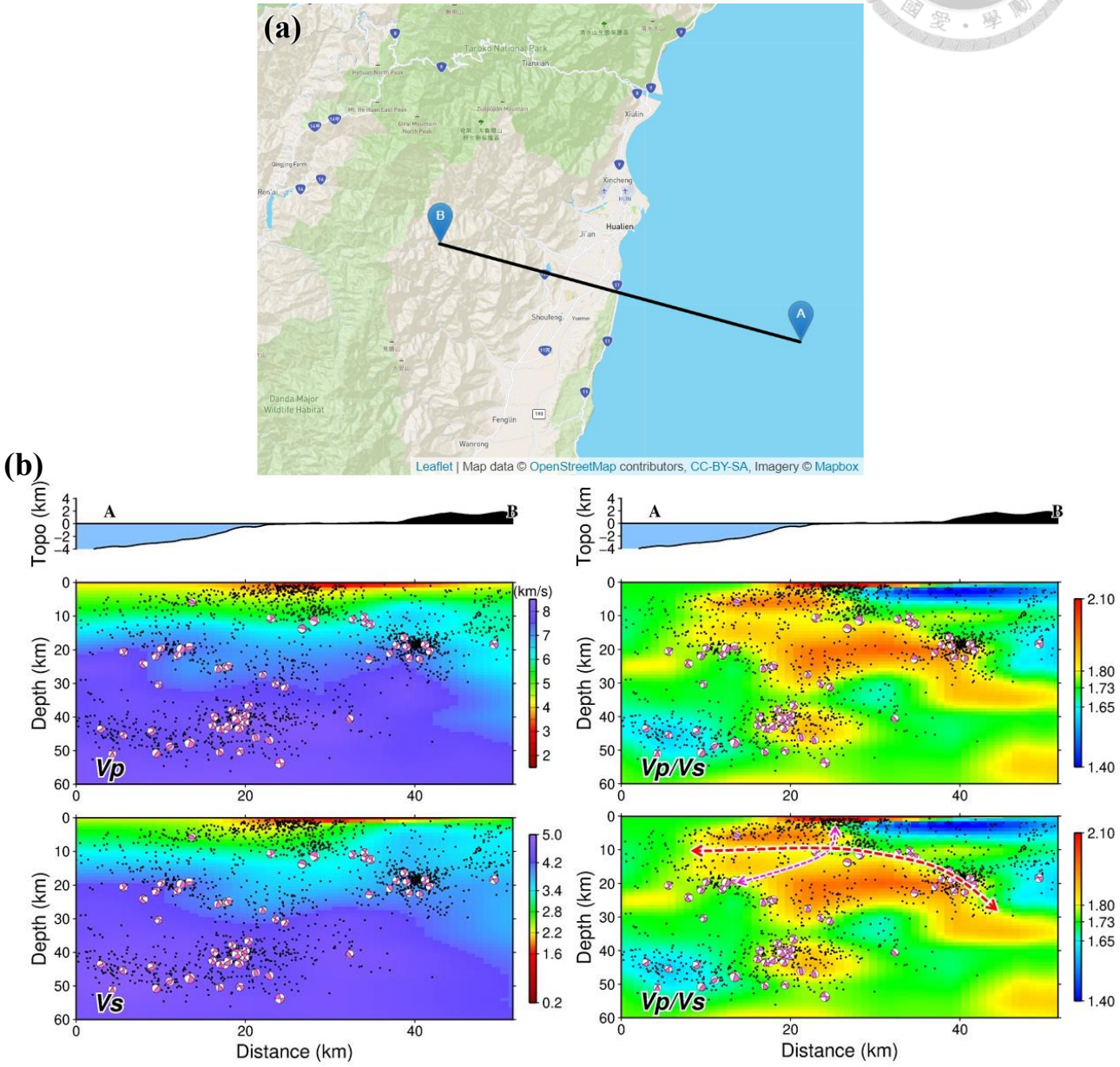

Figure 6.10 (a) The location of the tomography profile. (b) The Vp, Vs, and Vp/Vs velocity model (produced by the Taiwan Velocity Model (http://tecdc.earth.sinica.edu.tw/TWtomo/VerticalProfile.php)

doi:10.6342/NTU202202354

The relation between these two fault planes and the Lingding Fault, the mainshock and the aftershocks of the 2018 Hualien earthquake is still worth exploring. We combine this information together in three dimensions (Figure 6.11). As the result shows, the aftershocks are almost located in the west of the Lingding Fault, and concentrates in the shallow depth. No aftershocks happened on the Lingding Fault plane in our model setting. Most of the aftershocks are distributed to the north and within the range of the Lingding Fault plane. To the south of the Lingding Fault, few aftershocks occurred, which also agrees with our surface deformation and fault slip pattern that the deformation focused on the northernmost part of the Lingding Fault. The distribution of the aftershocks seems to happen on the west-dipping plane, which we mentioned before. More importantly, the mainshock of the 2018 Hualien earthquake could also be related to this plane. Hence, we think this west-dipping fault plane is the main seismogenic source that causes the mainshock and the aftershocks in the 2018 Hualien earthquake. Besides, it seems that the east-dipping plane can connect to the Lingding Fault, but the area where the two faults connect to each other is noisy, owing to the west-dipping fault also passing through. The exact relation between the Lingding Fault and the east-dipping fault plane is still needed to discuss in more detail, but we think these two faults are both the Longitudinal Valley Fault system.

doi:10.6342/NTU202202354

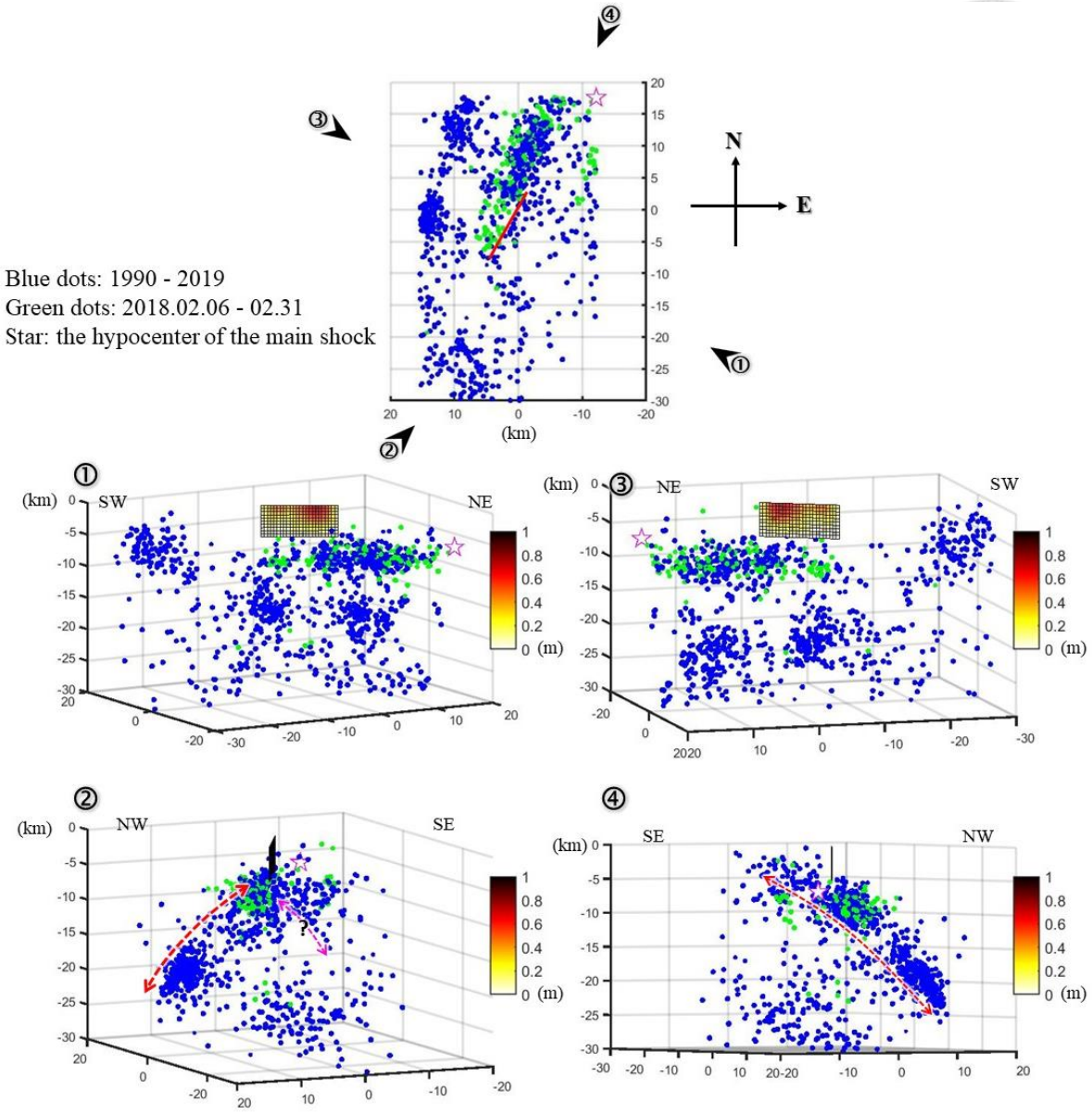

Figure 6.11 The combination of the thirty years seismicity (blue dots), the mainshock (star symbol) and the aftershocks (green dots) of the 2018 Hualien earthquake, and the fault slip and geometry of the Lingding Fault in three dimension. We display their relation in four different angles, and the direction shows in the uppermost raw.

With the thirty-year relocated seismicity, the tomography, the mainshock and the aftershocks of the 2018 Hualien earthquake, and the fault slip and geometry of the Lingding Fault, we discuss what happened in the 2018 Hualien earthquake (Figure

doi:10.6342/NTU202202354

6.12). There are two main faults in this region: a west-dipping fault and an east-dipping fault. The east-dipping fault could be the Longitudinal Valley Fault, or the Lingding Fault, and it is cut across by the west-dipping fault at about 10 km depth. From the seismicity and the aftershocks distribution, the mainshock and most of the aftershocks happened on the west-dipping plane, which indicates the 2018 Hualien earthquake is mostly related to the activity of this fault. The focal mechanism of the mainshock shows the reverse motion component. However, the Coastal Range moves toward the northwest (Yu et al., 1997b; Yu & Kuo, 2001), which is related to the motion of the Philippine Sea Plate. This might indicate that the upper Coastal Range and the lower part move in different velocities toward the northwest, with the lower part moving faster than the upper part. The different movement velocity caused the mainshock of the 2018 Hualien earthquake, and the stress propagated upward to the Lingding Fault, which lies above the west-dipping fault. Therefore, the fault slip on the Lingding Fault is mainly concentrated in the shallow depth. Then the aftershocks occurred on the lower part of the west-dipping fault to release the stress, mostly within the depth of 15 km. Our study area locates in a complicated structural region. The regional geological model is proposed by only some evidence. More data, materials and methods are needed to examine our model's accuracy.

doi:10.6342/NTU202202354

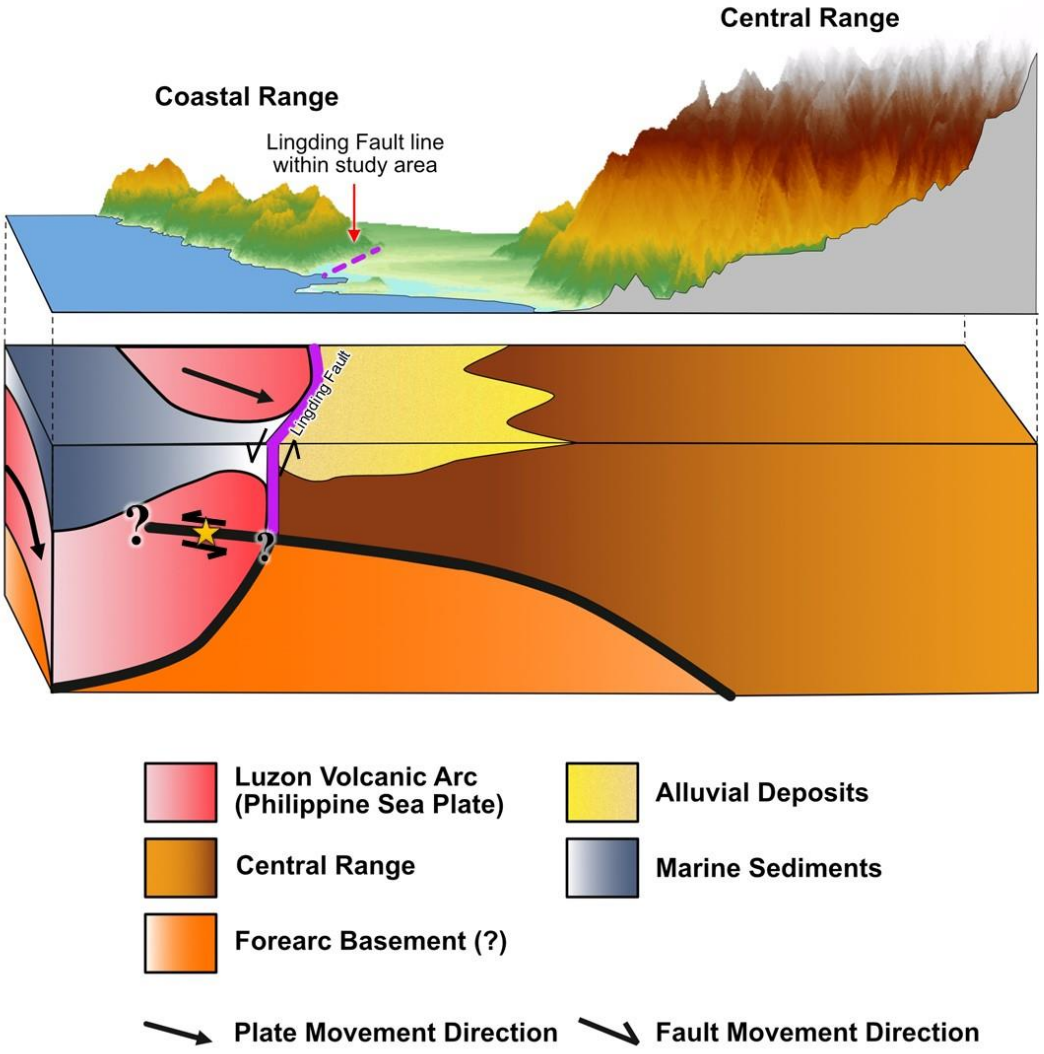

Figure 6.12 The regional geological structure model of the Lingding Fault. The star is the 2018 Hualien earthquake mainshock.

doi:10.6342/NTU202202354

6.5 The relation between the Lingding Fault and the Milun Fault

The relationship between the Lingding Fault and the Milun Fault has been unclear for many years. For example, whether the two faults can connect together? What is the link between the regional geological setting and the movement pattern or growth of these two faults? The 2018 Hualien earthquake might give some hints about their relationship (Lee et al., 2018; Lo et al., 2019; Yen et al., 2018), but a more detailed discussion still needs more information to improve, such as seismicity at deeper depth, the shallow seismic profiles between the two faults, etc. Here, we briefly summarize what happened to these two faults during the 2018 Hualien earthquake, and discuss their relationship.

First of all, the materials to the east of the faults differ from the geological evidence. The east of the Milun Fault is composed of the Milun Conglomerate, which is related to the shallow marine facies in Pleistocene (謝和鄧，1994), while to the east of the Lingding Fault is Tuluanshan Formation, which is the volcanic breccia and epiclastics in Miocene and Pliocene (Teng et al., 1988). Therefore, the formation of these two faults seems to be different owing to the lithological boundary. The Lingding Fault should be related to the plate boundary.

doi:10.6342/NTU202202354

Second, although the fault behavior is similar for the horizontal component (both are left-lateral strike-slip fault and the offsets decreased toward the south), the vertical component has some discrepancies (Figure 6.13). The motion of the Milun Fault is with reverse component, but the Lingding Fault is with normal component (CGS, 2018). Hence, the two faults seem to be separate. Because it is rare for a strike-slip fault to behave in opposite vertical motion in different parts. Besides, the displacement of the eastern Milun Fault is clockwise rotation (Figure 3.7a) (Yen et al., 2018). However, there is no obvious rotation that happened on the Lingding Fault. The scenario is similar to the model proposed by Chen et al. (2014). The northward motion of the Coastal Range makes the Hualien Tableland (east of the Milun Fault) escape eastward, which could explain the formation of the Milun Fault.

Third, the fault geometry of the two faults is also hard to connect. The Milun Fault is curved, while the Lingding Fault is relatively straight (almost along the Coastal Range) (Figure 6.13). Although the fault dip is varied for the Milun Fault (Kuo et al., 2018), the southern part is around 60° - 65°, which is gentler than the fault dip of the Lingding Fault, larger than 75°. Based on the information, we think the Milun Fault and the Lingding Fault cannot connect together. Both of them are shallow and relatively minor structures within the geological setting in this area. The interaction between the two faults and relation in the deeper depth or connection to the regional geological

doi:10.6342/NTU202202354

setting is still unclear with the information in this earthquake. The topics about the detailed regional setting in this complicated area and the connection to the two shallow faults, the Milun Fault and the Lingding Fault, are worth exploring in the future.

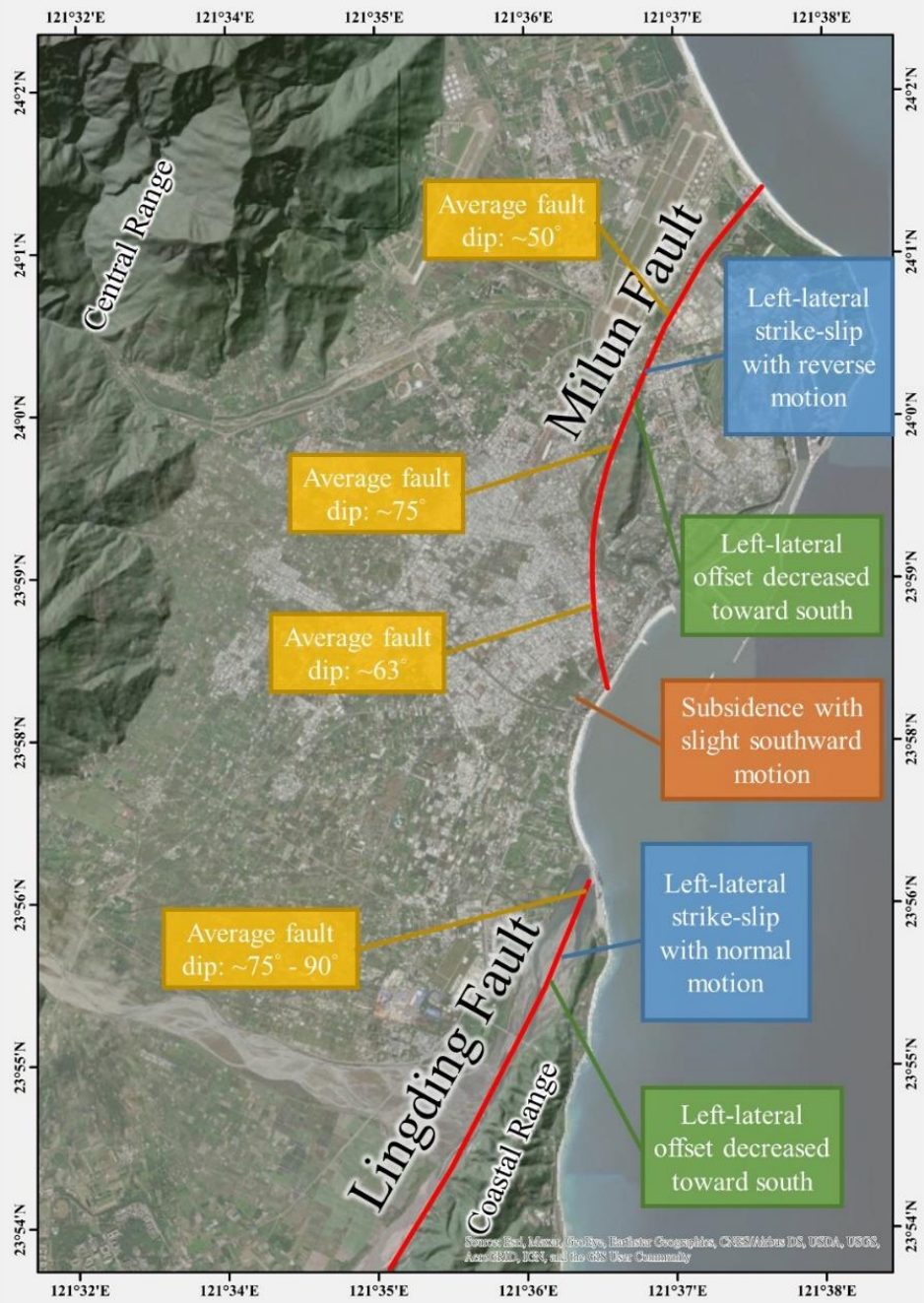

Figure 6.13 The displacement and the fault geometry from the 2018 Hualien earthquake around the Milun Fault and the Lingding Fault area. The information is from Kuo et al. (2018), Lee et al. (2018), Lo et al. (2019), Tung et al. (2019), Yen et al. (2018).

doi:10.6342/NTU202202354

7. Conclusion

This study uses the pre- and post-earthquake aerial photos to study the surface deformation of the Lingding Fault in the 2018 Hualien earthquake by the sub-pixel correlation (using COSI-Corr software package). The result shows the fault behaved in the left-lateral strike-slip motion in this earthquake. From the visual inspection of the different periods of the images and the surface deformation pattern, the Lingding Fault trace is located in the Hualien River, and larger surface deformation happened in the northernmost of the fault, with the straight and clearly linear structure on the sandbar. We use the result of the COSI-Corr and the GNSS data to inverse the fault slip at depth. The result shows the larger fault slips mainly focus on the northern part of the Lingding Fault and concentrate within the shallow depth (<5 km depth). The behavior of the Lingding Fault acts as the dogtail rupture pattern in this earthquake.

Our study deciphers the regional geological structure model based on the seismicity and the 2018 Hualien earthquake. Two fault planes are revealed by the seismicity, with opposite dipping directions. The tomography also supports the existence of these two fault planes. We found the 2018 Hualien earthquake is mostly related to the west-dipping fault because of the mainshock location and the distribution of the aftershocks in three dimensions. The stress propagated to the shallow fault above,

doi:10.6342/NTU202202354

and caused the Lingding Fault to rupture. Based on the fault slip inversion result and the distribution of the aftershocks, the Lingding Fault only deformed in the northern part in this earthquake. As for the exact relationship between the Lingding Fault, the east-dipping and the west-dipping faults, our study cannot give a more detailed discussion. More earthquake events in this region and seismicity are needed to solve this puzzle. But overall, our study reveals the behavior of the Lingding Fault in the 2018 Hualien earthquake and its connection to the regional structural setting.

doi:10.6342/NTU202202354

References

林亞嫻，2020，1999 年集集地震後濁水溪河道變遷。 [碩士論文: 國立臺灣大學]

廖昱茨，2014，利用持久散射體雷達干涉技術與 ALOS 影像探討台灣東部縱谷斷層北段的分段特性。[碩士論文: 國立台灣大學]

謝一銘，2017，台灣花東縱谷北段反射震測調查。[碩士論文: 國立中央大學]

謝孟龍、鄧屬予(1994)。米崙礫岩的岩相及沉積環境。地質，第 14 卷，第 1 期，第 201-217 頁。

鍾佩瑜，2019，利用密集地震網探討花東縱谷北段地下速度構造。[碩士論文: 國立中央大學]

簡立凱，2015，花東縱谷斷層之地電研究。[博士論文: 國立中央大學]

陳文山、林益正、顏一勤、楊志成、紀權宥、黃能偉、林啟文、林偉雄、侯進雄、劉彥求、林燕慧、石同生、盧詩丁（2008）從古地震研究與 GPS 資料探討縱谷斷層的分段意義。經濟部中央地質調查所特刊，第 20 號，第 165-191 頁。

陳文山、吳逸民、葉柏逸、賴奕修、柯明淳、柯孝勳、林義凱 (2018)。臺灣東部碰撞帶孕震構造。經濟部中央地質調查所特刊，第 33 號，123-155。

Avouac, J.-P., Ayoub, F., Leprince, S., Konca, O., & Helmberger, D. V. (2006). The 2005, Mw 7.6 Kashmir earthquake: Sub-pixel correlation of ASTER images and seismic waveforms analysis. *Earth and Planetary Science Letters, 249*(3-4), 514-528.

Avouac, J.-P., Ayoub, F., Wei, S., Ampuero, J.-P., Meng, L., Leprince, S., Jolivet, R., Duputel, Z., & Helmberger, D. (2014). The 2013, Mw 7.7 Balochistan earthquake, energetic strike-slip reactivation of a thrust fault. *Earth and Planetary Science Letters, 391*, 128-134.

Baird, T., Bristow, C. S., & Vermeesch, P. (2019). Measuring sand dune migration rates

doi:10.6342/NTU202202354

with COSI-Corr and landsat: Opportunities and challenges. *Remote Sensing,* 11(20), 2423.

Barrier, E., & Angelier, J. (1986). Active collision in eastern Taiwan: the Coastal Range. *Tectonophysics,* 125(1-3), 39-72.

Bemis, S. P., Micklethwaite, S., Turner, D., James, M. R., Akciz, S., Thiele, S. T., & Bangash, H. A. (2014). Ground-based and UAV-based photogrammetry: A multi-scale, high-resolution mapping tool for structural geology and paleoseismology. *Journal of Structural Geology, 69*, 163-178.

Binet, R., & Bollinger, L. (2005). Horizontal coseismic deformation of the 2003 Bam (Iran) earthquake measured from SPOT-5 THR satellite imagery. *Geophysical Research Letters, 32*(2).

Chemenda, A. I., Yang, R. K., Hsieh, C. H., & Groholsky, A. L. (1997). Evolutionary model for the Taiwan collision based on physical modelling. *Tectonophysics, 274*(1-3), 253-274.

Chen, C. Y., Lee, J. C., Chen, Y. G., & Chen, R. F. (2014). Campaigned GPS on present-day crustal deformation in northernmost Longitudinal Valley preliminary results, Hualien Taiwan. *Terrestrial, Atmospheric and Oceanic Sciences, 25*(3), 337-357.

Chen, K. H., Toda, S., & Rau, R. J. (2008). A leaping, triggered sequence along a segmented fault: The 1951 M_L 7.3 Hualien-Taitung earthquake sequence in eastern Taiwan. *Journal of Geophysical Research: Solid Earth, 113*(B2).

CGS (2018). Geological Report of 2018 Hualien Earthquake, Central Geological Survey report, Taipei, 131 pp. (in Chinese)

De Michele, M., Raucoules, D., Lasserre, C., Pathier, E., Klinger, Y., Van Der Woerd, J., De Sigoyer, J., & Xu, X. (2010). The Mw 7.9, 12 May 2008 Sichuan earthquake rupture measured by sub-pixel correlation of ALOS PALSAR amplitude images. *Earth, planets and space, 62*(11), 875-879.

doi:10.6342/NTU202202354

DeMets, C., Gordon, R. G., & Argus, D. F. (2010). Geologically current plate motions. *Geophysical Journal International, 181*(1), 1-80.

Dominguez, S., Avouac, J. P., & Michel, R. (2003). Horizontal coseismic deformation of the 1999 Chi-Chi earthquake measured from SPOT satellite images: Implications for the seismic cycle along the western foothills of central Taiwan. *Journal of Geophysical Research: Solid Earth, 108*(B2).

Gomez, C., Hayakawa, Y., & Obanawa, H. (2015). A study of Japanese landscapes using structure from motion derived DSMs and DEMs based on historical aerial photographs: New opportunities for vegetation monitoring and diachronic geomorphology. *Geomorphology, 242*, 11-20.

Herman, F., Anderson, B., & Leprince, S. (2011). Mountain glacier velocity variation during a retreat/advance cycle quantified using sub-pixel analysis of ASTER images. *Journal of Glaciology, 57*(202), 197-207.

Hermas, E., Leprince, S., & Abou El-Magd, I. (2012). Retrieving sand dune movements using sub-pixel correlation of multi-temporal optical remote sensing imagery, northwest Sinai Peninsula, Egypt. *Remote Sensing of Environment, 121*, 51-60.

Hollingsworth, J., Ye, L., & Avouac, J. P. (2017). Dynamically triggered slip on a splay fault in the Mw 7.8, 2016 Kaikoura (New Zealand) earthquake. *Geophysical Research Letters, 44*(8), 3517-3525.

Hsu, S. K. (2001). Subduction/collision complexities in the Taiwan-Ryukyu junction area: Tectonics of the northwestern corner of the Philippine Sea plate. *Terrestrial, Atmospheric and Oceanic Sciences, 12*(SUPP), 209-230.

Hsu, Y. C., Chang, C. P., Yen, J. Y., Kuo-Chen, H., & Wang, C. C. (2019). Investigating the structure of the Milun Fault from surface ruptures of the 2018 Hualien Earthquake. *Terrestrial, Atmospheric and Oceanic Sciences, 30*(3), 337-350.

Huang, H. H., Wu, Y. M., Song, X., Chang, C. H., Lee, S. J., Chang, T. M., & Hsieh, H.

doi:10.6342/NTU202202354

H. (2014). Joint Vp and Vs tomography of Taiwan: Implications for subduction-collision orogeny. *Earth and Planetary Science Letters, 392,* 177-191.

Huang, M. H., Tung, H., Fielding, E. J., Huang, H. H., Liang, C., Huang, C., & Hu, J. C. (2016). Multiple fault slip triggered above the 2016 Mw 6.4 MeiNong earthquake in Taiwan. *Geophysical Research Letters, 43*(14), 7459-7467.

Huang, M. H., & Huang, H. H. (2018). The complexity of the 2018 Mw 6.4 Hualien earthquake in east Taiwan. *Geophysical Research Letters, 45*(24), 13,249-13,257.

Huang, S. Y., Yen, J. Y., Wu, B. L., Yen, I. C., & Chuang, R. Y. (2019). Investigating the Milun Fault: The coseismic surface rupture zone of the 2018/02/06 M_L 6.2 Hualien earthquake, Taiwan. *Terrestrial, Atmospheric and Oceanic Sciences, 30*(3), 311-335.

James, M. R., & Robson, S. (2012). Straightforward reconstruction of 3D surfaces and topography with a camera: Accuracy and geoscience application. *Journal of Geophysical Research: Earth Surface, 117*(F3).

Jian, P. R., Hung, S. H., & Meng, L. (2018). Rupture Behavior and Interaction of the 2018 Hualien Earthquake Sequence and Its Tectonic Implication. *Seismological Research Letters, 90*(1), 68-77.

Ko, Y. Y., Hsu, S. Y., Yang, H. C., Lu, C. C., Hwang, Y. W., Liu, C. H., & Hwang, J. H. (2018). Soil Liquefaction and Ground Settlements in 6 February 2018 Hualien, Taiwan, Earthquake. *Seismological Research Letters, 90*(1), 51-59.

Kuochen, H., Wu, Y. M., Chang, C. H., Hu, J. C., & Chen, W. S. (2004). Relocation of eastern Taiwan earthquakes and tectonic implications. *Terrestrial, Atmospheric and Oceanic Sciences, 15*(4), 647-666.

Kuo-Chen, H., Guan, Z. K., Sun, W. F., Jhong, P. Y., & Brown, D. (2018). Aftershock Sequence of the 2018 Mw 6.4 Hualien Earthquake in Eastern Taiwan from a

doi:10.6342/NTU202202354

Dense Seismic Array Data Set. *Seismological Research Letters, 90*(1), 60-67.

Kuo, Y. T., Ayoub, F., Leprince, S., Chen, Y. G., Avouac, J. P., Shyu, J. B. H., Lai, K. Y., & Kuo, Y. J. (2014). Coseismic thrusting and folding in the 1999 Mw 7.6 Chi-Chi earthquake: A high-resolution approach by aerial photos taken from Tsaotun, central Taiwan. *Journal of Geophysical Research: Solid Earth, 119*(1), 645-660.

Kuo, Y. T., Wang, Y., Hollingsworth, J., Huang, S. Y., Chuang, R. Y., Lu, C. H., Hsu, Y. C., Tung, H., Yen, J. Y., & Chang, C. P. (2018). Shallow Fault Rupture of the Milun Fault in the 2018 Mw 6.4 Hualien Earthquake: A High-Resolution Approach from Optical Correlation of Pléiades Satellite Imagery. *Seismological Research Letters, 90*(1), 97-107.

Lee, S. J., Lin, T. C., Liu, T. Y., & Wong, T. P. (2018). Fault-to-Fault Jumping Rupture of the 2018 Mw 6.4 Hualien Earthquake in Eastern Taiwan. *Seismological Research Letters, 90*(1), 30-39.

Leprince, S., Barbot, S., Ayoub, F., & Avouac, J.-P. (2007). Automatic and precise orthorectification, coregistration, and subpixel correlation of satellite images, application to ground deformation measurements. *IEEE Transactions on Geoscience and Remote Sensing, 45*(6), 1529-1558.

Lin, Y. S., Chuang, R. Y., Yen, J. Y., Chen, Y. C., Kuo, Y. T., Wu, B. L., Huang, S. Y., & Yang, C. J. (2019). Mapping surface breakages of the 2018 Hualien earthquake by using UAS photogrammetry. *Terrestrial, Atmospheric and Oceanic Sciences, 30*(3), 351-366.

Lo, Y. C., Yue, H., Sun, J., Zhao, L., & Li, M. (2019). The 2018 Mw6. 4 Hualien earthquake: dynamic slip partitioning reveals the spatial transition from mountain building to subduction. *Earth and Planetary Science Letters, 524*, 115729.

Michel, R., Avouac, J. P., & Taboury, J. (1999). Measuring ground displacements from

doi:10.6342/NTU202202354

SAR amplitude images: Application to the Landers earthquake. *Geophysical Research Letters, 26*(7), 875-878.

Michel, S., Avouac, J.-P., Ayoub, F., Ewing, R. C., Vriend, N., & Heggy, E. (2018). Comparing dune migration measured from remote sensing with sand flux prediction based on weather data and model, a test case in Qatar. *Earth and Planetary Science Letters, 497*, 12-21.

Miles, B. W. J., Jordan, J. R., Stokes, C. R., Jamieson, S. S. R., Gudmundsson, G. H., & Jenkins, A. (2021). Recent acceleration of Denman Glacier (1972–2017), East Antarctica, driven by grounding line retreat and changes in ice tongue configuration. *The Cryosphere, 15*(2), 663-676.

Milliner, C. W. D., Dolan, J. F., Hollingsworth, J., Leprince, S., Ayoub, F., & Sammis, C. G. (2015). Quantifying near-field and off-fault deformation patterns of the 1992 Mw 7.3 Landers earthquake. *Geochemistry, Geophysics, Geosystems, 16*(5), 1577-1598.

Milliner, C. W. D., Dolan, J. F., Hollingsworth, J., Leprince, S., & Ayoub, F. (2016). Comparison of coseismic near-field and off-fault surface deformation patterns of the 1992 Mw 7.3 Landers and 1999 Mw 7.1 Hector Mine earthquakes: Implications for controls on the distribution of surface strain. *Geophysical Research Letters, 43*(19), 10,115-10,124.

Okada, Y. (1985). Surface deformation due to shear and tensile faults in a half-space. *Bulletin of the seismological society of America, 75*(4), 1135-1154.

Peyret, M., Dominguez, S., Cattin, R., Champenois, J., Leroy, M., & Zajac, A. (2011). Present-day interseismic surface deformation along the Longitudinal Valley, eastern Taiwan, from a PS-InSAR analysis of the ERS satellite archives. *Journal of Geophysical Research: Solid Earth, 116*(B3).

Piermattei, L., Carturan, L., de Blasi, F., Tarolli, P., Dalla Fontana, G., Vettore, A., &

doi:10.6342/NTU202202354

Pfeifer, N. (2016). Suitability of ground-based SfM–MVS for monitoring glacial and periglacial processes. *Earth Surface Dynamics, 4*(2), 425-443.

Saito, H., Uchiyama, S., Hayakawa, Y. S., & Obanawa, H. (2018). Landslides triggered by an earthquake and heavy rainfalls at Aso volcano, Japan, detected by UAS and SfM-MVS photogrammetry. *Progress in Earth and Planetary Science, 5*(1), 1-10.

Shyu, J. B. H., Sieh, K., & Chen, Y. G. (2005). Tandem suturing and disarticulation of the Taiwan orogen revealed by its neotectonic elements. *Earth and Planetary Science Letters, 233*(1-2), 167-177.

Shyu, J. B. H., Sieh, K., Chen, Y. G., & Chung, L. H. (2006). Geomorphic analysis of the Central Range fault, the second major active structure of the Longitudinal Valley suture, eastern Taiwan. *Geological Society of America Bulletin, 118*(11-12), 1447-1462.

Shyu, J. B. H., Chung, L. H., Chen, Y. G., Lee, J. C., & Sieh, K. (2007). Re-evaluation of the surface ruptures of the November 1951 earthquake series in eastern Taiwan, and its neotectonic implications. *Journal of Asian Earth Sciences, 31*(3), 317-331.

Shyu, J. B. H., Chuang, Y. R., Chen, Y. L., Lee, Y. R., & Cheng, C. T. (2016a). A New On-Land Seismogenic Structure Source Database from the Taiwan Earthquake Model (TEM) Project for Seismic Hazard Analysis of Taiwan. *Terrestrial, Atmospheric & Oceanic Sciences, 27*(3), 311-323.

Shyu, J. B. H., Chen, C. F., & Wu, Y. M. (2016b). Seismotectonic characteristics of the northernmost Longitudinal Valley, eastern Taiwan: Structural development of a vanishing suture. *Tectonophysics, 692*, 295-308.

Sibuet, J.-C., & Hsu, S. K. (2004). How was Taiwan created? *Tectonophysics, 379*(1-4), 159-181.

doi:10.6342/NTU202202354

Sieh, K. (1996). The repetition of large-earthquake ruptures. *Proceedings of the National Academy of Sciences, 93*(9), 3764-3771.

Teng, L. S., Chen, W. S., Wang, Y., Song, S. R., & Lo, H. J. (1988). Toward a comprehensive stratigraphic system of the Coastal Range, eastern Taiwan. *Acta Geologica Taiwanica, 26,* 19-36.

Teng, L. S. (1990). Geotectonic evolution of late Cenozoic arc-continent collision in Taiwan. *Tectonophysics, 183*(1-4), 57-76.

Tian, S., Gardoni, P., & Yuan, W. (2018). Coseismic Deformation of the 6 February 2018 Mw 6.2 Hualien Earthquake Based on Strong-Motion Recordings. *Seismological Research Letters, 90*(1), 108-117.

Toyokuni, G., Zhao, D., & Chen, K. H. (2021). Structural control on the 2018 and 2019 Hualien earthquakes in Taiwan. *Physics of the Earth and Planetary Interiors, 312*, 106673.

Tung, H., Chen, H. Y., Hsu, Y. J., Hu, J. C., Chang, Y. H., & Kuo, Y. T. (2019). Triggered slip on multifaults after the 2018 Mw 6.4 Hualien earthquake by continuous GPS and InSAR measurements. *Terrestrial, Atmospheric and Oceanic Sciences, 30*(3), 285-300.

Ward, S. N. (1997). Dogtails versus rainbows: Synthetic earthquake rupture models as an aid in interpreting geological data. *Bulletin of the seismological society of America, 87*(6), 1422-1441.

Wen, S., Wen, Y. Y., Ching, K. E., Yeh, Y. L., & Lee, Y. H. (2019). Tectonic implications on the 2018 Hualien Earthquake. *Terrestrial, Atmospheric and Oceanic Sciences, 30*(3), 389-398.

Wen, Y. Y., Wen, S., Lee, Y. H., & Ching, K. E. (2019). The kinematic source analysis for 2018 Mw 6.4 Hualien, Taiwan earthquake. *Terrestrial, Atmospheric and Oceanic Sciences, 30*(3), 377-387.

doi:10.6342/NTU202202354

Wu, B. L., Yen, J. Y., Huang, S. Y., Kuo, Y. T., & Chang, W. Y. (2019). Surface deformation of 0206 Hualien earthquake revealed by the integrated network of RTK GPS. *Terrestrial, Atmospheric and Oceanic Sciences, 30*(3), 301-310.

Wu, F. T., Liang, W. T., Lee, J. C., Benz, H., & Villasenor, A. (2009). A model for the termination of the Ryukyu subduction zone against Taiwan: A junction of collision, subduction/separation, and subduction boundaries. *Journal of Geophysical Research: Solid Earth, 114*(B7).

Wu, Y. M., Chang, C. H., Zhao, L., Teng, T. L., & Nakamura, M. (2008a). A comprehensive relocation of earthquakes in Taiwan from 1991 to 2005. *Bulletin of the seismological society of America, 98*(3), 1471-1481.

Wu, Y. M., Zhao, L., Chang, C. H., & Hsu, Y. J. (2008b). Focal-mechanism determination in Taiwan by genetic algorithm. *Bulletin of the seismological society of America, 98*(2), 651-661.

Xu, X., Tong, X., Sandwell, D. T., Milliner, C. W. D., Dolan, J. F., Hollingsworth, J., Leprince, S., & Ayoub, F. (2016). Refining the shallow slip deficit. *Geophysical Journal International, 204*(3), 1867-1886.

Yang, Y. H., Hu, J. C., Tung, H., Tsai, M. C., Chen, Q., Xu, Q., Zhang, Y. J., Zhao, J. J., Liu, G. X., Xiong, J. N., Wang, J. Y., Yu, B., Chiu, C. Y., & Su, Z. (2018). Co-seismic and postseismic fault models of the 2018 Mw 6.4 Hualien earthquake occurred in the junction of collision and subduction boundaries offshore eastern Taiwan. *Remote Sensing, 10*(9), 1372.

Yen, J. Y., Lu, C. H., Dorsey, R. J., Kuo-Chen, H., Chang, C. P., Wang, C. C., Chuang, R. Y., Kuo, Y. T., Chiu, C. Y., Chang, Y. H., Bovenga, F., & Chang, W. Y. (2018). Insights into Seismogenic Deformation during the 2018 Hualien, Taiwan, Earthquake Sequence from InSAR, GPS, and Modeling. *Seismological Research Letters, 90*(1), 78-87.

doi:10.6342/NTU202202354

Yu, S. B., Chen, H. Y., & Kuo, L. C. (1997). Velocity field of GPS stations in the Taiwan area. *Tectonophysics, 274*(1-3), 41-59.

Yu, S. B., & Kuo, L. C. (2001). Present-day crustal motion along the Longitudinal Valley Fault, eastern Taiwan. *Tectonophysics, 333*(1-2), 199-217.

Zhao, D., Qu, C., Shan, X., Bürgmann, R., Gong, W., Tung, H., Zhang, G., Song, X., & Qiao, X. (2020). Multifault complex rupture and afterslip associated with the 2018 M w 6.4 Hualien earthquake in northeastern Taiwan. *Geophysical Journal International, 224*(1), 416-434.

Zielke, O., Klinger, Y., & Arrowsmith, J. R. (2015). Fault slip and earthquake recurrence along strike-slip faults—Contributions of high-resolution geomorphic data. *Tectonophysics, 638*, 43-62.

Zinke, R., Hollingsworth, J., & Dolan, J. F. (2014). Surface slip and off-fault deformation patterns in the 2013 Mw 7.7 Balochistan, Pakistan earthquake: Implications for controls on the distribution of near-surface coseismic slip. *Geochemistry, Geophysics, Geosystems, 15*(12), 5034-5050.

doi:10.6342/NTU202202354

Supplementary

Supplementary 1: The situation of the aerial photos overlapping (a) pre-event (b) post-event

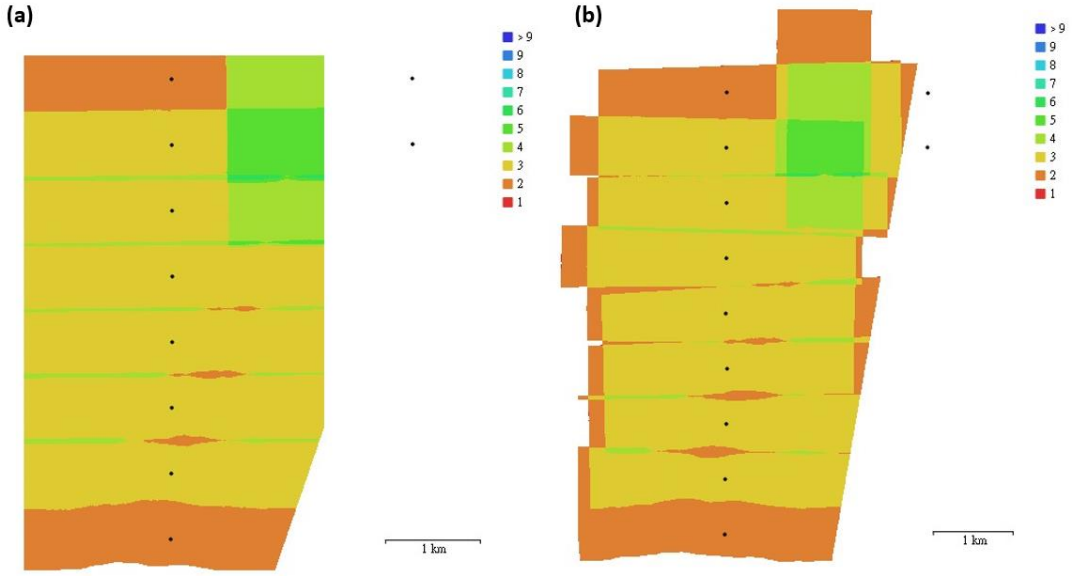

Supplementary 2: The SPOT 7 images and the area we used for calculation of sub-pixel correlation (a) pre-event (b) post-event

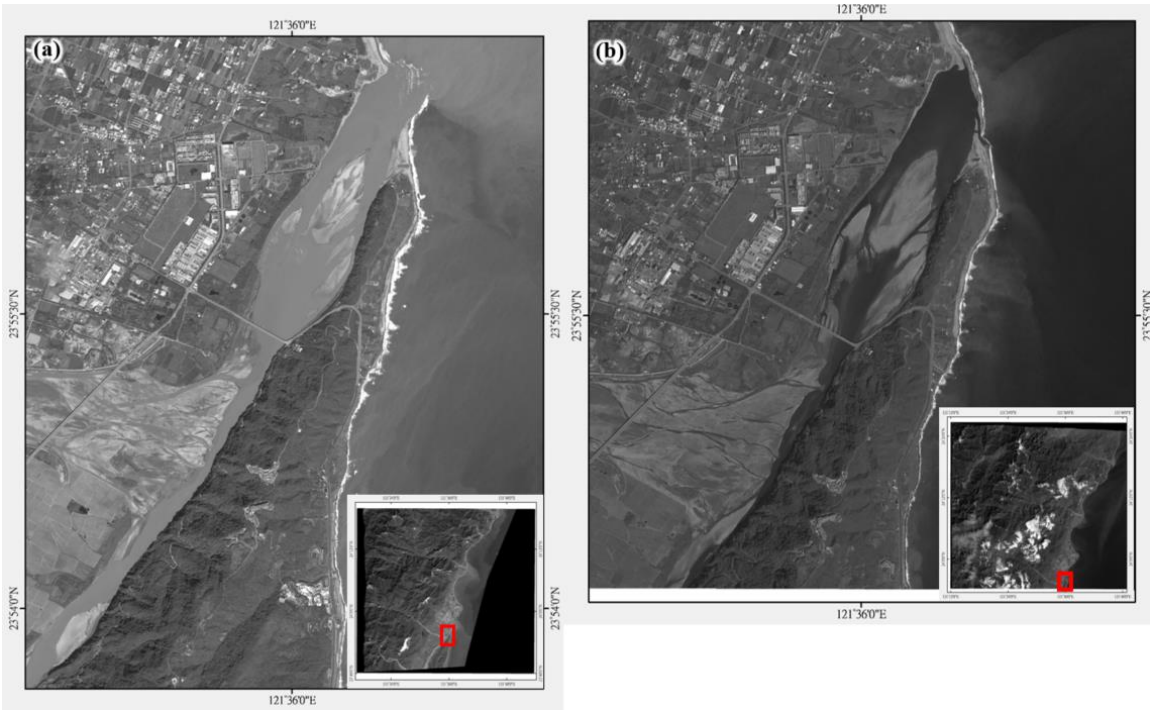

doi:10.6342/NTU202202354

Supplementary 3: The estimated error of the GCPs and ChPs (a) pre-event (b) post-event

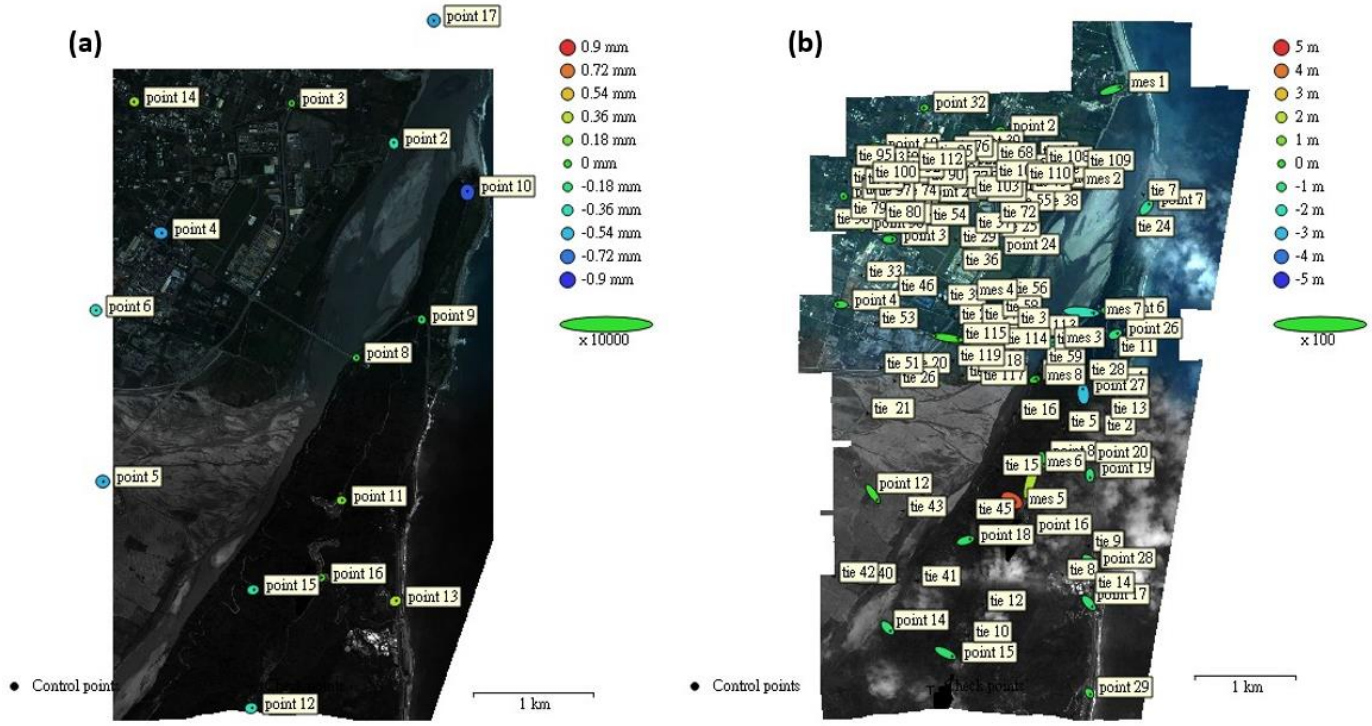

Pre-event GCPs

#Label	X/Longitude	Y/Latitude	Z/Altitude	Accuracy_X/Y/Z_(m)	Error_(m)	X_error	Y_error	Z_error	X_est	Y_est	Z_est
point 2	121.603374	23.938763	6	0.005	0.001415	-0.000269	0.001354	-0.000311	121.603374	23.938763	5.999689
point 3	121.595026	23.941709	14	0.005	0.000193	0.000055	0.000185	0.000011	121.595026	23.941709	14.000011
point 4	121.584387	23.931955	26	0.005	0.00153	0.001401	-0.000111	-0.000604	121.584387	23.931955	25.999396
point 5	121.579615	23.913278	24	0.005	0.001087	0.000926	-0.000045	-0.000568	121.579615	23.913278	23.999432
point 6	121.579028	23.926133	30	0.005	0.000749	0.000556	-0.00031	-0.000394	121.579028	23.926133	29.999606
point 8	121.600319	23.922587	14	0.005	0.000252	0.00014	0.000207	-0.000037	121.600319	23.922587	13.999963
point 9	121.605663	23.925473	31	0.005	0.000665	-0.000258	0.000601	-0.000121	121.605663	23.925473	30.999879
point 10	121.609406	23.935097	20	0.005	0.001939	-0.000038	0.001764	-0.000803	121.609406	23.935097	19.999197
point 11	121.599164	23.911862	176	0.005	0.00122	0.001205	-0.000076	0.000173	121.599164	23.911862	176.000173
point 12	121.591803	23.89627	318	0.005	0.001943	0.001892	0.000266	-0.000354	121.591803	23.89627	317.999646
point 13	121.603581	23.904327	14	0.005	0.00164	0.001433	0.000724	0.000332	121.603581	23.904327	14.000332
point 14	121.58212	23.941819	28	0.005	0.000595	-0.000528	-0.000025	0.000273	121.58212	23.941819	28.000273
point 15	121.591955	23.905151	73	0.005	0.001886	0.001843	0.000285	-0.000285	121.591955	23.905151	72.999715
point 16	121.59747	23.906073	225	0.005	0.002098	0.001964	0.000729	0.000109	121.59747	23.906073	225.000109
point 17	121.606662	23.947928	11	0.005	0.000605	-0.000088	-0.000073	-0.000594	121.606662	23.947928	10.999406

doi:10.6342/NTU202202354

					Error_(m)	X_error	Y_error	Z_error			
#Total error					0.001342	0.001093	0.000669	0.000399			

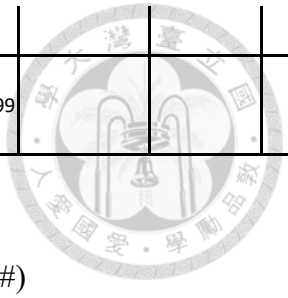

Post-event GCPs (labeled with point #) and ChPs (labeled with mes #)

#Label	X/Longitude	Y/Latitude	Z/Altitude	Accuracy_X/Y/Z (m)	Error_(m)	X_error	Y_error	Z_error	X_est	Y_est	Z_est
point 2	121.595026	23.941709	14	0.5	0.401808	0.345976	0.086388	0.185169	121.595029	23.941710	14.185169
point 3	121.584387	23.931955	26	0.5	0.719582	0.599427	-0.011107	-0.397948	121.584393	23.931955	25.602052
point 4	121.579035	23.926137	30	1	0.715555	-0.629344	0.019237	-0.339963	121.579029	23.926137	29.660037
point 6	121.605663	23.925477	31	0.5	1.047799	0.529041	-0.139447	-0.893618	121.605668	23.925476	30.106382
point 7	121.609408	23.935102	20	0.7	1.656641	0.527046	0.652332	-1.428686	121.609413	23.935108	18.571314
point 8	121.599164	23.911862	176	0.7	1.008228	0.259173	-0.873223	-0.432242	121.599167	23.911854	175.567758
point 10	121.582586	23.940258	27	0.5	0.689428	-0.328441	0.116133	0.594937	121.582583	23.940259	27.594937
point 12	121.582885	23.908677	16	1	1.50155	0.87211	-1.206827	0.194024	121.582894	23.908666	16.194024
point 14	121.584182	23.896956	79	0.5	1.27022	0.561176	-0.596163	-0.971148	121.584188	23.896951	78.028851
point 15	121.590205	23.894681	332	0.7	1.739461	1.353917	-0.653086	-0.875278	121.590218	23.894675	331.124722
point 16	121.597471	23.906074	225	0.5	1.655689	0.629649	-0.152461	-1.523682	121.597477	23.906073	223.476318
point 17	121.603875	23.899118	14	0.5	1.382257	0.678099	-0.739212	-0.95099	121.603882	23.899111	13.049010
point 18	121.591951	23.905152	73	0.7	1.224089	0.917529	0.275273	-0.762075	121.591960	23.905154	72.237925
point 19	121.603661	23.910657	31	0.5	1.093184	0.019792	-0.478079	-0.982904	121.603661	23.910653	30.017096
point 20	121.603433	23.912485	30	0.5	0.351275	0.287767	-0.106696	-0.17088	121.603436	23.912484	29.829120
point 21	121.590748	23.938772	18	0.5	0.522512	0.218089	-0.178531	0.439981	121.590750	23.938770	18.439981
point 22	121.586651	23.935804	24	0.5	0.677578	0.585246	0.058502	-0.336418	121.586657	23.935805	23.663582
point 24	121.594451	23.931095	14	0.5	0.18656	0.091458	0.052668	-0.153838	121.594452	23.931095	13.846162
point 26	121.606338	23.923556	30	0.5	1.236608	0.466586	0.201991	-1.127251	121.606343	23.923558	28.872749
point 27	121.602964	23.91855	151	1	3.044254	-0.087848	0.899996	-2.906849	121.602963	23.918558	148.093151
point 28	121.60383	23.903078	13	0.5	1.123403	0.554918	-0.43256	-0.87578	121.603835	23.903074	12.124220
point 29	121.603681	23.891278	15	0.5	0.457813	0.184937	-0.241213	-0.342355	121.603683	23.891276	14.657645
point 31	121.588616	23.923311	20	0.5	2.517932	-2.47382	0.379409	0.276122	121.588592	23.923314	20.276121
point 32	121.587436	23.943718	23	0.5	0.181077	-0.122831	-0.027574	0.130157	121.587435	23.943718	23.130157
point 33	121.594304	23.936412	14	0.5	0.407468	0.39315	0.070673	-0.080426	121.594308	23.936413	13.919574
point 34	121.579636	23.935795	32	0.5	0.246517	0.042731	-0.070839	-0.232221	121.579636	23.935794	31.767779
point 36	121.586646	23.939343	24	0.5	0.29077	0.251697	0.05309	-0.135563	121.586648	23.939343	23.864437
point 37	121.58267	23.935302	28	0.7	0.382959	0.368837	-0.045229	-0.092583	121.582674	23.935302	27.907417

doi:10.6342/NTU202202354

#Label	X/Longitude	Y/Latitude	Z/Altitude	Accuracy_X/Y/Z (m)	Error (m)	X_error	Y_error	Z_error	X_est	Y_est	Z_est
point 38	121.581382	23.932976	29	0.5	0.280054	-0.171951	-0.044236	0.216578	121.581380	23.932976	29.216578
point 39	121.590966	23.940297	18	0.5	0.467806	-0.045364	0.448671	0.124413	121.590966	23.940301	18.124413
mes 1	121.606593	23.945584	3	3	1.81406	1.679516	0.55071	-0.408359	121.606609	23.945589	2.591641
mes 2	121.602166	23.936972	6.5	1	1.858616	0.438915	0.05568	-1.805188	121.602170	23.936973	4.694812
mes 3	121.600217	23.92275	14	3	1.970909	1.118764	0.161251	-1.614574	121.600228	23.922751	12.385426
mes 4	121.591873	23.927092	15	3	0.529345	0.402744	-0.115981	-0.323344	121.591877	23.927091	14.676656
mes 5	121.596414	23.908428	203	3	4.55122	0.767543	-0.455814	4.462815	121.596422	23.908424	207.462815
mes 6	121.598329	23.911734	173	3	3.447471	0.872734	2.817167	1.785206	121.598338	23.911759	174.785205
mes 7	121.604033	23.92537	26	3	3.225609	2.554295	-0.210862	-1.958486	121.604058	23.925368	24.041514
mes 8	121.598431	23.919487	25	0.5	0.367665	0.34266	0.122107	0.053401	121.598434	23.919488	25.053401
#Total error					1.169777	0.677889	0.441577	0.844899			
#GCPs error					0.94934	0.22929	-0.0894	-0.46171			

Supplementary 4: The post-event SPOT 7 image with the linear feature on the sand bar

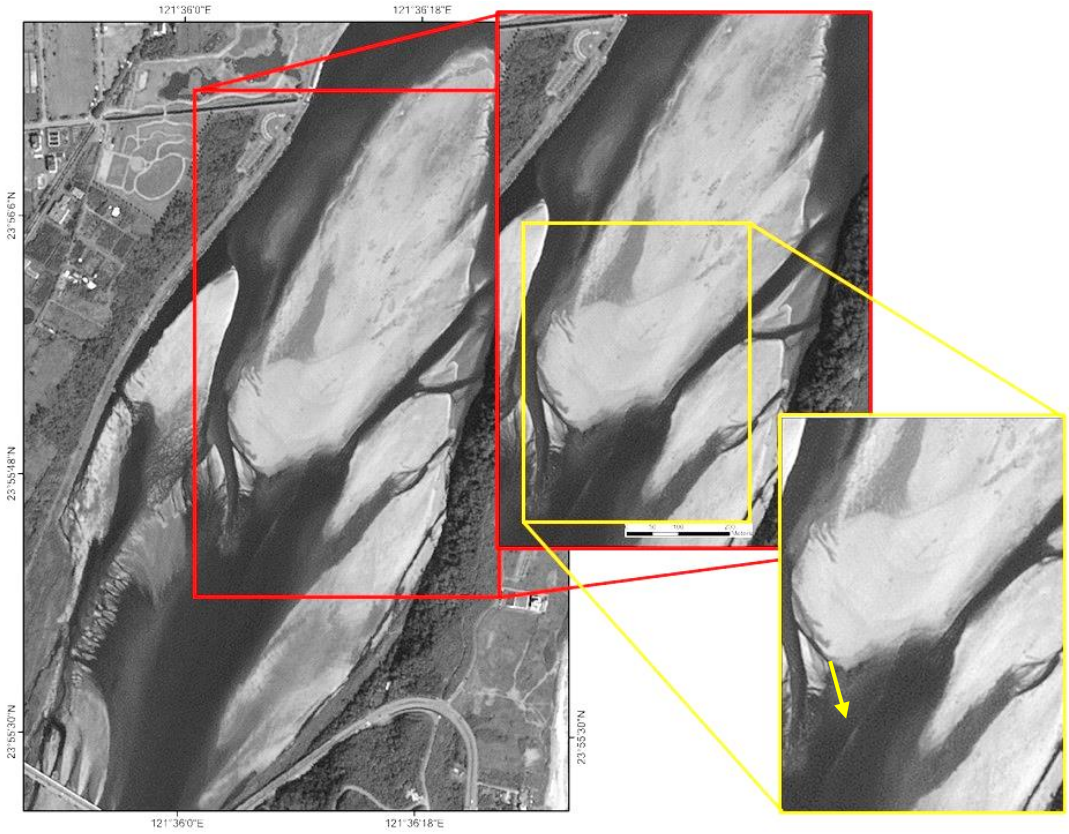

doi:10.6342/NTU202202354

Supplementary 5: The pre- and post-Google Earth images

(a)

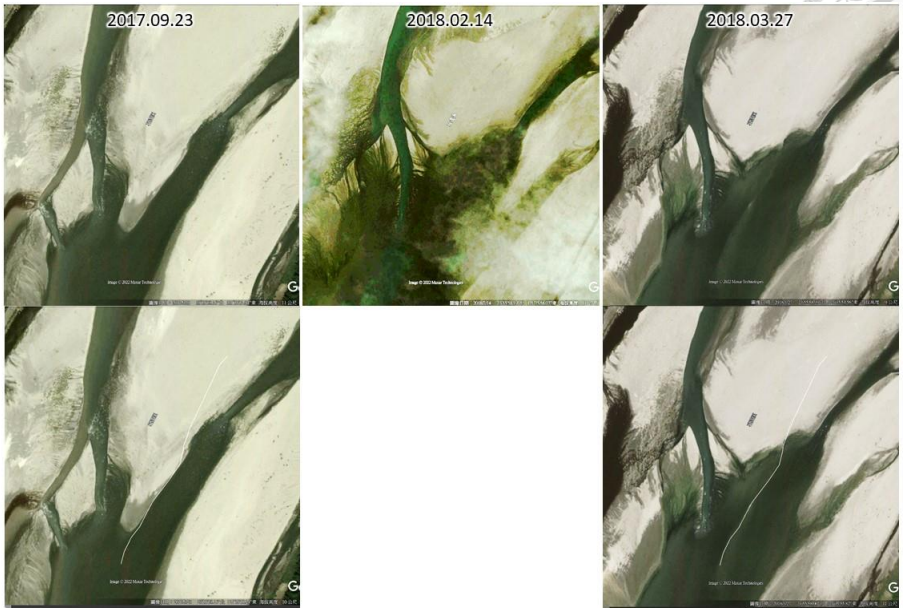

(b)

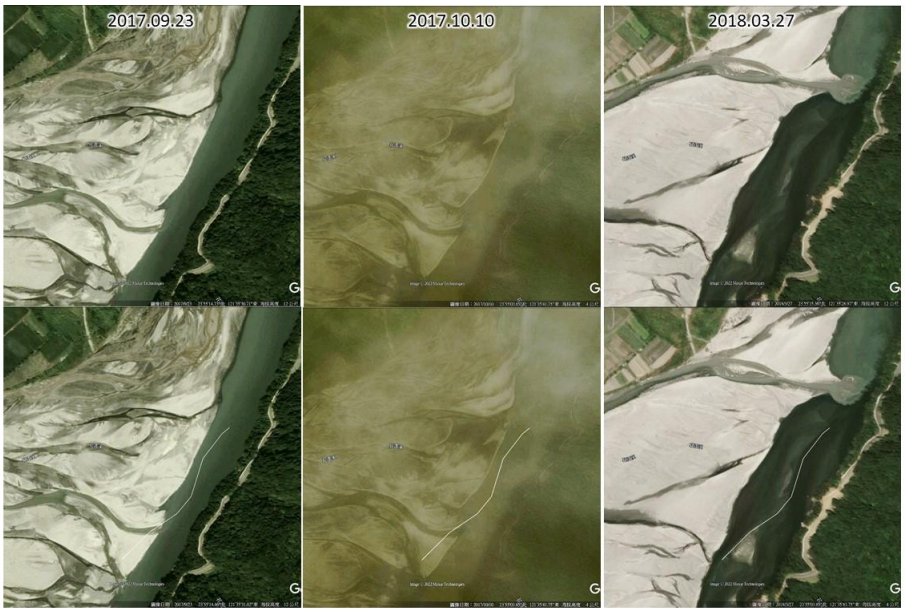

(c)

doi:10.6342/NTU202202354

Supplementary 6: The closer images of uncertain mapping result

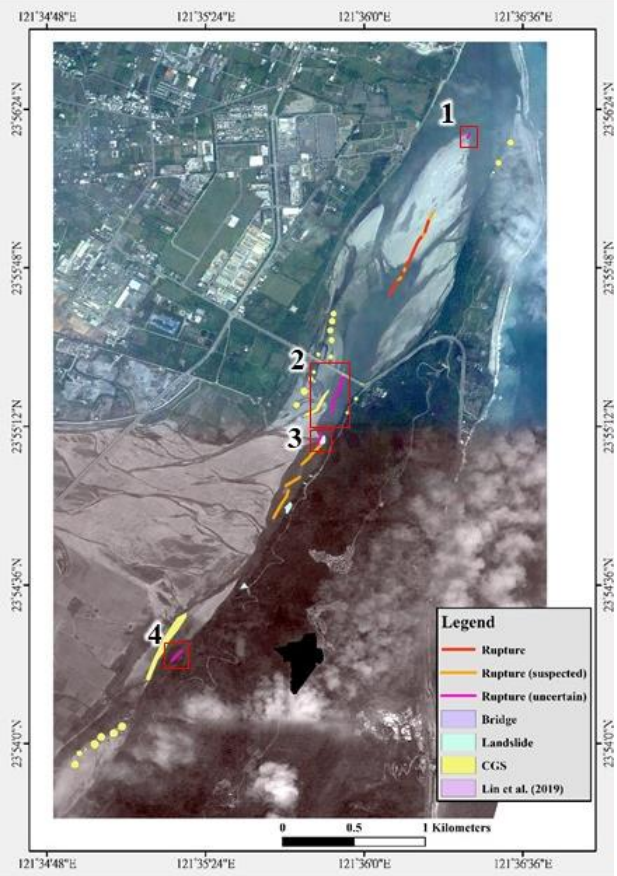

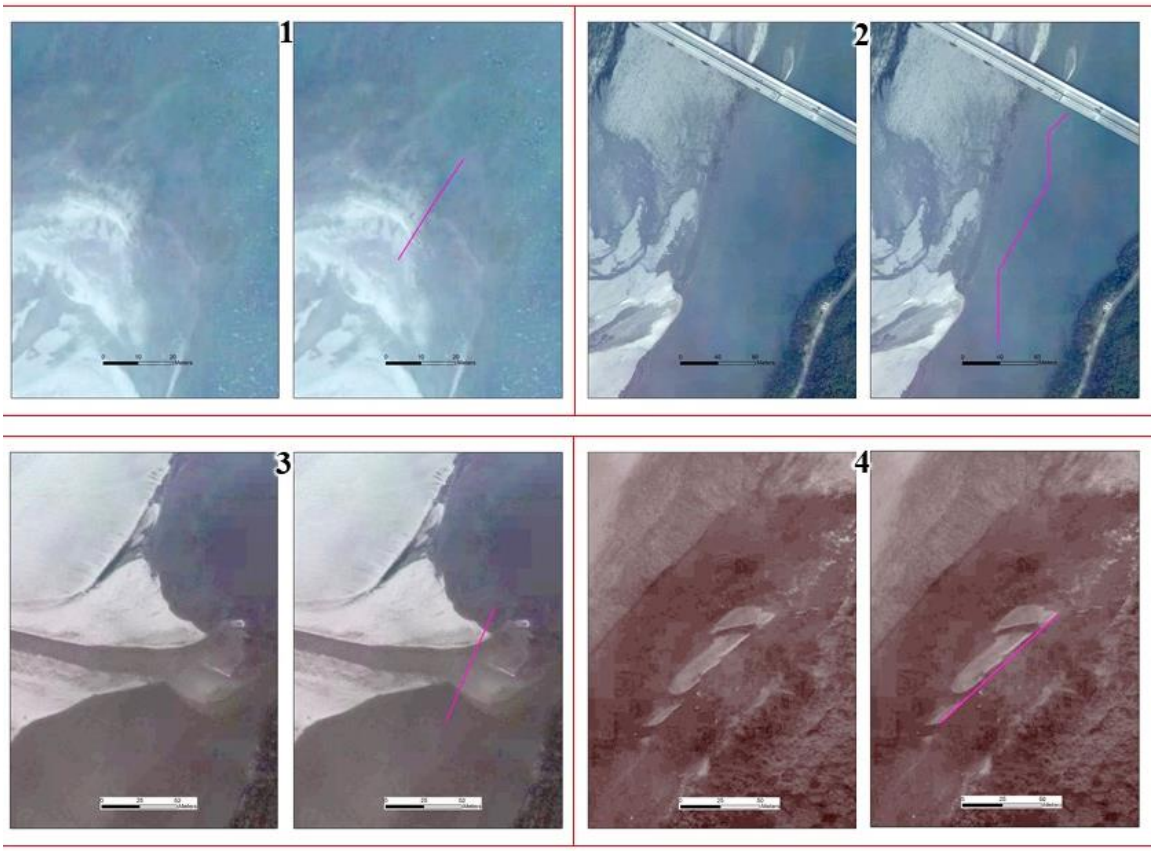

doi:10.6342/NTU202202354

Supplementary 7: N/S and E/W components of profiles

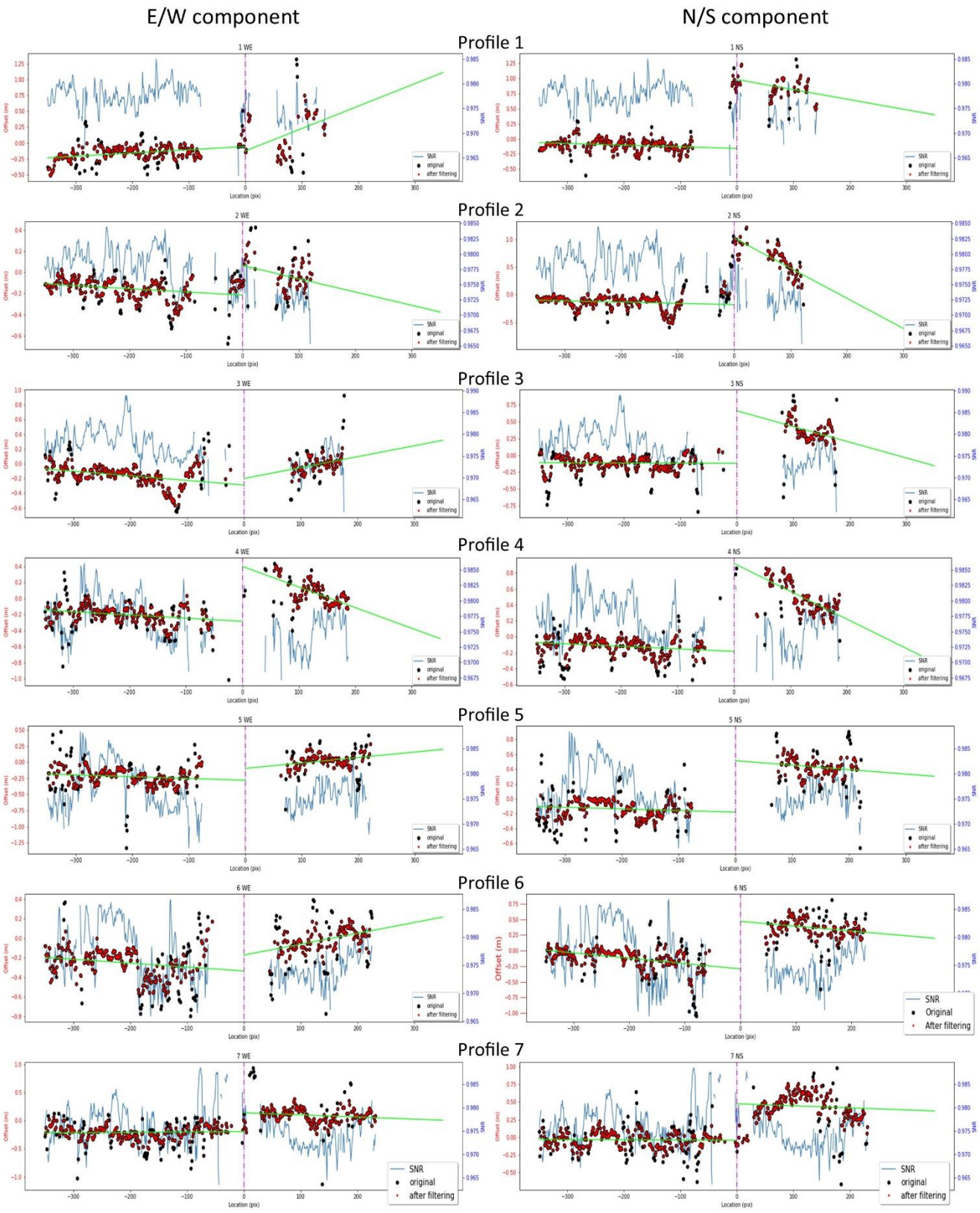

doi:10.6342/NTU202202354

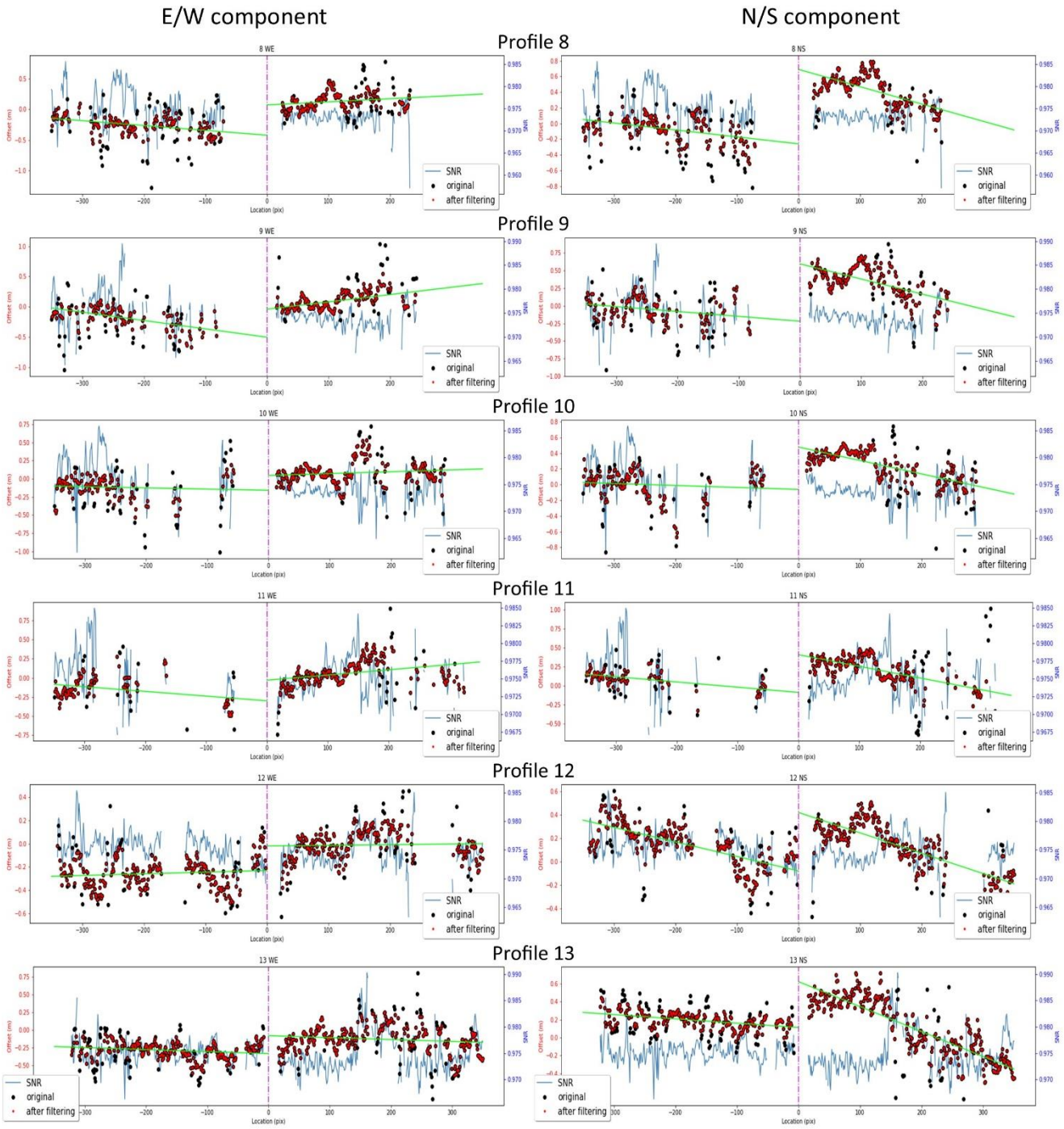

doi:10.6342/NTU202202354

The result of profiles across the Lingding Fault (window size 64X64)

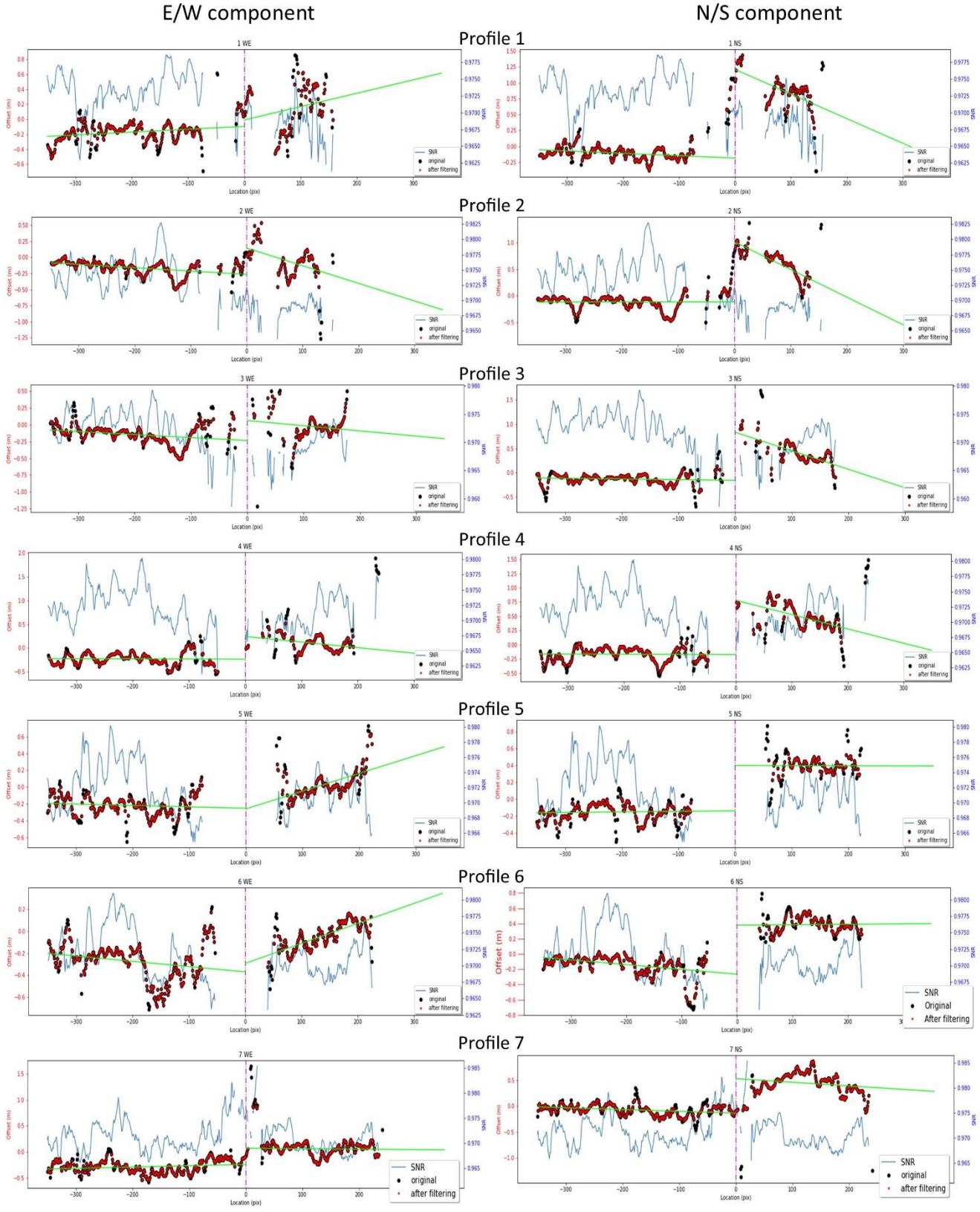

doi:10.6342/NTU202202354

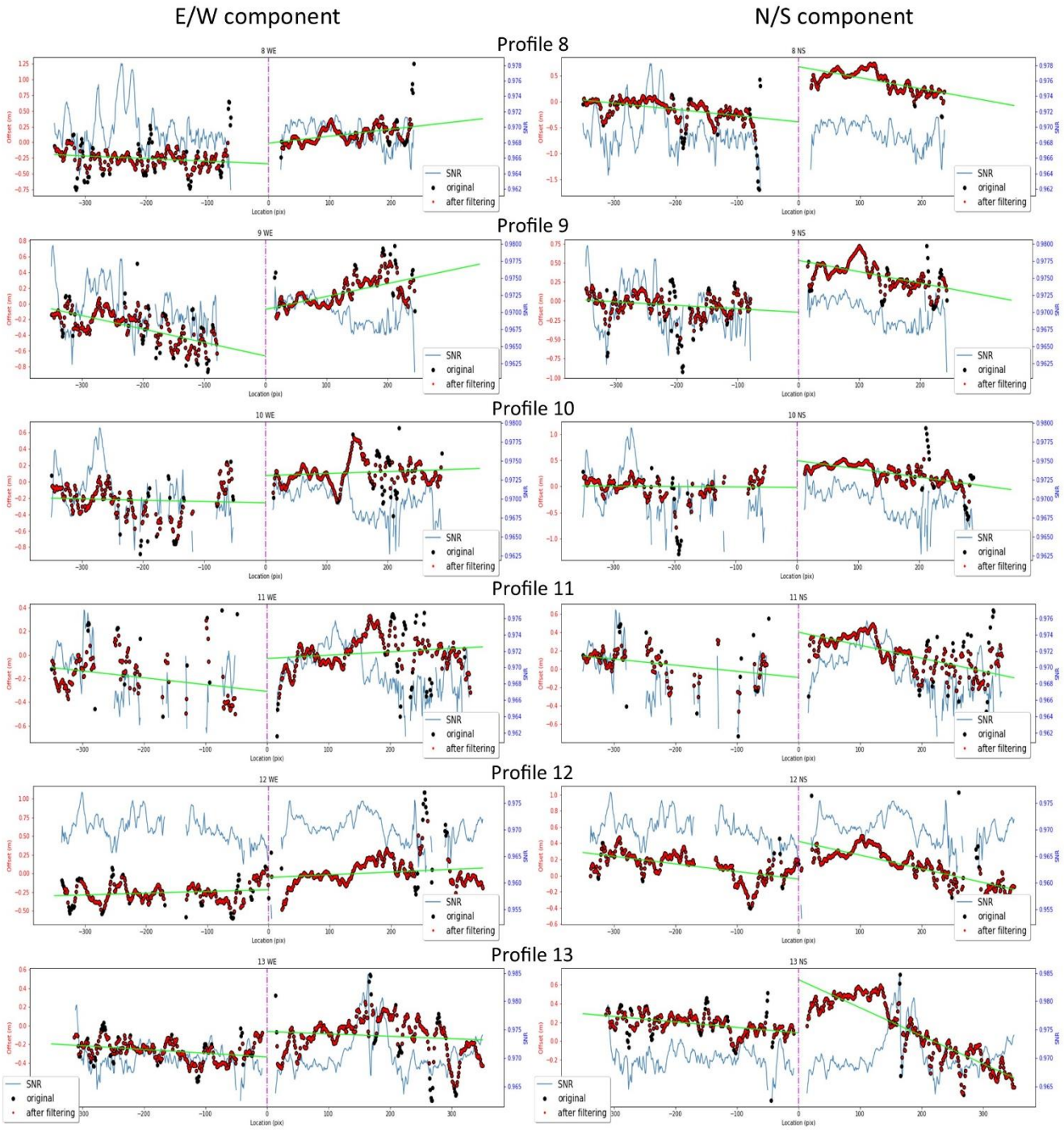

doi:10.6342/NTU202202354

The result of profiles across the Lingding Fault (window size 128X128)

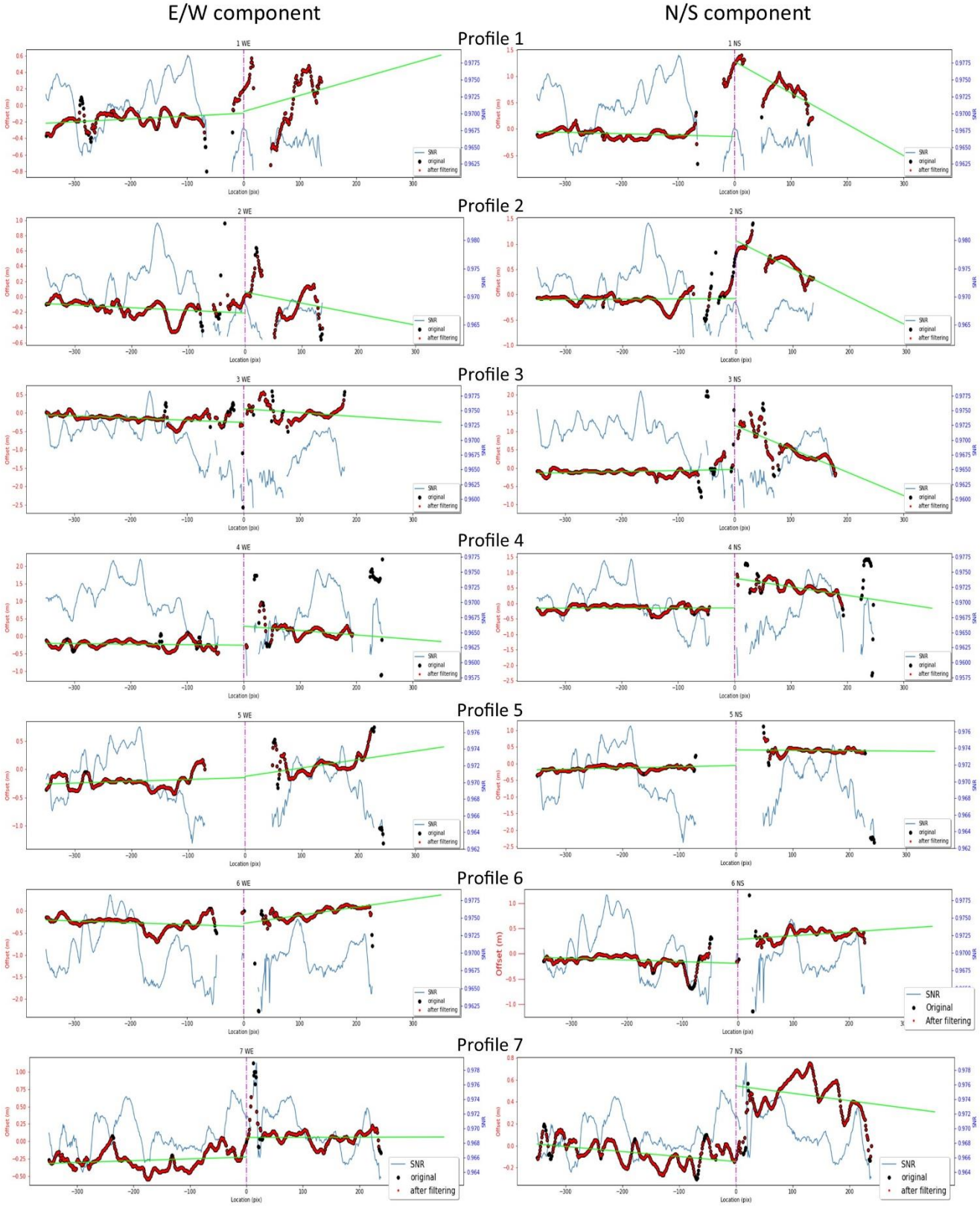

doi:10.6342/NTU202202354

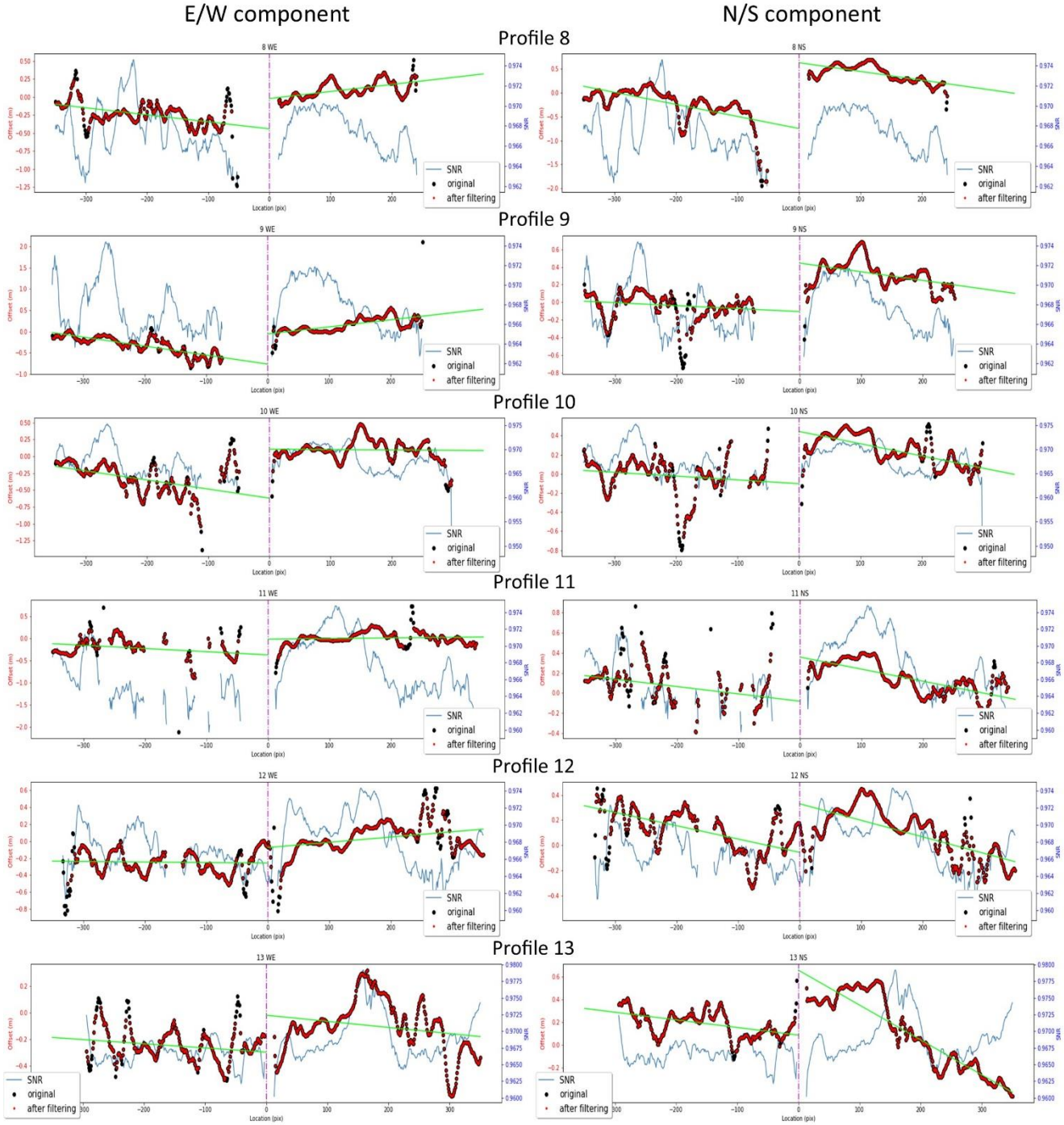

doi:10.6342/NTU202202354

Supplementary 8:
Perpendicular and parallel components of profiles

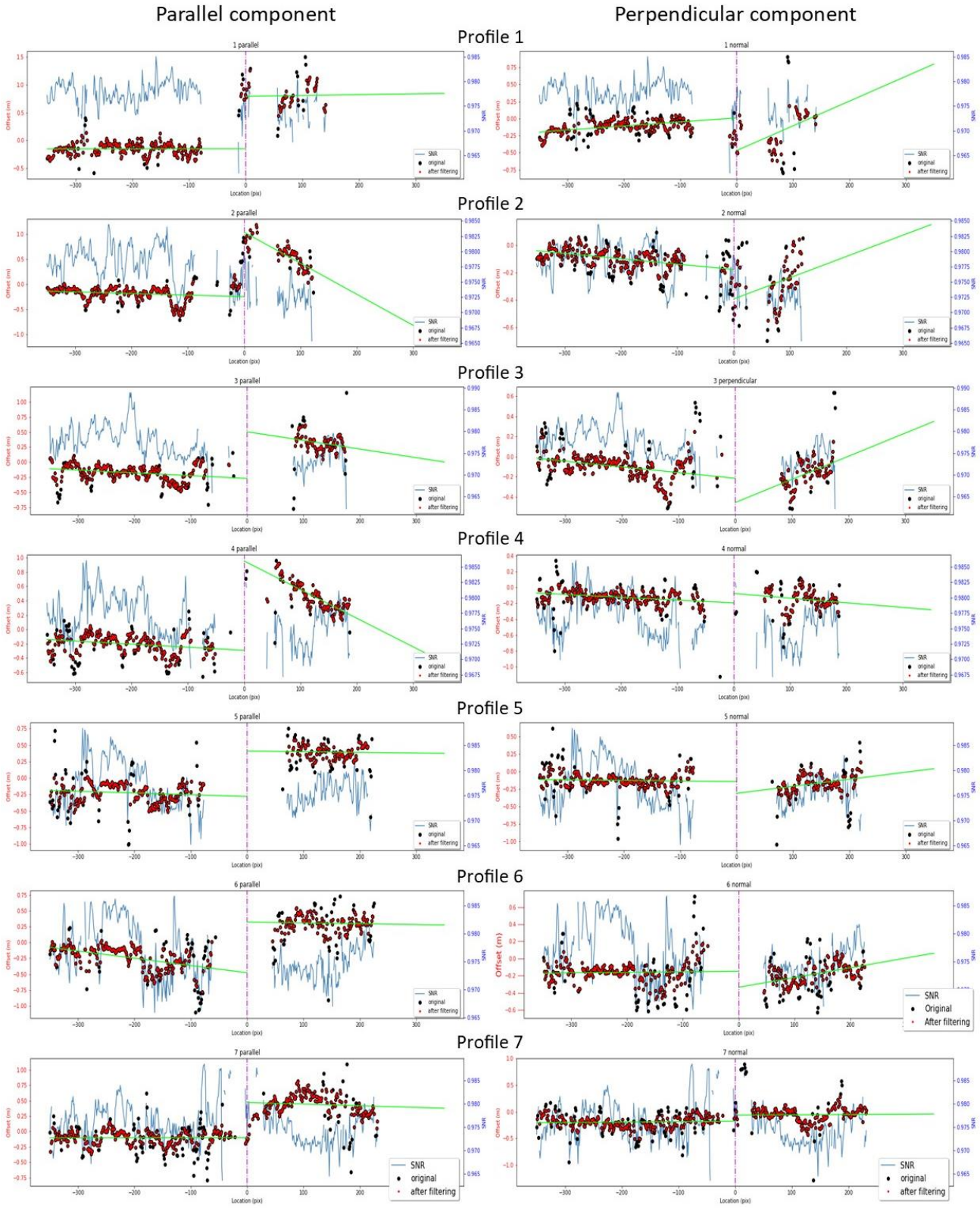

doi:10.6342/NTU202202354

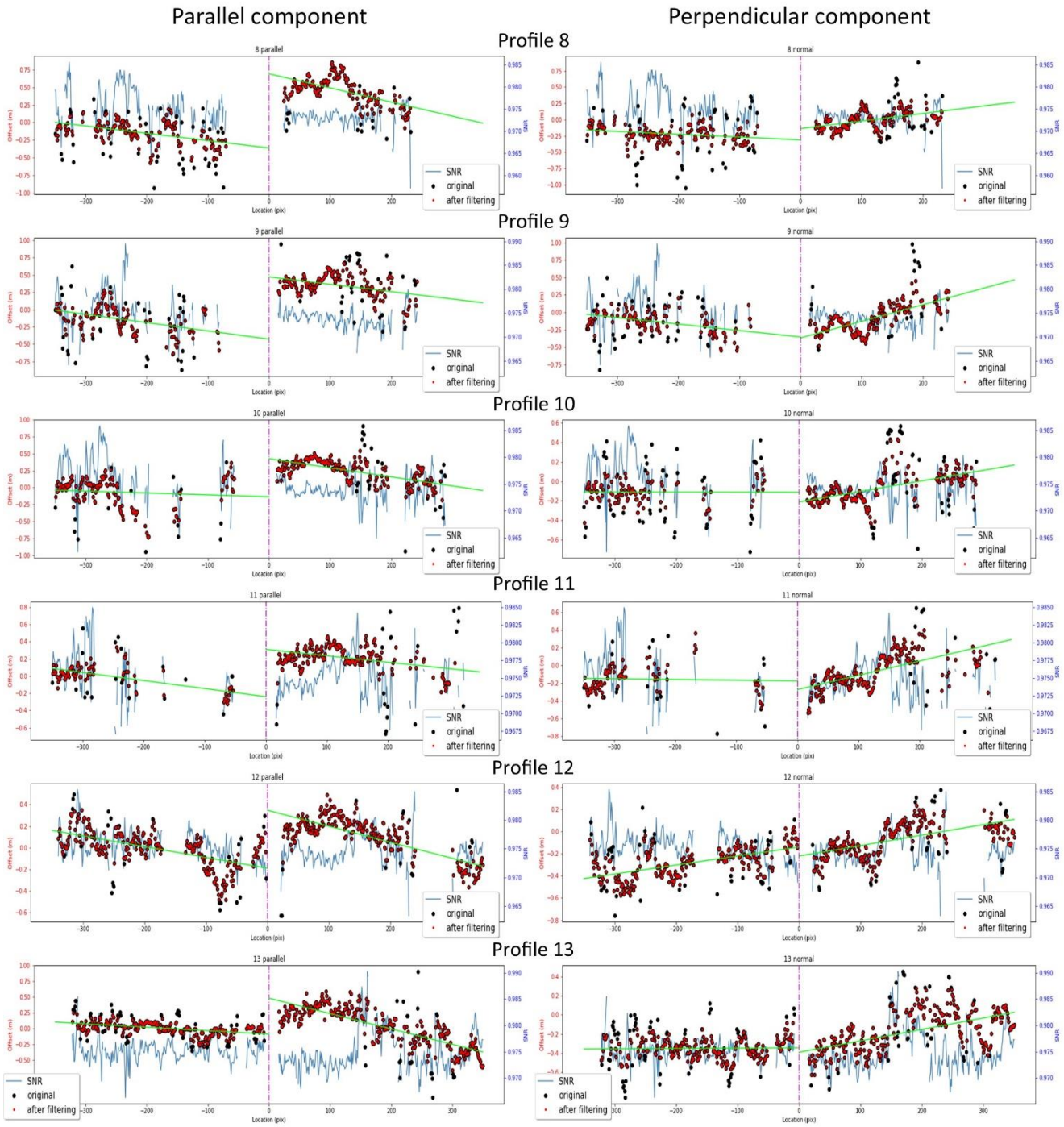

doi:10.6342/NTU202202354

The result of profiles across the Lingding Fault (window size 64X64)

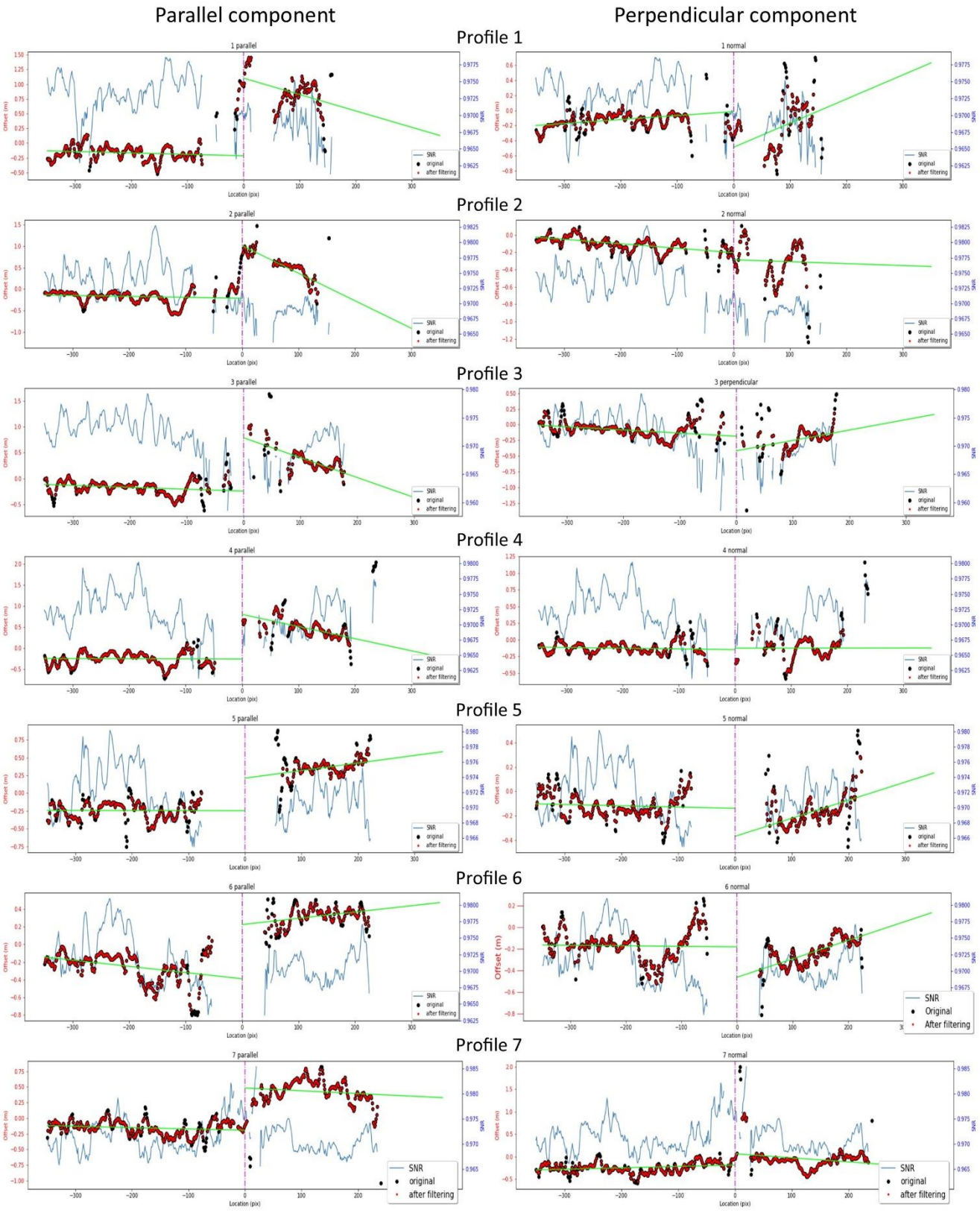

doi:10.6342/NTU202202354

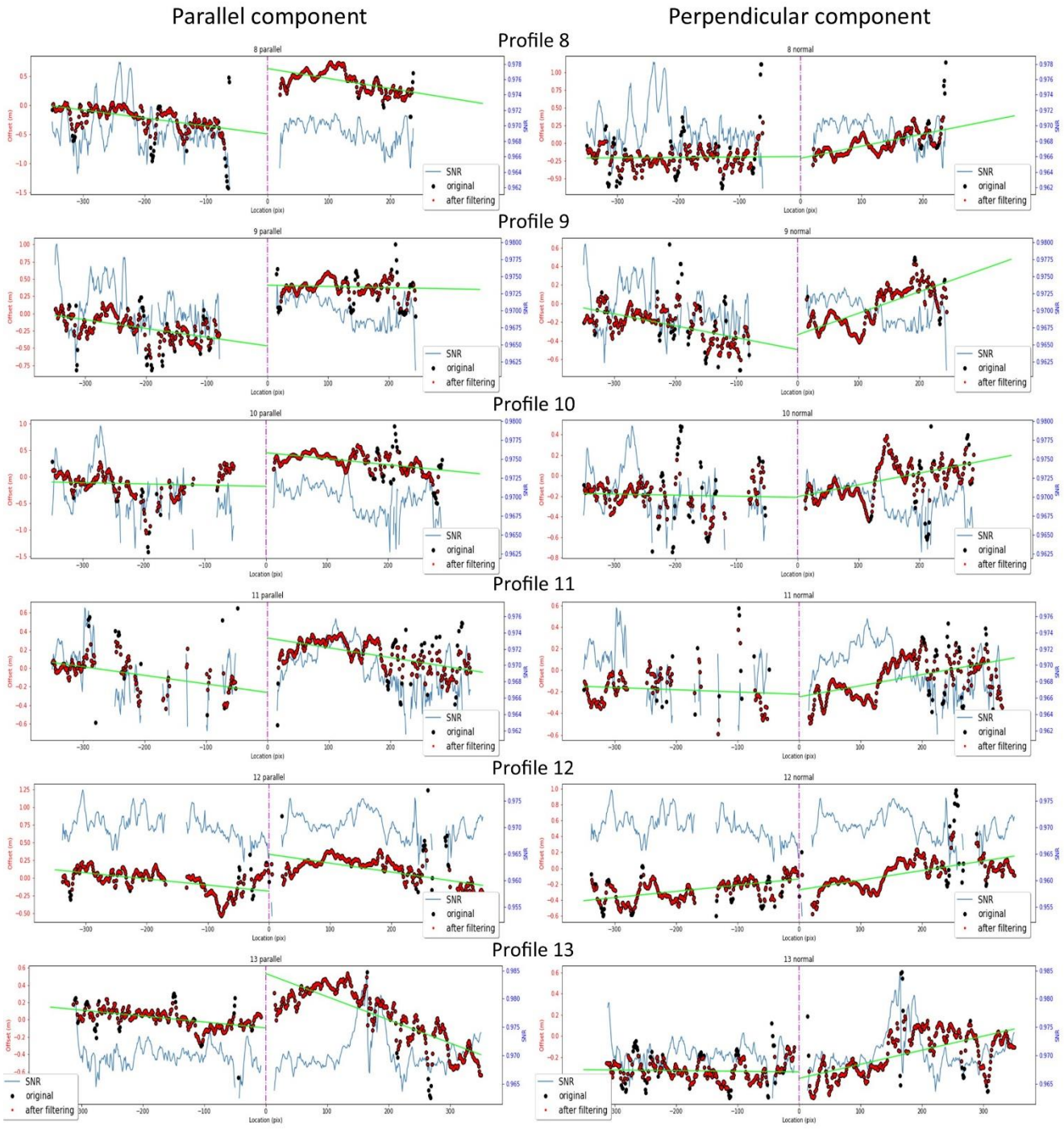

doi:10.6342/NTU202202354

The result of profiles across the Lingding Fault (window size 128X128)

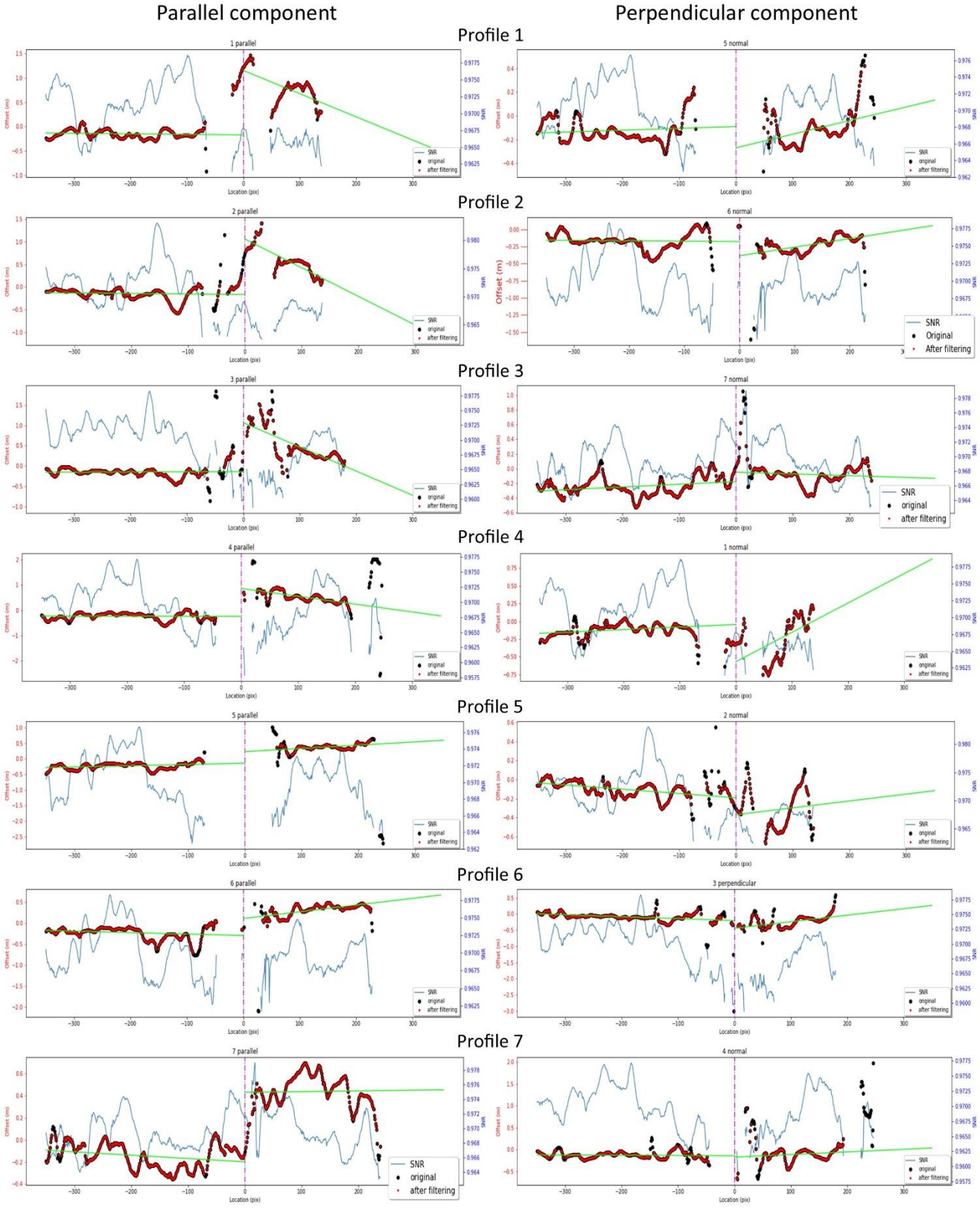

doi:10.6342/NTU202202354

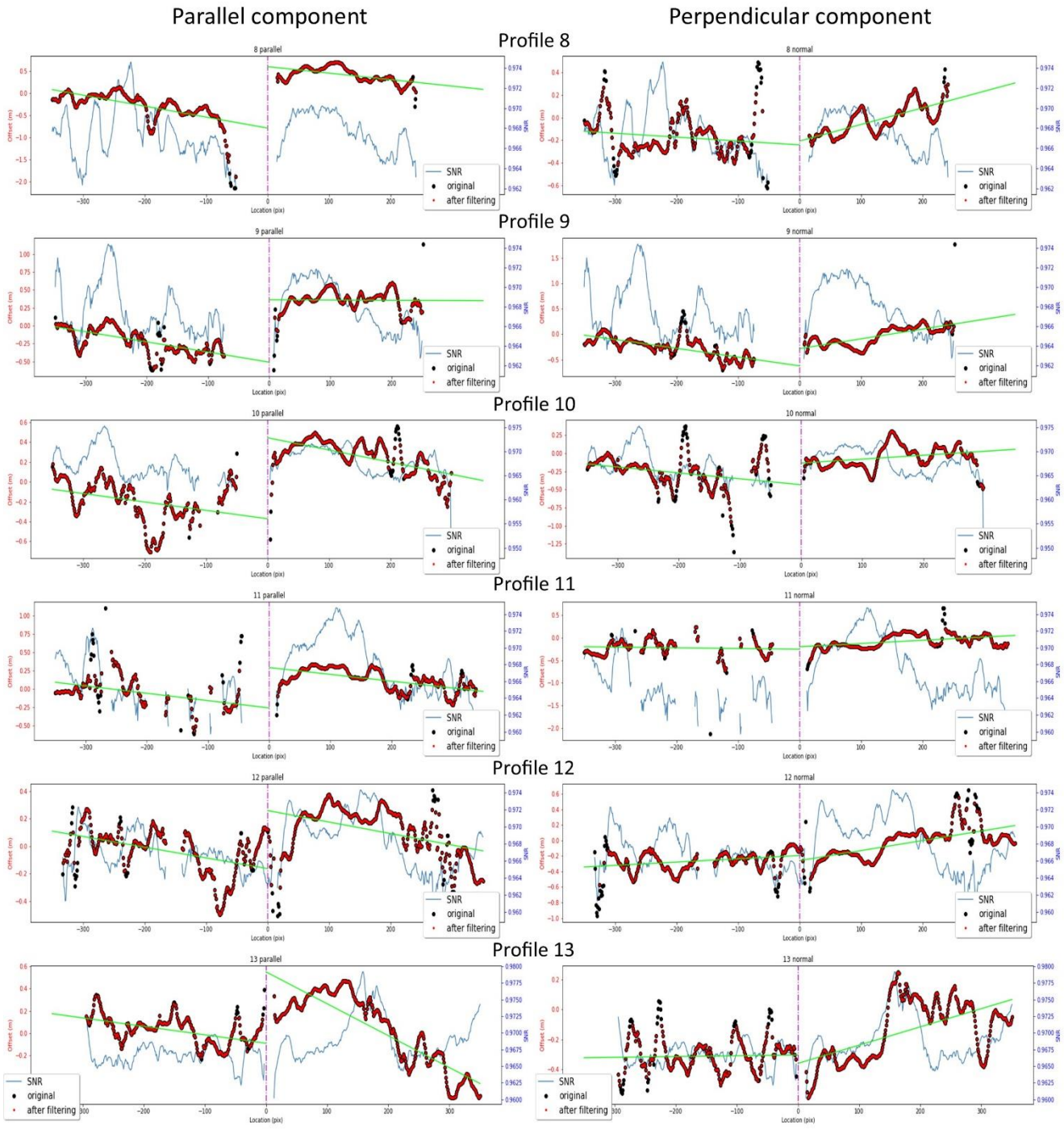

doi:10.6342/NTU202202354

Supplementary 9: The offset map for different methods of orthorectified aerial photos (a) GCPs only turned on in western part (b) GCPs only turned on in eastern part

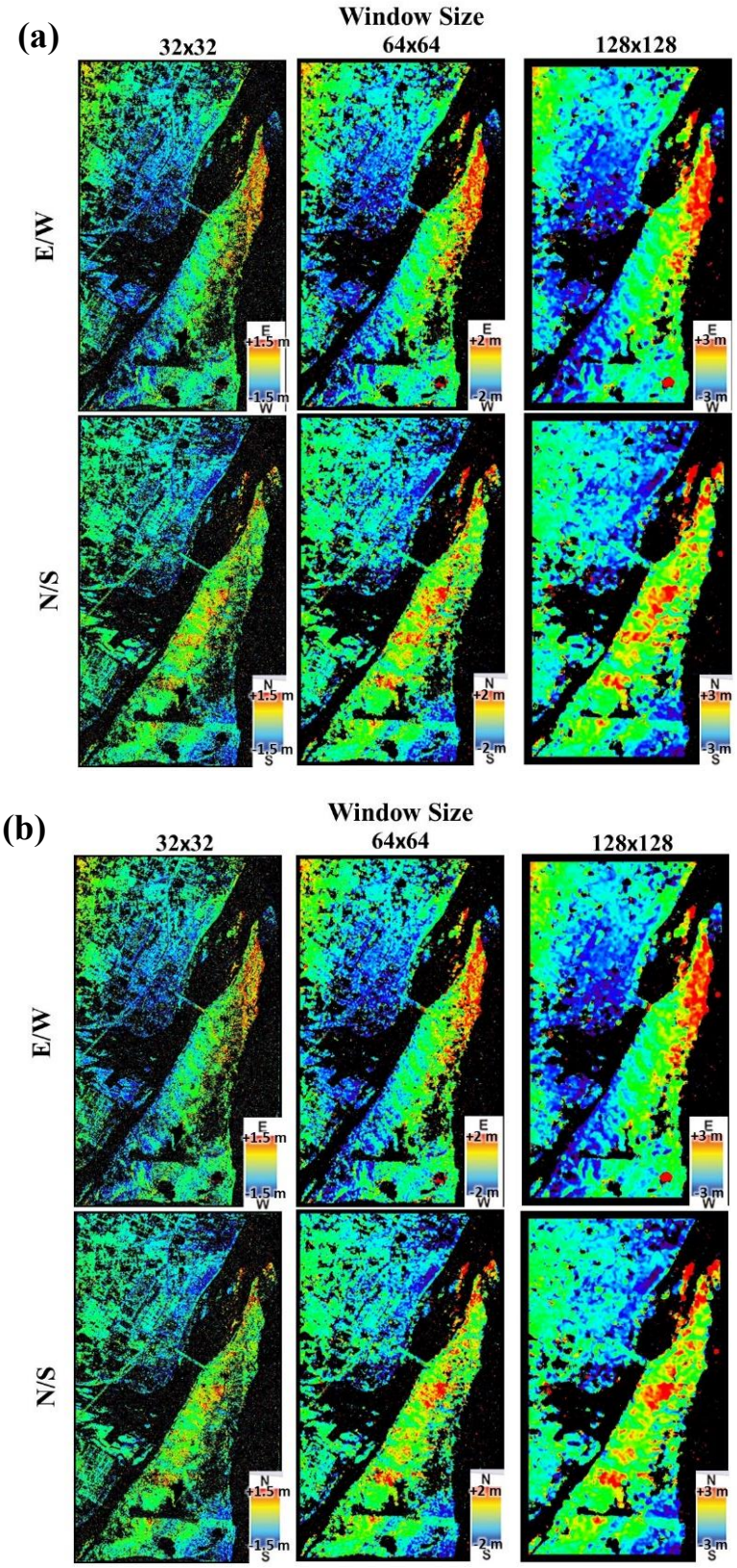

doi:10.6342/NTU202202354

Supplementary 10: Compared the results of different methods for orthorectified aerial photos with GNSS data (a) GCPs only turned on in western part (b) GCPs only turned on in eastern part

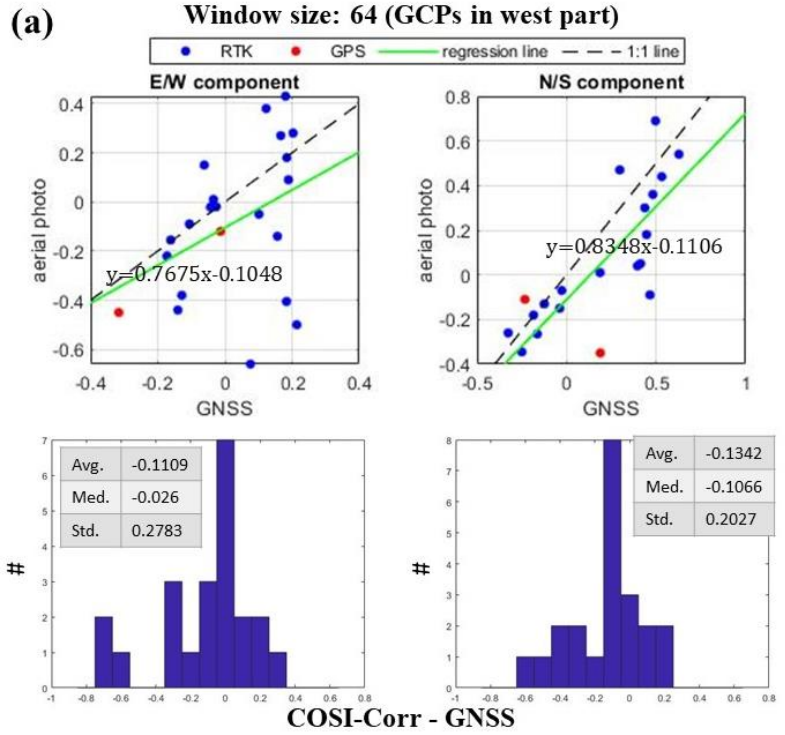

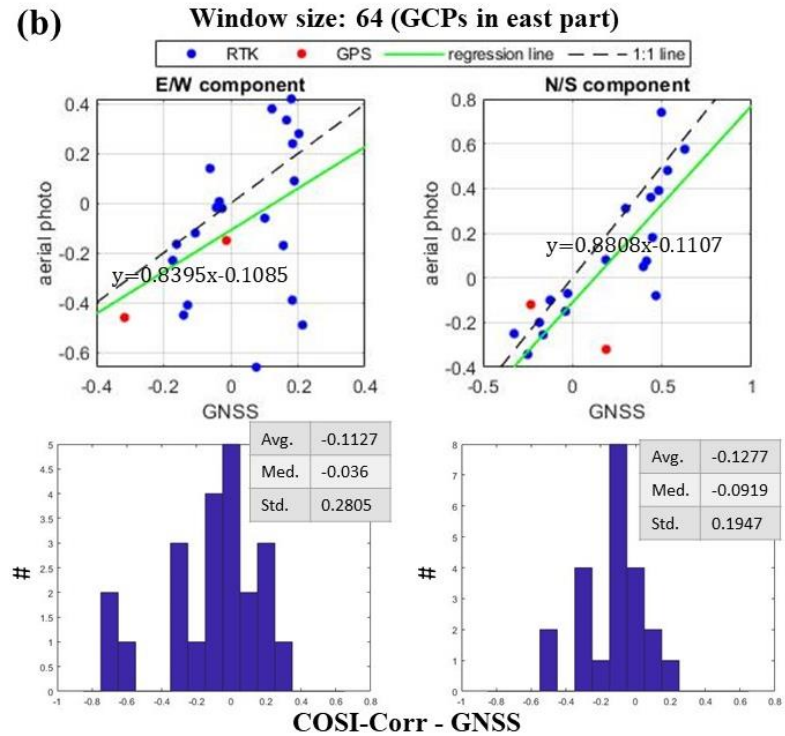

doi:10.6342/NTU202202354

Supplementary 11: (a) The comparison of GNSS and the result of COSI-Corr (window size 32x32), and the lower column is the distribution of the deviation between the result of COSI-Corr and GNSS. (b) The spatial distribution of the deviation between the result of COSI-Corr and GNSS, with E/W component and N/S component.

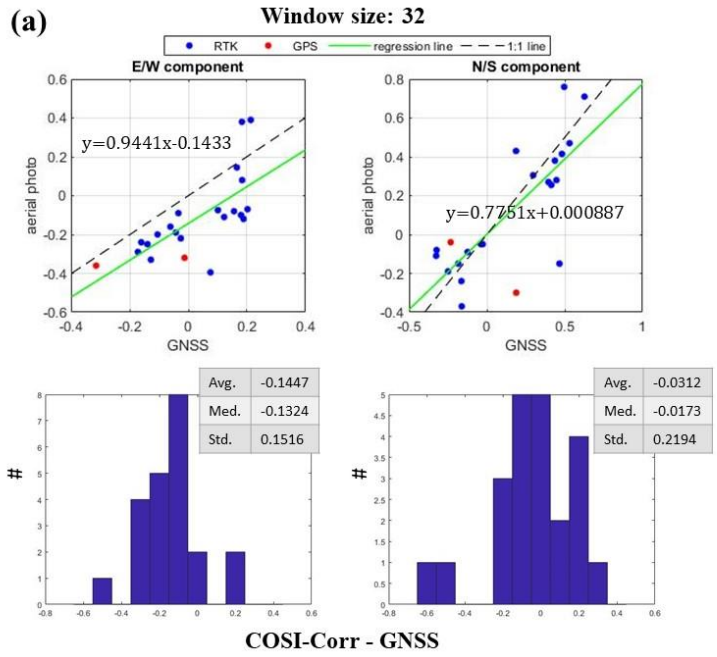

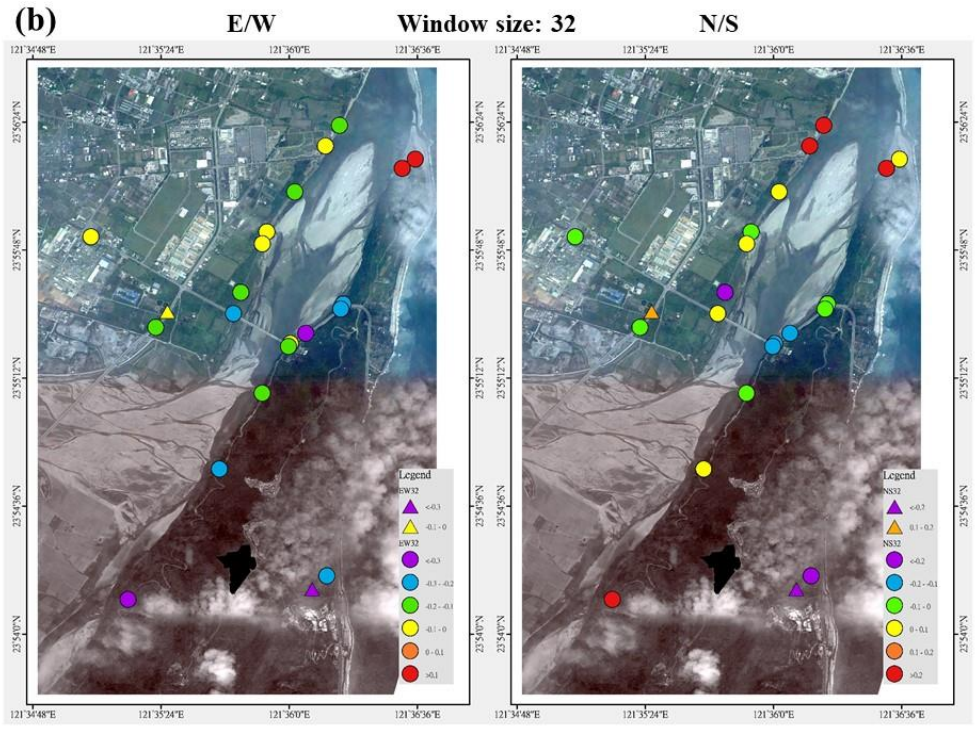

doi:10.6342/NTU202202354

Supplementary 12: (a) The comparison of GNSS and the result of COSI-Corr (window size 128x128), and the lower column is the distribution of the deviation between the result of COSI-Corr and GNSS. (b) The spatial distribution of the deviation between the result of COSI-Corr and GNSS, with E/W component and N/S component.

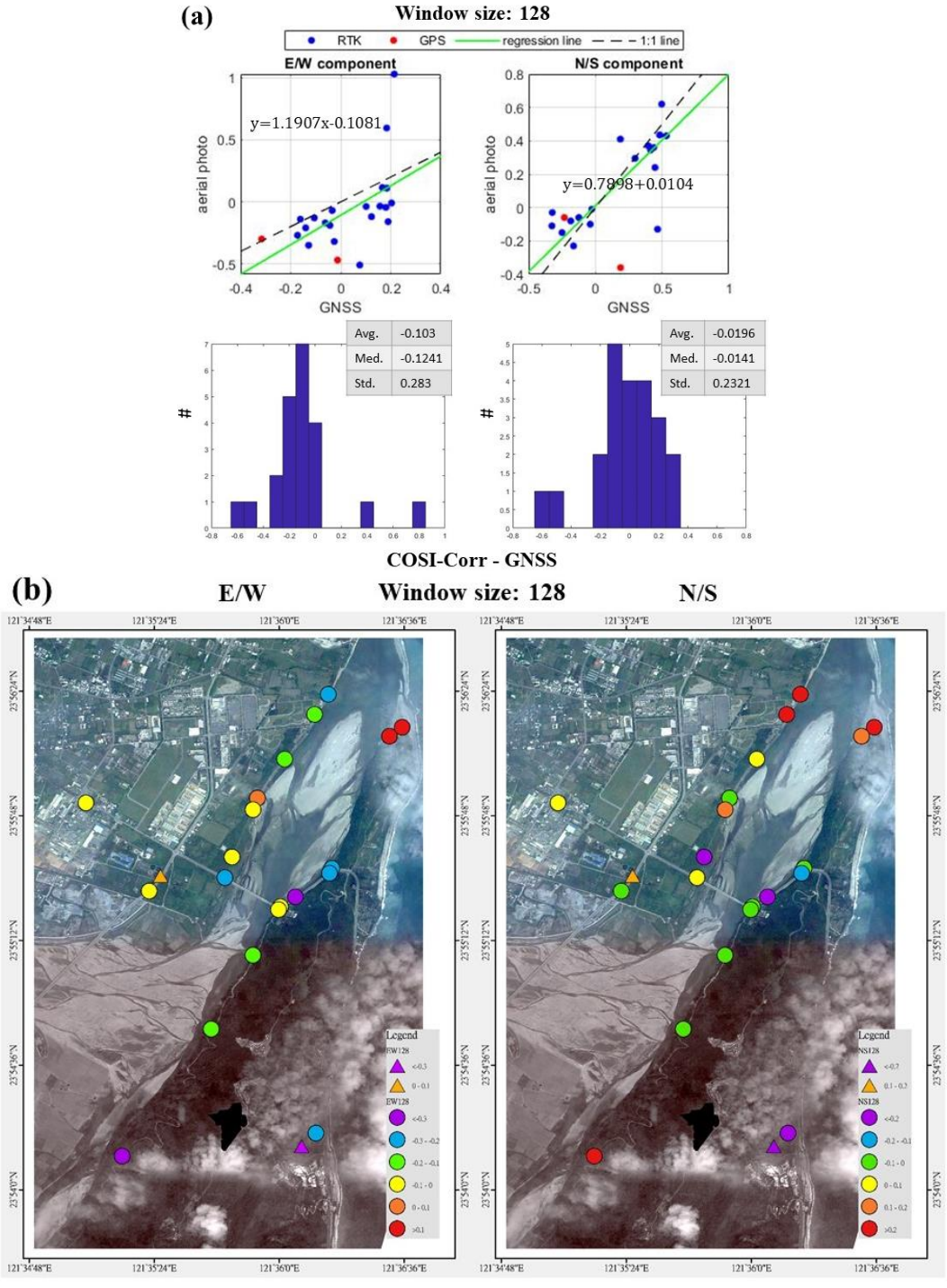

doi:10.6342/NTU202202354

Supplementary 13: The trade-off curve for the smoothing weighting factor (α) for different input data sets

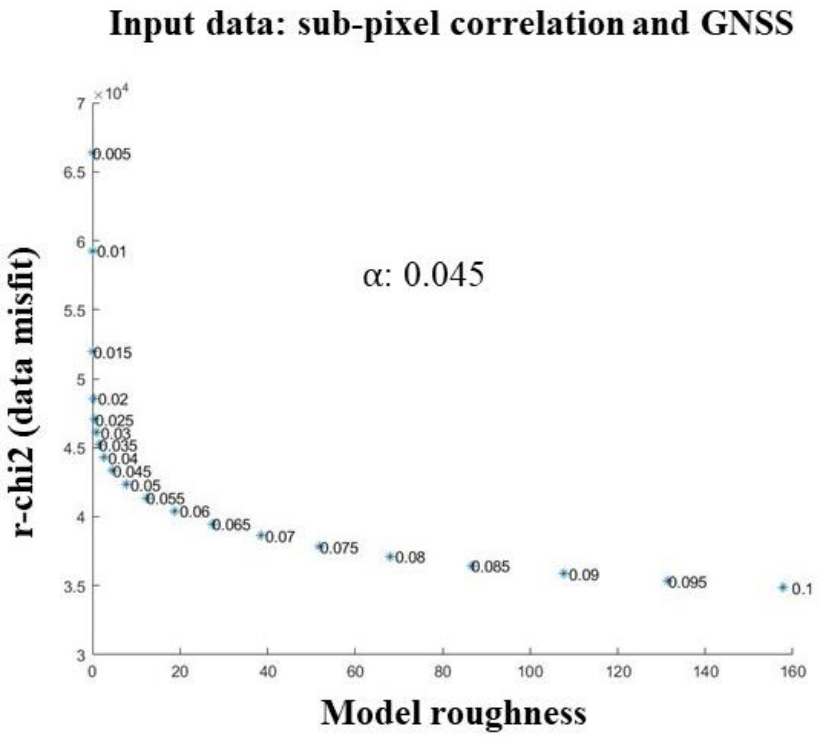

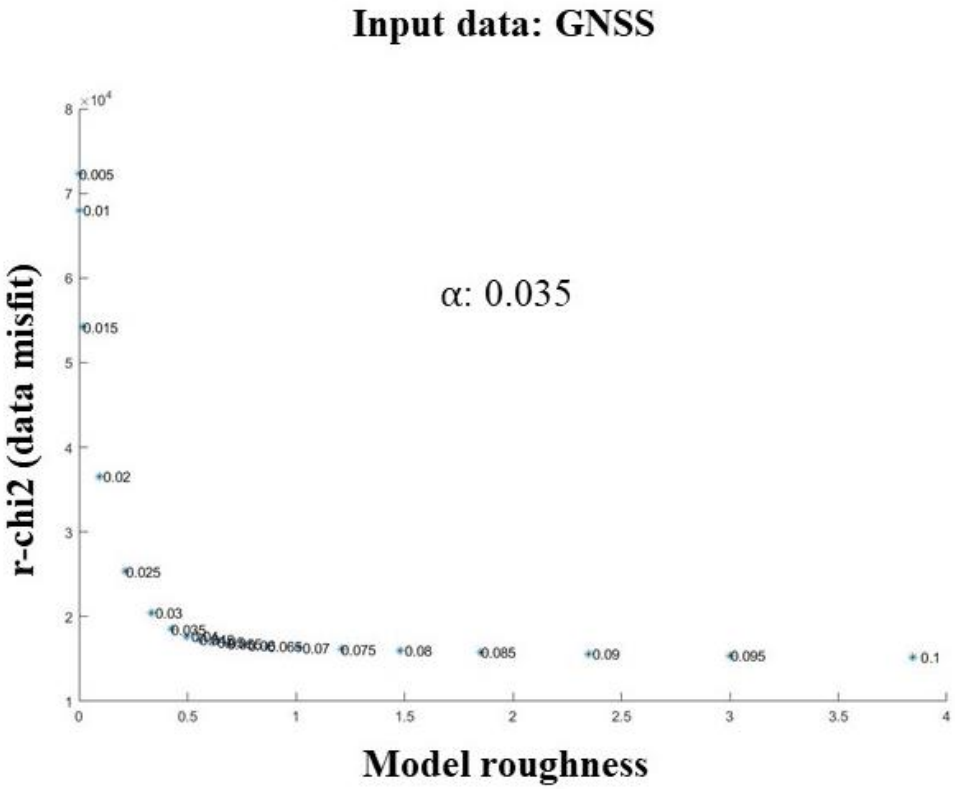

doi:10.6342/NTU202202354